ADVANCED ENERGY STORAGE SYSTEM FOR ELECTRIC VEHICLE CHARGING STATIONS FOR RURAL COMMUNITIES IN THE PACIFIC NORTHWEST

FINAL PROJECT REPORT

by

Dr. Herb Hess
University of Idaho

Sponsorship

Pacific Northwest Transportation Consortium (PacTrans)

for

Pacific Northwest Transportation Consortium (PacTrans)
USDOT University Transportation Center for Federal Region 10
University of Washington
More Hall 112, Box 352700
Seattle, WA 98195-2700

In cooperation with U.S. Department of Transportation,
Office of the Assistant Secretary for Research and Technology (OST-R)

DISCLAIMER

The contents of this report reflect the views of the authors, who are responsible for the facts and the accuracy of the information presented herein. This document is disseminated under the sponsorship of the U.S. Department of Transportation's University Transportation Centers Program, in the interest of information exchange. The Pacific Northwest Transportation Consortium, the U.S. Government and matching sponsor assume no liability for the contents or use thereof.

TECHNICAL REPORT DOCUMENTATION PAGE

1. Report No.	2. Government Accession No.	3. Recipient's Catalog No.
	01764465	

4. Title and Subtitle
Advanced energy storage system for electric vehicle charging stations for rural communities in the pacific northwest

5. Report Date
June 15, 2022

6. Performing Organization Code

7. Author(s) and Affiliations
Dr. Herb Hess
University of Idaho

8. Performing Organization Report No.
2022-S-UI-2

9. Performing Organization Name and Address
PacTrans
Pacific Northwest Transportation Consortium
University Transportation Center for Federal Region 10
University of Washington More Hall 112 Seattle, WA 98195-2700

10. Work Unit No. (TRAIS)

11. Contract or Grant No.
69A3551747110

12. Sponsoring Organization Name and Address
United States Department of Transportation
Research and Innovative Technology Administration
1200 New Jersey Avenue, SE
Washington, DC 20590

13. Type of Report and Period Covered
Final Project Report
January 25, 2022, through August 15, 2022

14. Sponsoring Agency Code

15. Supplementary Notes
Report uploaded to: www.pactrans.org

16. Abstract

A rural electric vehicle charging system is envisioned with an energy source, e.g., solar panels on a car port, energy storage, e.g., a flywheel energy storage system, and an energy sink, e.g., electric vehicle charging. The focus of this project was on the hardware development of the sensors and actuator subsystems of the energy storage system.

The energy storage device is a reluctance machine operated as either a motor or generator, depending on the direction of energy transfer. The rotor of the reluctance machine functions as a flywheel, storing energy in the rotating mass. The position of the rotating mass (rotor) is critical to the function and performance of the energy storage control system. Commutating electrical currents is necessary to energy transfer by the reluctance machine. Three types of sensors and actuators subsystems are used to control the reluctance machine: 1) position or displacement sensors, 2) electrical current sensors, and 3) electrical current actuators. The hardware interface of each sensor and actuator subsystem was developed, including functional testing of the sensors and actuator subsystems hardware with Simulink Real-Time hardware-in-the-loop. These subsystems can be integrated into the flywheel energy storage system.

17. Key Words
Sensors, Actuators, Dynamic Plant Model, Feedback Control, Field Regulated Reluctance Machine, Flywheel Energy Storage System, Advanced Rural Transportation Systems, Electric Vehicle Charging, Energy Conversion

18. Distribution Statement

19. Security Classification (of this report)	20. Security Classification (of this page)	21. No. of Pages	22. Price
Unclassified.	Unclassified.	45	N/A

SI* (MODERN METRIC) CONVERSION FACTORS

APPROXIMATE CONVERSIONS TO SI UNITS				
Symbol	**When You Know**	**Multiply By**	**To Find**	**Symbol**
		LENGTH		
in	inches	25.4	millimeters	mm
ft	feet	0.305	meters	m
yd	yards	0.914	meters	m
mi	miles	1.61	kilometers	km
		AREA		
in^2	square inches	645.2	square millimeters	mm^2
ft^2	square feet	0.093	square meters	m^2
yd^2	square yard	0.836	square meters	m^2
ac	acres	0.405	hectares	ha
mi^2	square miles	2.59	square kilometers	km^2
		VOLUME		
fl oz	fluid ounces	29.57	milliliters	mL
gal	gallons	3.785	liters	L
ft^3	cubic feet	0.028	cubic meters	m^3
yd^3	cubic yards	0.765	cubic meters	m^3
	NOTE: volumes greater than 1000 L shall be shown in m^3			
		MASS		
oz	ounces	28.35	grams	g
lb	pounds	0.454	kilograms	kg
T	short tons (2000 lb)	0.907	megagrams (or "metric ton")	Mg (or "t")
		TEMPERATURE (exact degrees)		
°F	Fahrenheit	5 (F-32)/9 or (F-32)/1.8	Celsius	°C
		ILLUMINATION		
fc	foot-candles	10.76	lux	lx
fl	foot-Lamberts	3.426	$candela/m^2$	cd/m^2
		FORCE and PRESSURE or STRESS		
lbf	poundforce	4.45	newtons	N
lbf/in^2	poundforce per square inch	6.89	kilopascals	kPa

APPROXIMATE CONVERSIONS FROM SI UNITS				
Symbol	**When You Know**	**Multiply By**	**To Find**	**Symbol**
		LENGTH		
mm	millimeters	0.039	inches	in
m	meters	3.28	feet	ft
m	meters	1.09	yards	yd
km	kilometers	0.621	miles	mi
		AREA		
mm^2	square millimeters	0.0016	square inches	in^2
m^2	square meters	10.764	square feet	ft^2
m^2	square meters	1.195	square yards	yd^2
ha	hectares	2.47	acres	ac
km^2	square kilometers	0.386	square miles	mi^2
		VOLUME		
mL	milliliters	0.034	fluid ounces	fl oz
L	liters	0.264	gallons	gal
m^3	cubic meters	35.314	cubic feet	ft^3
m^3	cubic meters	1.307	cubic yards	yd^3
		MASS		
g	grams	0.035	ounces	oz
kg	kilograms	2.202	pounds	lb
Mg (or "t")	megagrams (or "metric ton")	1.103	short tons (2000 lb)	T
		TEMPERATURE (exact degrees)		
°C	Celsius	1.8C+32	Fahrenheit	°F
		ILLUMINATION		
lx	lux	0.0929	foot-candles	fc
cd/m^2	$candela/m^2$	0.2919	foot-Lamberts	fl
		FORCE and PRESSURE or STRESS		
N	newtons	0.225	poundforce	lbf
kPa	kilopascals	0.145	poundforce per square inch	lbf/in^2

*SI is the symbol for the International System of Units. Appropriate rounding should be made to comply with Section 4 of ASTM E380.
(Revised March 2003)

TABLE OF CONTENTS

LIST OF FIGURES

LIST OF TABLES

LIST OF ABBREVIATIONS

ac:	Alternating current
AMB:	Active magnetic bearing
CS:	Current sensor
dc:	Direct current
DIN:	Deutsche Institut fur Normung (German Institute of Standards)
DIR:	Direction
ESS:	Energy storage system
EV:	Electric vehicle
FESS:	Flywheel energy storage system
FET:	Field-effect transistor
FRRM:	Field regulated reluctance machine
GHA:	
GLB:	
HIL:	Hardware-in-the-loop
IC:	Integrated circuit
IMEAS:	Measured current
LLC:	Inductor-inductor-capacitor
MATLAB:	MATrix LABoratory, a mathematical simulation software by The Mathworks
MOSFET:	Metal oxide semiconductor field effect transistor
PacTrans:	Pacific Northwest Transportation Consortium
PCB:	Printed circuit board
PI:	Proportional-integral
PNW:	Pacific Northwest
PV:	Photovoltaic
PWM:	Pulse width modulation
PWMH:	Pulse width modulation
PWML:	Pulse width modulation
RC:	Resister-capacitor
RES:	Renewable energy source
Simulink:	MATLAB-based graphical programming environment

TSSOP:	Thin shrink small outline package
TTL:	Transistor transistor logic
UI:	University of Idaho
Vac:	Volts alternating current
VBB:	Voltage base base
VCC	Common collector voltage, power supply voltage
Vdc:	Volts direct current
VFD:	Variable frequency drive
VIOUT:	Analog voltage proportional to a measured current
XMEAS:	Measured displacement

EXECUTIVE SUMMARY

This project developed the mathematical models, MATLAB Simulink simulations, and hardware functional testing of the sensor and actuator subsystems for a flywheel energy storage system (FESS). The mathematical models described ideal sensor and actuator behavior. The simulation facilitated critical evaluation of candidate signal processing (e.g., sampling, filtering, response time, etc.) in the context of the energy storage system. The MATLAB Simulink simulation(s) were extended to Simulink Real-Time hardware-in-the-loop testing with physical sensors and actuators, enabling verification of the modeling assumptions and limitations.

The electrical current actuator was mathematically modeled using H-bridge pulse width modulation current control [23]. While the theory has been well established, the limitations and non-idealities of the physical current actuator subsystem needed to be well understood before integration into the FESS.

The electrical current sensor was well defined in the mathematical model and was based on the manufacturers' data for the actual hardware. The current sensors' ratiometric output sensitivity to the current sensors' 5V supply voltage warrants careful selection of a 5V power source. This is an example of a small but important hardware implementation detail that was observed only during physical hardware testing.

The position or displacement sensor was also well defined in the mathematical model and was based on the manufacturers' data for the actual hardware. The physical hardware testing was notably consistent with the mathematical model and MATLAB Simulink simulations.

For all three sensors and actuators subsystems, the physical interface is described and documented for integration into the flywheel energy storage system.

The rotary absolute encoder was used in the University of Idaho (UI) FESS. Chapter 9 presents the results of this project's development of the rotary encoder system interface. The rotary encoder interface did not work initially. The troubleshooting steps taken to get to root out the cause are detailed. After the root cause had been identified and sufficiently addressed, the Renishaw Resolute™ rotary absolute encoder system block diagram was functional on the bench.

Having the UI FESS rotor assembly supported magnetically by a Halbach magnet array (as shown in Figure 1.3) was a major component of this project's end goal. An intermediate

development step specifically pertaining to the rotor assembly's support along its axis of rotation, the z-axis, was taken and is detailed in Chapter 10.

CHAPTER 1. INTRODUCTION

1.1. Typical Application Block Diagram / Overview

The University of Idaho (UI) is developing a flywheel energy storage system (FESS) for applications including electric vehicle (EV) charging stations. A solar carport array of photovoltaic modules could convert solar energy into electricity, as shown in Figure 1.1.

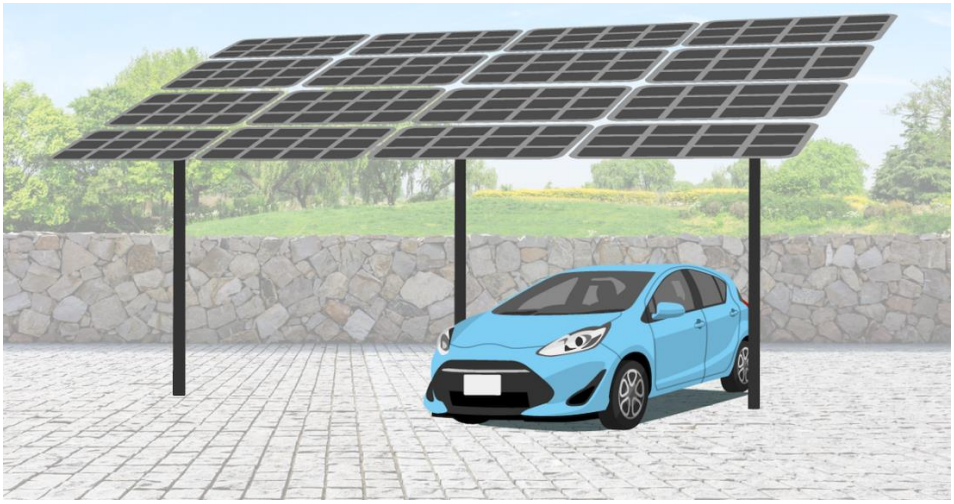

Figure 1.1 Solar Carport

In such as system, all electricity will be consumed as it is generated. If an EV is not present when the sun shines on a solar carport, then energy storage will be needed. The purpose of the UI FESS will be to store energy when the photovoltaic (PV) module array supplies more power than the load consumes, and to supply stored energy when the PV array supplies less power than the load demands. Thus, the UI FESS will be in the business of balancing supply and demand. Ideal UI FESS operation will maintain a constant direct current (dc) bus voltage (see Figure 1.2).

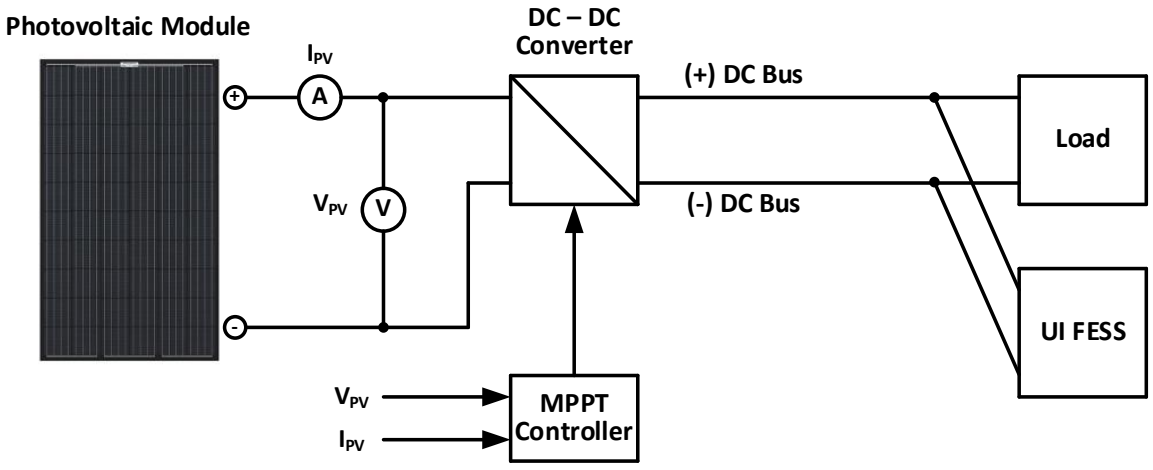

Figure 1.2 Flywheel Energy Storage System Typical Application Block Diagram

1.2. UI FESS Functional Block Diagram / Overview

The UI FESS is an energy storage flywheel. Energy storage flywheels have very high performance and work on simple principles. To understand their operation, it is best to start with the electric motor-generator. An electric motor-generator is the same machine running in opposite directions. When one puts electrical energy into a motor-generator, it turns into mechanical energy on the spinning rotor; that is a motor. When one puts mechanical energy into the motor-generator by spinning the rotor, electrical energy can be drawn back out; that is a generator. For an energy storage flywheel, the motor-generator is hooked up to a wheel. For the UI FESS, the rotor is the flywheel. When electrical energy is put into the motor-generator it accelerates the rotor storing that energy as momentum on the rotor. To retrieve the electrical energy, the momentum of the spinning rotor is allowed to drive the motor-generator, regenerating electricity and slowing the rotor. Because our motor-generator is run in a vacuum and on magnetic bearings, very little energy is lost over time.

Figure 1.3 shows the UI FESS functional block diagram. It shows the measurement, control, and motor-generator energy exchange functions of a six-axis flywheel rotating about a vertical axis. A rotary encoder measures the rotating position of the flywheel's rotor in its yaw axis. Four displacement sensors measure displacement of the rotor in the two horizontal dimensions. From their measurements, pitch and roll are also calculated. The Halbach Magnet Array provides passive displacement in the vertical axis. These measurements are provided to a

real-time digital controller based in a Speedgoat module. The Speedgoat module calculates commands for two sets of Pololu Motor Drivers to stabilize the flywheel in all six dimensions and to regulate the flow of energy by controlling angular velocity and angular position of the flywheel in its yaw axis. Figure 1.3 illustrates these relationships.

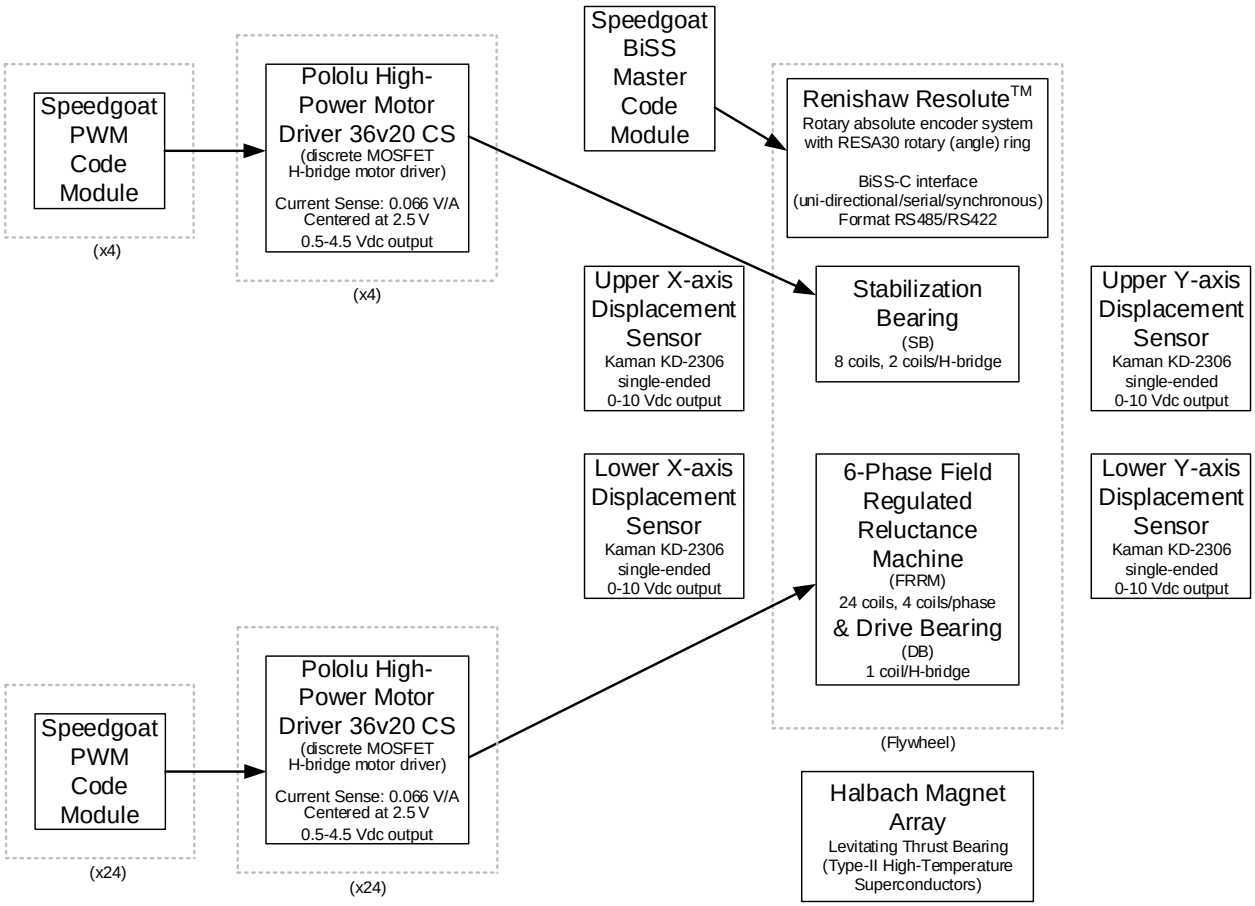

Figure 1.3 UI FESS Functional Block Diagram

1.3. UI FESS Sensors and Actuators Subsystems

1.3.1. *H-Bridge PWM Current Actuators*

The Pololu 36v20 current sensor (CS) discrete metal oxide semiconductor field effect transistor (MOSFET) H-bridge coil driver enables bidirectional control of one high-power coil. The compact 1.8×1.2-inch printed circuit board (PCB) assembly supports 24 volts direct current (Vdc) and is efficient enough to deliver a continuous 20 amperes (A) without a heat sink. The

integrated Allegro ACS714 Hall effect-based current sensor outputs an analog voltage proportional to the coil current (VIOUT).

1.3.2. *Hall Effect Current Sensors*

For I_{COIL} = 0 A, VIOUT is 2.5 V. The current sensor sensitivity is 66 mV/A. With increasing coil current, I_{COIL}, flowing in the direction from OUTA to OUTB, the VIOUT voltage increases from 2.5 V to 4.5 V. For I_{COIL} = 30 A, VIOUT is 4.5 V. With increasing coil current, I_{COIL}, flowing in the opposite direction, from OUTB to OUTA, the VIOUT voltage decreases from 2.5 V to 0.5 V. For I_{COIL} = -30 A, the VIOUT is 0.5 V.

1.3.3. *Non-Contact Eddy Current Displacement Sensors*

The Kaman KD-2306-9U is a non-contact linear displacement measurement system. The KD-2306 sensor signal conditioning electronics module supports the 9U sensor. This 9U sensor makes up one leg of a balanced inductive bridge circuit network. It produces a high-frequency magnetic field by applying a high-frequency (1-MHz) current to the leg of the bridge network inside the sensor head. If there is a conductive target within this magnetic field, then electromagnetic induction causes magnetic flux to pass over the surface of, and eddy currents to flow in, the conductive target. This causes the impedance of the leg of the bridge network to change. As the conductive target gets closer, the magnitude of the eddy current sensor oscillations decreases, and the rectified voltage is smaller. As the conductive target gets further away, the magnitude of the eddy current sensor oscillations increases, and the rectified voltage is larger. The 0- to 10-V output voltage is linearly proportional to the distance between the face of the 9U sensor and the stainless-steel conductive target. The measured displacement is 0 mm at 0 V and 3 mm at 10 V.

1.3.4. *Rotary Absolute Encoder*

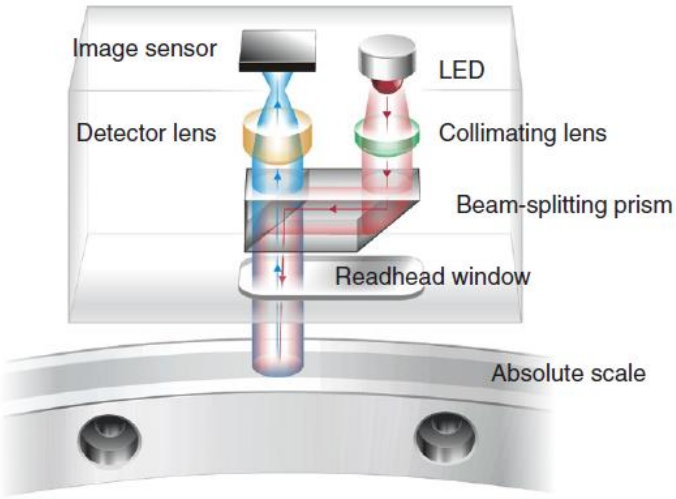

The Renishaw Resolute™ rotary absolute encoder system is a rotational position measurement system consisting of a miniature ultra-high-speed digital camera inside a stationary readhead and a stainless-steel ring with absolute scale code marked directly on the periphery.

The Resolute encoder calculates rotational position on demand. The readhead receives a series of request signals from the host control system (Speedgoat Performance Real-Time Target Machine). Each time it receives a request, the readhead determines rotational position by two independent methods: 1) decoding a single image without any information from previous positions, and 2) linear extrapolation from the two most recent rotational position readings, assuming constant velocity. Once the two rotational position methods have been calculated, the encoder decides which position to output and whether to set the error flag. If the positions calculated by the two methods agree within ±15 µm (half a scale period) of one another, then the encoder outputs the position from the first method and sets an internal counter to zero.

If the positions disagree, then the encoder outputs the position from the second method and increments the internal counter. If the internal counter ever exceeds four, then the readhead sets the error flag. The readhead makes sure that there is never more than 75 µs between images by capturing extra images between requests if necessary. For a system requesting a position every ≤ 75 µs, the time between outputting the first incorrect position and raising the error flag is five times the request interval. For a slower system requesting a position at 500 µs intervals, this time will be 500 µs, as the readhead will have processed six further images between each pair of requests to make sure that the time between images never exceeds 75 µs. In both cases, the time between outputting an incorrect position and raising the error flag is sufficiently short that appropriate action can be taken in response to the error flag before the incorrect rotational position data can influence the control system.

CHAPTER 2. LITERATURE REVIEW

Electric vehicles (EVs) have the potential to significantly reduce greenhouse gas emissions in the Pacific Northwest (PNW) and everywhere [1][2]. With the number of EVs on the rise, there is a need for adequate charging infrastructure to serve these vehicles [11]. Rural EV charging stations in the PNW based on abundant renewable energy and flywheel energy storage present both an opportunity and a challenge to significantly reduce greenhouse gas emissions.

EV users need access to charging services within the driving range of their EVs. Hence, there is a need to provide adequate access to charging facilities along different automotive transportation networks. Many of the routes along those transportation networks are isolated from the power grid and in some cases the expansion of the existing power grid to feed charging stations located along these routes may be impossible, costly, or impractical [3]. For instance, in the PNW many rural communities and national parks are accessible by long remote highways that are far from any nearby distribution-level power grid.

The planning of grid-tied EV charging stations has been extensively studied in recent literature [3]. In contrast, the planning of stand-alone EV charging stations, i.e., charging stations not connected to the electric grid, have not received as much attention.

A flywheel energy storage system (FESS) as a part of a fully green renewable energy storage system could minimize the operational costs of charging stations and their impacts on the peak demand of the hosting distribution power grid, if connected [7]. A FESS could also be part of a charging station not connected to the electric distribution power grid. For example, EV charging stations might use an energy storage system (ESS), e.g., flywheel ESS, and a renewable energy source (RES), e.g., photovoltaic (PV) modules. ESSs could store the energy generated from intermittent RESs to charge EVs when needed [2]. Combining an ESS and RES in a grid-connected charging station with islanding capability could improve EV charging availability and reliability. Although PV RESs are inherently intermittent because of diurnal and seasonal cycles and are also affected by cloud cover [10], locations with an adequate PV RES and ESS could operate in an islanded state indefinitely.

An EV charging station may offer multiple charging options, including, from slowest to fastest, ac level 1, i.e., 120 Vac charging; ac level 2, i.e., 240 Vac charging; dc fast charging; and battery swapping [4][15]. Level 1 and level 2 ac charging are only available from power grid-

connected EV charging stations unless an inverter is used on the dc bus of an off-grid EV charging station. The trends among the first three options are toward level 2 ac charging at a home or residence and toward dc fast charging at public EV charging stations, with a continual push for faster charging. A full battery swap should take 10 minutes or less in comparison to a plug-in EV charge, which can take 30 minutes to a few hours. The key point is that a rural EV charging system with combined RES and ESS, as envisioned in this study, could offer multiple charging options and hence would not be limited to providing a particular charging option. Such a proposed solution would be flexible and could be optimized toward reducing EV user waiting time.

The lack of public charging infrastructure is a major factor in the slower adoption of EVs in rural areas in the PNW. Dc fast charging increases EV user convenience by reducing charging time. High capital costs and uneven power demand are challenges to deploying EV dc fast charging stations. These issues have been studied in three types of areas—urban, suburban, and rural—within the Columbus, Ohio, region [5]. Ucer et al. [5] decried a 12-minute maximum queuing time for urban areas but were not overly concerned about the 30-minute average queuing duration for rural areas, the 276-minute (over 4 ½ hours) maximum queuing time for rural areas notwithstanding. It is likely that the authors did not live in a rural area. Long queuing durations like these will only further retard the adoption of EVs in rural areas. The suppressed demand due to either long driving distances to get to a charging station or long waiting times (queuing duration) was the focus of consideration by Gan et al. [8]. The authors used both spatial and temporal penalties (costs) to capture the nature of EV users' charging behaviors. Their claimed result was a fixed-point equation formulated as a nonlinear integer problem, which determined the optimal locations (i.e., spatial solution) and optimal number of charging ports (i.e., the equivalent to "pumps" at a gas station).

EV user waiting time (queuing duration) modeling leads to the question of optimal capacity sizing for EV charging systems. Ugirumurera and Haas [6] studied the optimal sizing of a complete green charging system that relied entirely on the power generated by RES, specifically by solar panels. Their work can be used to determine the optimal resource size (e.g., the number of solar panels and the energy-storage capacity) that would minimize the charging system's costs while meeting performance metrics. For grid-connected EV charging stations, work by Negarestani et al. [7] can be used to determine the optimal size of the ESS for an EV dc

fast charging station to minimize station energy costs and ESS costs. The approach by Negarestani et al. [7] considered various technical and economic constraints, such as energy loss and the life cycle cost of the ESS.

In economics, competition exists when multiple companies compete for customers. Basic economic theory suggests that when firms must compete for customers, the competition leads to lower prices, higher quality goods and services, greater variety, and more innovation. Duan et al. [9] examined the situation when multiple fast charging service providers participated in the investment of EV fast charging (dc) stations in competition with one another. They proposed a methodology to optimize EV user queuing time and fast charging station location and number of charging ports. Of interest for this study's work is a charging station-level model to obtain the optimal sizes and operation scheduling of on-site (at a charging station) ESSs. This could be useful in future scaling of our ESS.

Focusing on the major challenge to widespread EV adoption, namely a refueling experience similar to that of gasoline vehicles, Tu et al. [11] reviewed emerging extreme fast-charging technologies. Despite significant Li-ion battery technology advancements in the last five years, the energy density of the Li-ion batteries is 40 times lower than the energy density of petroleum. Despite falling costs and major improvements in performance, Li-ion battery degradation at rest and during cycling, charging rate limitations due to the electrochemical processes, and limited energy density (compared with petroleum) still pose major challenges to more widespread EV adoption [11]. Beyond Li-ion battery technology limitations, a key remaining challenge for the extensive adoption of EVs is the lack of refueling infrastructure. This is especially true in rural areas such as in the PNW. "Extreme" dc fast-charging refers to the grouping of dc fast charging ports. High power transfer rates are required to speed up EV charging. Designing and building a system that can deliver such high power becomes increasingly challenging and costly. A grid-connected dc fast-charging station may require electrical service upgrades such as a transformer and a feeder, conditioning of the ground surface, conduits from the power source to the service transformer and from the transformer to the fast-charging port, material costs, permits, and administration. The key idea of "extreme" dc fast-charging is for multiple charging ports to share the same costly upstream equipment, thereby spreading the construction overhead over multiple charging ports [11]. While Tu et al. [11] noted that this sharing can reduce the dc fast-charging stations' footprint in densely populated areas,

this sharing is more important for cost reduction in rural dc fast-charging station locations, where cost rather than footprint is likely to be the most significant constraint.

At the ESS level, Figure 1.2 shows that the ideal UI FESS operation will maintain a constant dc bus voltage. To use the dc bus voltage to charge an EV will require dc to dc conversion. These converters would interface between the dc bus voltage, which is the output of an ESS, and the EV charging port. Isolated dc-dc converters with galvanic isolation are commonly used in EV battery chargers. He and Khaligh [16] considered a vehicle-to-grid concept in which EVs could be considered as distributed power sources to store and send power back to the grid. This would allow EVs to provide voltage and frequency regulation to the grid, absorb excess electricity, and deliver power to the grid during periods of high demand. The vehicle-to-grid capability would require EVs to have bidirectional charging systems. While vehicle-to-grid capability is not the immediate intent of the UI FESS typical application, unidirectional isolated dc-dc converters would be necessary to interface the RES with the dc bus voltage and the EV charging port with the dc bus voltage. For unidirectional grid-to-vehicle chargers, inductor-inductor-capacitor (LLC) converters are commonly selected as the dc–dc stages [16].

In rural EV charging station applications, ESSs may be required to efficiently store energy for longer periods of time than their urban counterparts. The nature of RESs also means that they need efficient, longer-term ESSs. Pei et al. [17] extolled the benefits of magnetic bearings because they are frictionless, pollution-free, and maintenance-free,. They noted that active magnetic bearing machines, sometimes called bearingless machines, are becoming increasingly attractive in applications such as flywheel ESSs. A 5-degree of freedom active magnetic bearing for flywheel ESS was described by Li et al. [18]. Flywheels have great potential for fast charging for EVs. For grid-connected fast-charging stations, using ESSs will reduce the cost of infrastructure upgrades, e.g., transformers and feeders, etc. In comparison with other ESS technologies such as Li-ion batteries, flywheels have longer life cycles and higher power density [18]. Other advantages include operating under low/high temperatures, an accurate state of charge, and recyclability [19].

CHAPTER 3. SINGLE-AXIS ACTIVE-MAGNETIC-BEARING ACADEMIC TEST FIXTURE

A single-axis active-magnetic-bearing (AMB) academic test fixture (Figure 3.1) was created to help develop, test, and improve the AMB control software and hardware used for the University of Idaho (UI) flywheel energy storage system (FESS). The single-axis AMB academic test fixture served as an intermediate step before the design and implementation of the more complex field regulated reluctance machine (FRRM) AMB and stabilization AMB in the UI FESS.

The single-axis AMB academic test fixture had a “U”-shaped electromagnet. The coil consisted of 150 turns of 18 American wire gauge (AWG) solid core copper wire coated with a thin layer of enamel insulation. The flotor was free to translate up and down along the vertical axis. The iron core of the electromagnet was M36 electrical steel (μr = 1616).

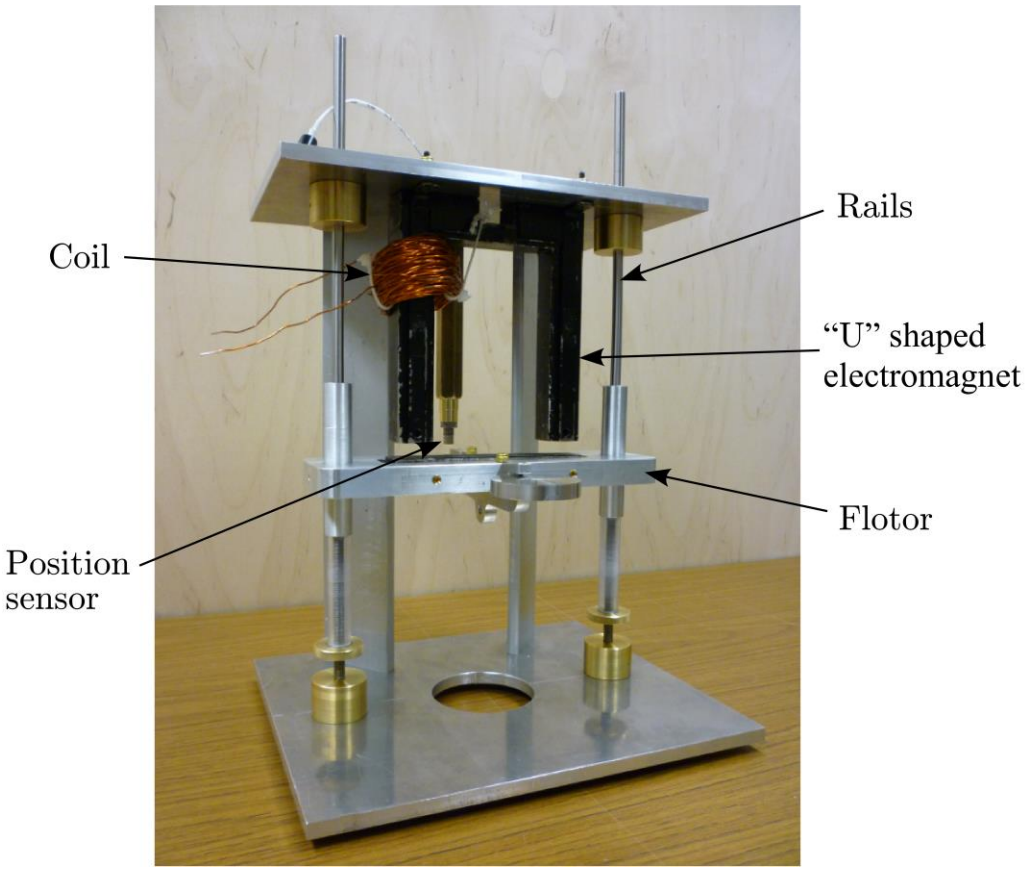

Figure 3.1 Single-Axis Active-Magnetic-Bearing Academic Test Fixture

The “U” electromagnet was oriented to impose an attractive magnetic force on the flotor, against the force of gravity. The flotor was fixed to rails with mechanical bearings.

A discrete MOSFET H-bridge coil driver enabled bidirectional electro-magnet coil current control. A Hall-effect current sensor measured electro-magnet coil current, and a non-contact Eddy current displacement sensor was used to measure the air gap.

Each sensor and actuator interface is described and documented in upcoming chapters for integration into the flywheel energy storage system.

CHAPTER 4. H-BRIDGE PULSE WIDE MODULATION (PWM) CURRENT ACTUATOR

The single-axis active-magnetic-bearing (AMB) academic test fixture electro-magnet coil current was actuated by one Pololu 36v20 CS [20] (Figure 4.1). This discrete MOSFET H-bridge coil driver enables bidirectional current control of one high-power coil, i.e., the electro-magnet coil. The compact 1.8×1.2-inch PCB assembly supports 24 Vdc and is efficient enough to deliver up to a continuous 20 A without a heat sink (at room temperature).

The H-bridge is made up of one N-channel MOSFET [21] per leg, and most of the board's performance is determined by these MOSFETs. The rest of the board contains electrical circuitry to take 5V transistor transistor logic (TTL) digital inputs, pulse width modulation (PWMH) and direction (DIR), and it controls the MOSFETs.

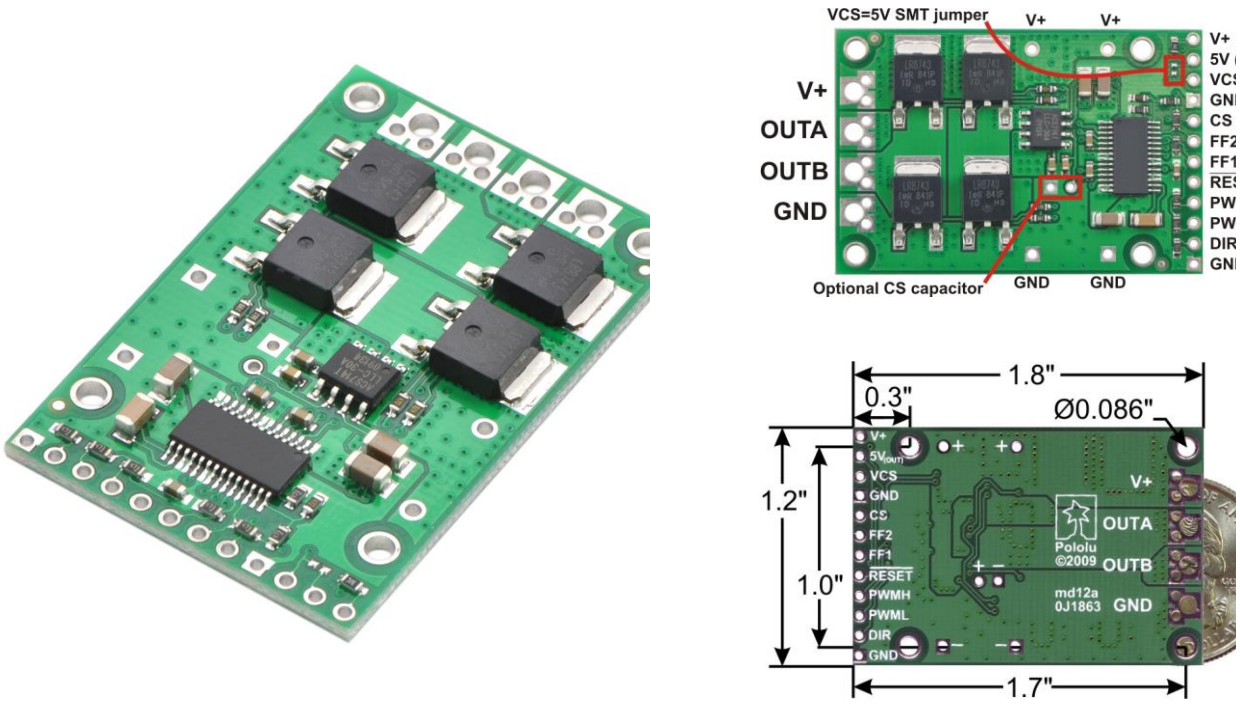

Figure 4.1 Pololu High-Power Motor Driver 36v20 CS [20]

During the active (high) portion of the PWMH 5V TTL signal, the full dc bus voltage is applied across the machine coil in the polarity or direction determined by the DIR 5V TTL signal; during the low portion of the PWMH 5V TTL signal, both sides of the machine coil are connected or shorted to the dc bus negative terminal (Figure 4.2).

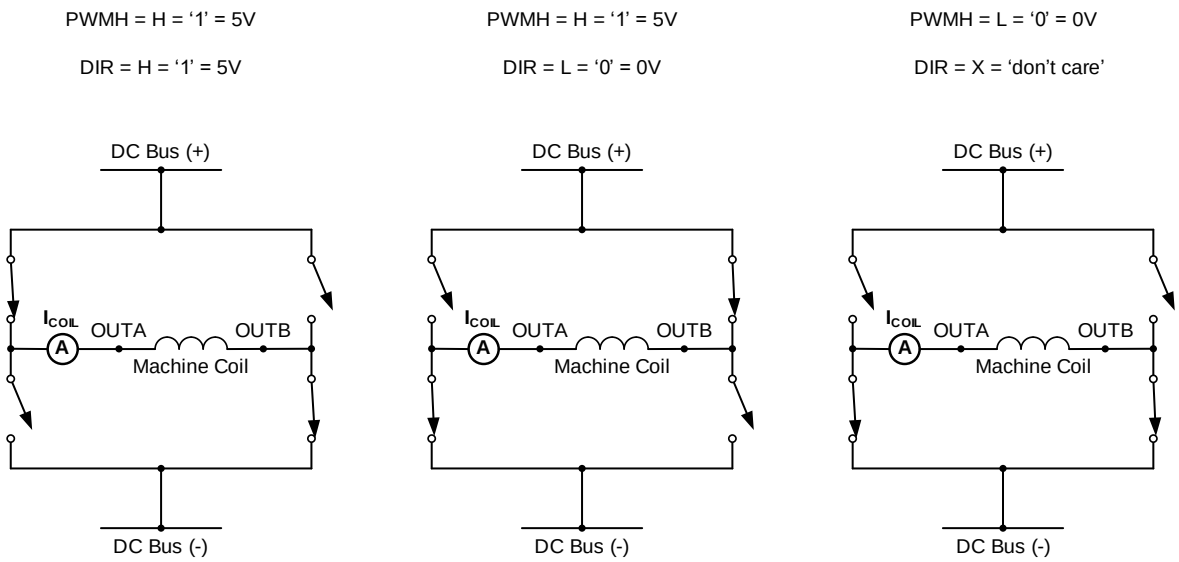

Figure 4.2 Pololu High-Power Motor Driver 36v20 CS [20] Operation Modes

When DIR = '1' the polarity or direction is from OUTA to OUTB. When DIR = '0' the polarity or direction is from OUT B to OUT A (Figure 4.3).

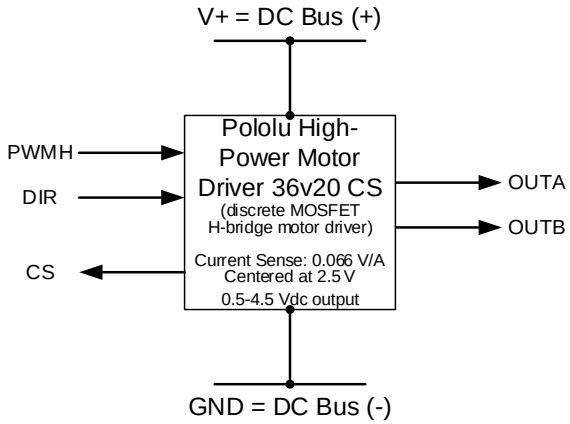

Figure 4.3 Pololu High-Power Motor Driver 36v20 CS [20] Functional Block Diagram

4.1. Pololu 36v20 CS: N-Channel MOSFET

The Pololu 36v20 CS H-bridge is made up of one N-channel MOSFET per leg, and most of the board's performance is determined by these MOSFETs. The MOSFETs are all Infineon IPD048N06L3 G OptiMOS™3 power transistors [21] (Figure 4.4) in a TO-252, also known as a DPAK, package. The key parameters are shown in Table 4.1.

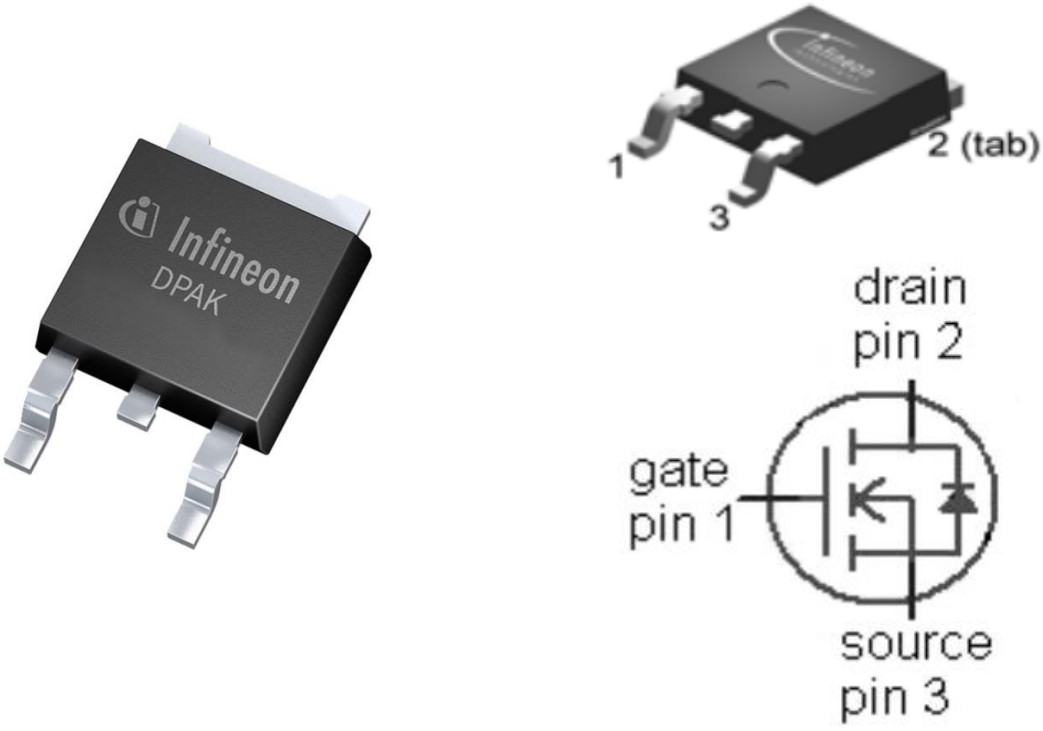

Figure 4.4 Infineon IPD048N06L3 G OptiMOS™3 Power Transistor [21]

Table 4.1 Infineon IPD048N06L3 G Parameters

Parameter	Value	Unit	Notes
$V_{DS,MAX}$	60	V	
$R_{DS(ON),MAX}$	4.8	mΩ	max per H-bridge leg
$I_{D,MAX}$	90	A	at 25°C, infinite heatsink current limited by bond wire
	15	A	at 105°C, no heatsink, minimal footprint
θ_{JA}	62	K/W	minimal footprint
$T_{J,MAX}$	175	°C	operating and storage

Note 1: Infineon IPD048N06L3 G Parameters shown here are from [21].

4.2. Pololu 36v20 CS: Allegro Microsystems A3941 Full Bridge MOSFET Driver

The Allegro MicroSystems LLC A3941 is a full-bridge controller for use with external N-channel power MOSFETs (Figure 4.5) and is specifically designed for applications with high-power inductive loads, such as motor-generator coils and/or windings.

An integrated switched capacitor charge pump regulator provides full (> 10 V) gate drive to external N-channel MOSFETs, even the high-side external N-channel MOSFETs. This internal charge pump allows dc (100 percent duty cycle) operation.

The power MOSFETs are protected from shoot-through current by an external resistor adjustable deadtime. Integrated diagnostics provide indication of undervoltage, overtemperature, and H-bridge faults.

The A3941 integrated circuit (IC) is packaged in a 28-pin thin shrink small outline package (TSSOP) with an exposed thermal pad.

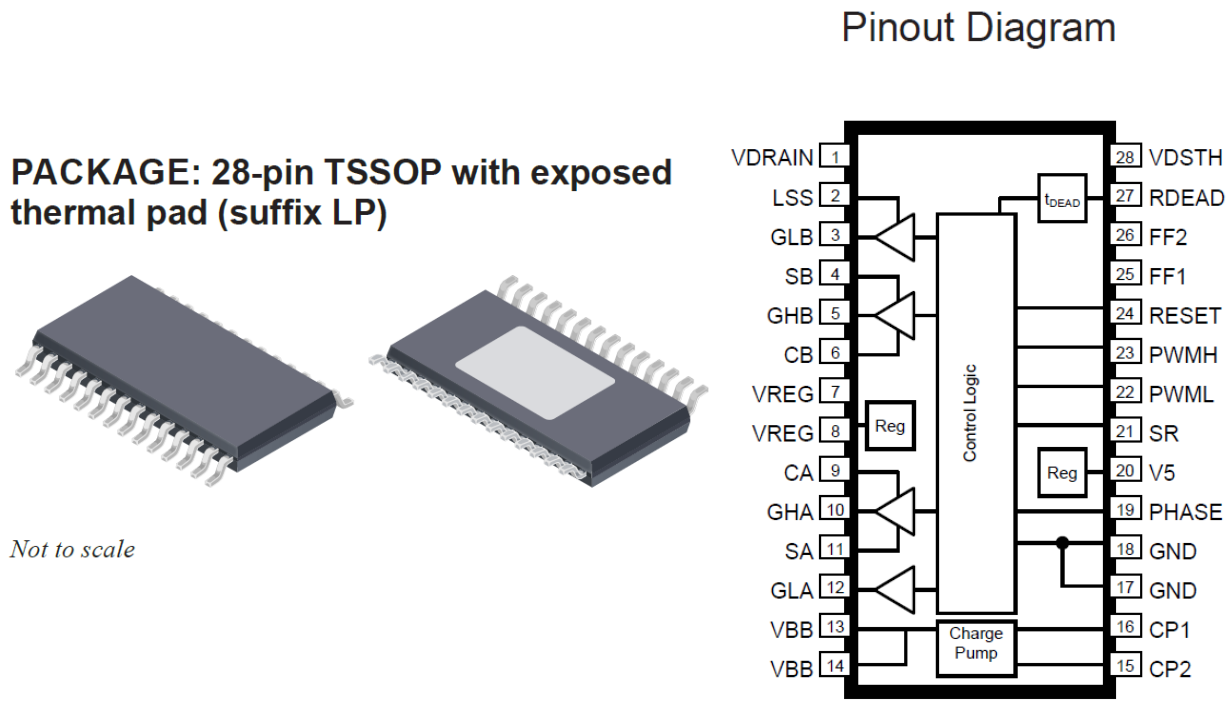

Figure 4.5 Allegro MicroSystems LLC A3941KLPTR-T Full Bridge MOSFET Driver [22]

The A3941 (Figure 4.6) is a full-bridge MOSFET driver requiring a single unregulated supply of 7 to 50 V. It includes an integrated 5-V logic supply regulator. The A3941 includes all the necessary circuits to ensure that the gate-to-source voltages of both high-side and low-side

external power MOSFETs are above 10 V, at supply voltages down to 7 V. A single power supply connection is required to the voltage base base (VBB pin.

The A3941 can be driven with PWM control signals. Cross-conduction (shoot-through current) in the external H-bridge is avoided by a resistor adjustable dead time.

The A3941 includes a number of protective features against undervoltage, overtemperature, and power bridge faults. Fault states enable responses by the device or by the external controller, depending on the fault condition and logic settings. Two fault flag outputs, FF1 and FF2, are provided to signal detected faults to an external controller.

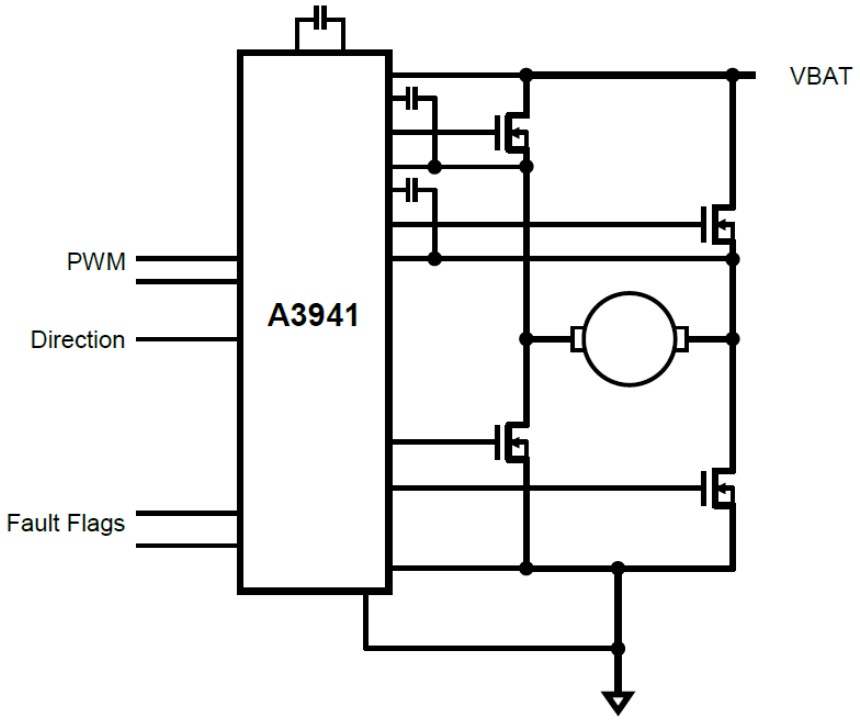

Figure 4.6 Allegro MicroSystems LLC A3941 Full Bridge MOSFET Driver Typical Application

The A3941 is designed to drive external, low on-resistance, power N-channel MOSFETs. It supplies the large transient currents necessary to quickly charge and discharge the external field-effect transistor (FET) gate capacitance to reduce dissipation in the external FET during switching. The charge and discharge rate can be controlled using an external resistor in series with the connection to the gate of the FET.

The A3941 provides two PWM control signals and a phase control for the current direction. A PWM signal is applied to PWMH, and PWML is tied high. The PHASE input is

required to reverse the current direction. The PHASE input of A3941 is the DIR input of the Pololu 36v20 CS.

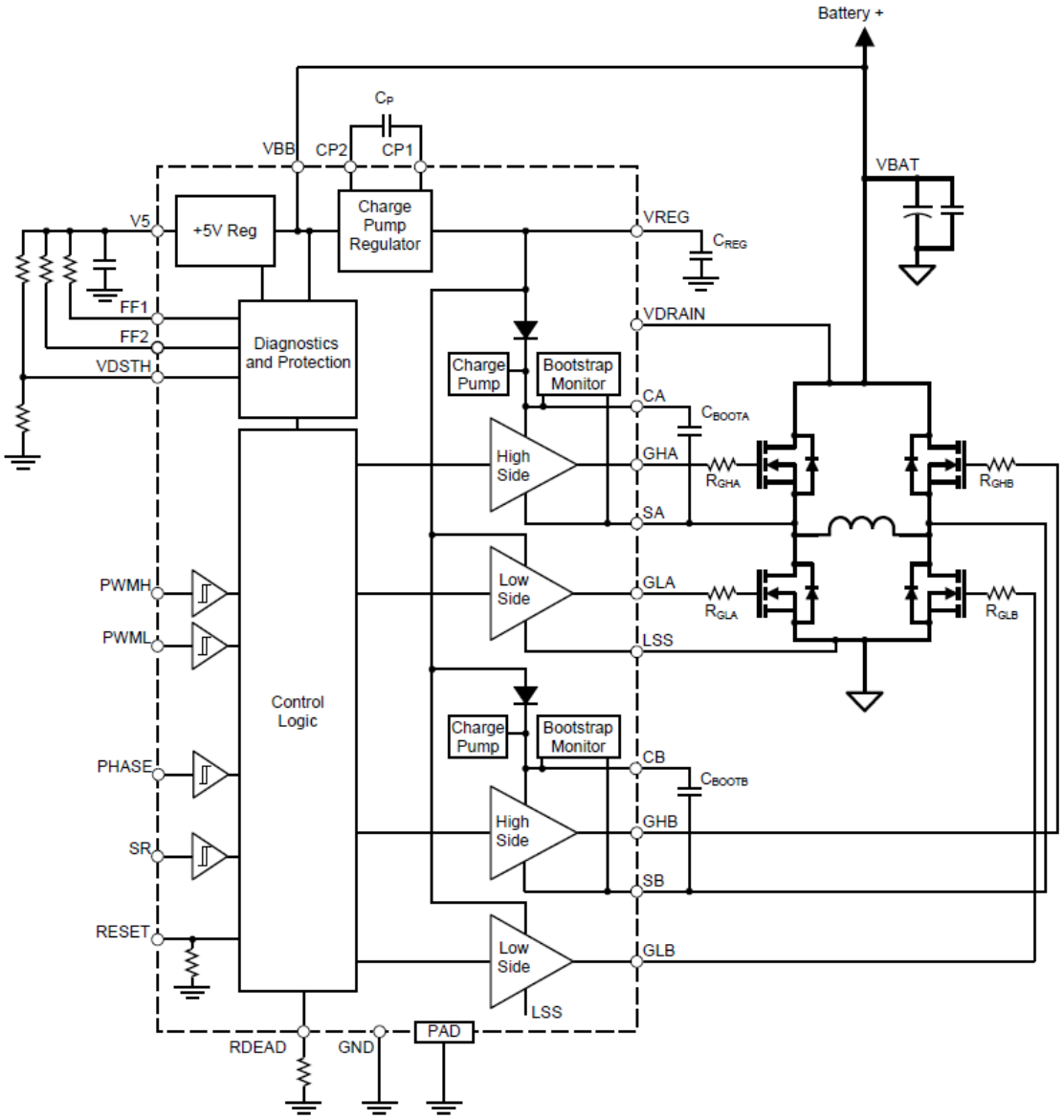

Figure 4.7 Allegro MicroSystems LLC A3941 Full Bridge MOSFET Driver Functional Block Diagram

When PWMH is high and DIR is high, then GHA is high and GLB is high, as shown in in Figure 4.7 (bridge driven with A high and B low).

When PWMH is high and DIR is low, then GHB is high and GLA is high, as shown in in Figure 4.7 (bridge driven with B high and A low).

When PWMH is low, DIR is “don’t care,” then GLA is high and GLB is high, as shown in in Figure 4.7. In this case the high-side MOSFETs are switched off during the current decay time (PWMH off-time) and the coil current recirculates through the low-side MOSFETs.

This control configuration is commonly referred to as high-side chopping or high-side PWM.

CHAPTER 5. HALL-EFFECT CURRENT SENSOR

The Pololu High-Power Motor Driver 36v20 CS board includes a current sensor IC, the Allegro Microsystems ACS714LLCTR-30A-T (Figure 5.1) [24]. The integrated Allegro ACS714 Hall-effect current sensor IC outputs an analog voltage, VIOUT, proportional to the electro-magnet coil current. This current sensor can measure bi-directional current with a magnitude of up to ±30 A.

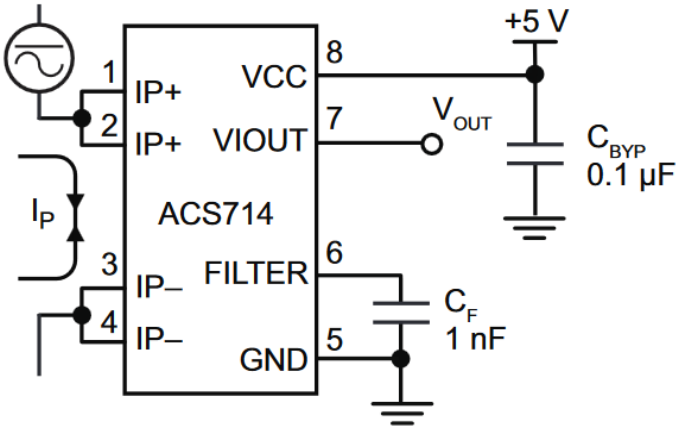

Figure 5.1 ACS714LLCTR-30A-T Typical Application

For I_{COIL} = 0 A, VIOUT is VCC/2 = 2.5V, where VCC = +5Vdc (nominal). The current sensor sensitivity is 66 mV/A. With increasing coil current, I_{COIL}, flowing in the direction from OUTA to OUTB, the VIOUT voltage increases from 2.5 V to 4.5 V. For I_{COIL} = 30 A, VIOUT is 4.5 V. With increasing coil current, I_{COIL}, flowing in the opposite direction, from OUTB to OUTA, the VIOUT voltage decreases from 2.5 V to 0.5 V. For I_{COIL} = -30 A, the VIOUT is 0.5 V.

VIOUT = (IP)*(66 mV/A) + (VCC/2)

= (IP)/(15 A/V) + (2.5V)

where IP is the current from OUTA to OUTB. The measured current is

IMEAS = (VIOUT – 2.5V)/(66 mV/A)

= (VIOUT – 2.5V)*(15 A/V)

The electrical current sensor's mathematical model is well defined and is based on the manufacturer's data for the actual hardware. The current sensor's ratiometric output sensitivity to the current sensor's 5V supply voltage (VCC) warrants careful selection of a 5V power source.

This is an example of a small but important hardware implementation detail that was observed during physical hardware testing.

Table 5.1 Hall-Effect Current Sensor: Allegro ACS714LLCTR-30A-T [24]

Allegro Part Number	VCC (V)	Current Measurement Range (A)	Sensitivity (mV/A)	Operating Temperature Range	Bandwidth (kHz)	Package	Cost ea. (Digi-Key 3k reel)
ACS714LLCTR-30A-T	5	±30	66	-40 to 150°C	80	8-pin SOIC	$2.46

5.1. Pololu 36v20 CS: Allegro Microsystems ACS714 Current Sensor

The Pololu High-Power Motor Driver 36v20 CS [20] board includes a current sensor IC, the Allegro Microsystems ACS714LLCTR-30A-T [24]. The Allegro ACS714 device consists of a linear Hall effect sensor with a copper conduction path located near the surface of the die. Applied current flowing through this copper conduction path generates a magnetic field that the Hall IC converts into a proportional voltage. The ACS714 outputs an analog signal, V_{IOUT}, that varies linearly with the bi-directional electro-magnet coil current, I_{COIL}. V_{IOUT} is the current sensor (CS) output of the Pololu High-Power Motor Driver 36v20 CS [20] board. For I_{COIL} = 0 A, the CS output is 2.5 V. The ACS714LLCTR-30A-T device sensitivity is 66 mV/A. With increasing coil current, I_{COIL}, flowing in the direction from OUTA to OUTB, the CS output voltage increases from 2.5 V to 4.5 V. For I_{COIL} = 30 A, the CS output is 4.5 V. With increasing coil current, I_{COIL}, flowing in the opposite direction, from OUTB to OUTA, the CS output voltage decreases from 2.5 V to 0.5 V. For I_{COIL} = -30 A, the CS output is 0.5 V. The current sensor measurement error is ±1.5 percent at 25°C and ±5 percent from -40°C to 150°C [24].

The Allegro Microsystems ACS714LLCTR-30A-T [24] senses ac or dc current using a Hall element. Device performance characteristics are specified over the operating temperature range of -40 to 150°C. The Hall current drive, shown in Figure 5.2, forces a known Hall current through the Hall element. The Hall voltage output from the Hall element is proportional to the magnetic field from the primary current flowing through the copper conduction path.

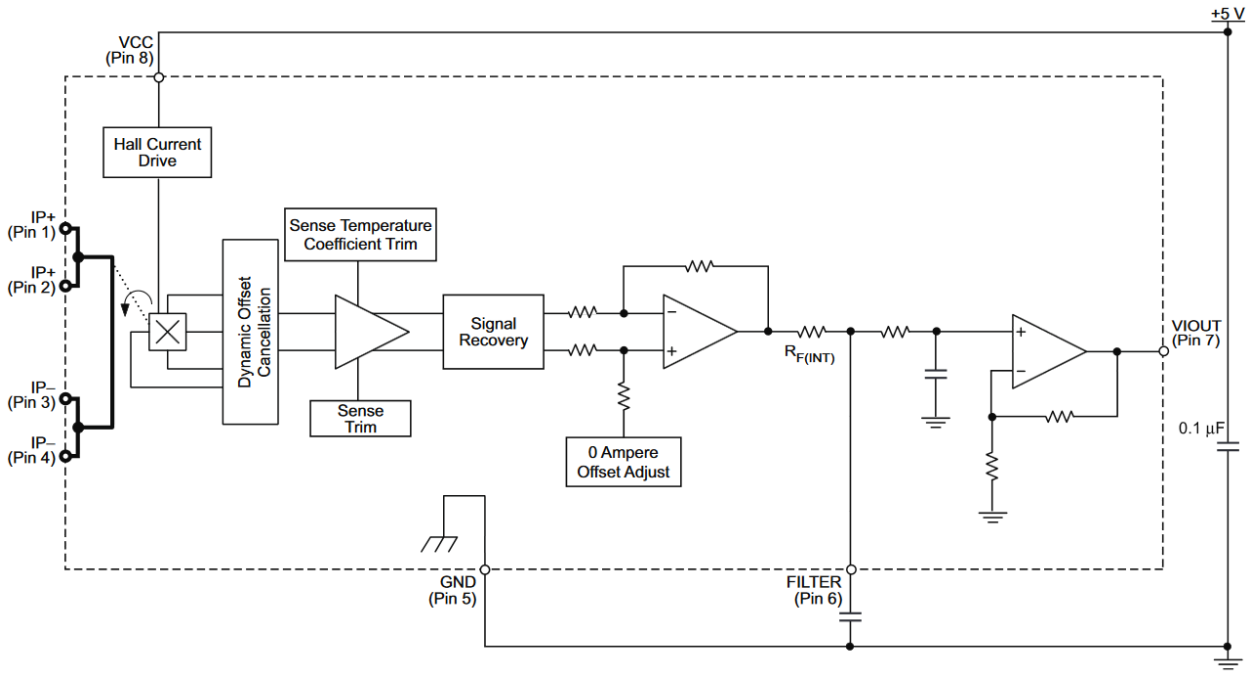

Figure 5.2 ACS724KMATR-20AB-T Functional Block Diagram

The Hall voltage is amplified by a temperature compensated gain (sensitivity). An integrated filter resistance, $R_{F(int)}$, can be combined with an external capacitor to RC low-pass filter the amplifier output before the non-inverting output buffer. The device V_{CC} = +5V, and the analog output voltage is nominally $V_{CC}/2$ = 2.5 V with I_P = 0A. With a ±30 A I_P measurement range, the sensitivity is 66 mV/A and the analog output voltage range is 0.5 to 4.5 V.

CHAPTER 6. NON-CONTACT EDDY CURRENT DISPLACEMENT SENSOR

A single Kaman KD-2306-9U non-contact Eddy current displacement sensor (Figure 6.1) was used to measure the air gap. The output of the KD-2306-9U is an analog voltage, VOUT.

$$V_{OUT} = \left(\frac{1\,V}{0.3\,mm}\right) \times (displacement[mm])$$

The Kaman KD-2306 is a non-contact, linear, analog displacement measuring system. The system operates on a traditional inductive bridge circuit. This system can be utilized for precision static and dynamic measurements of conductive targets.

The 0 to 10 V analog output voltage, VOUT, was linearly proportional to the distance between the face of the displacement sensor and the 303 stainless-steel conductive target on the flotor assembly. VOUT = 8.333 V for a displacement of 2.5 mm, VOUT = 5 V for a displacement of 1.5 mm, and VOUT = 1.667 V for a displacement of 0.5 mm.

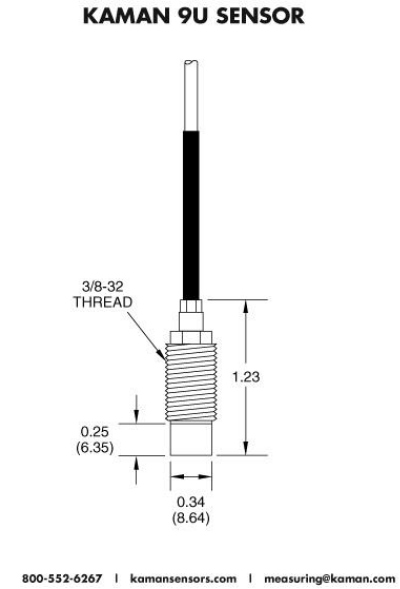

Figure 6.1 Kaman 9U Sensor [27]

6.1. Kaman KD-2306-9U

The Kaman KD-2306-9U is a non-contact linear displacement measurement system. The KD-2306 sensor signal conditioning electronics module supports the 9U sensor. This 9U sensor makes up one leg of a balanced inductive bridge circuit network. It produces a high-frequency magnetic field by applying a high-frequency (1-MHz) current to the leg of the bridge network inside the sensor head. If there is a conductive target within this magnetic field, then

electromagnetic induction causes magnetic flux to pass over the surface of, and eddy currents to flow in, the conductive target. This causes the impedance of the leg of the bridge network to change.

As the conductive target gets closer, the magnitude of the eddy current sensor oscillations decreases and the rectified voltage is smaller. As the conductive target gets further away, the magnitude of the eddy current sensor oscillations increases and the rectified voltage is larger. The 0 to 10-V output voltage was linearly proportional to the distance between the face of the 9U sensor and the 303 stainless-steel conductive target on the flotor assembly. The measured displacement was 0 mm at 0 V and 3 mm at 10 V (see tables 6.1 and 6.2).

Table 6.1 Kaman KD-2306-9U Displacement vs Output Voltage

Displacement	Output Voltage
0.0 mm	0.000 Vdc
0.5 mm	1.667 Vdc
1.5 mm	5.000 Vdc
2.5 mm	8.333 Vdc
3.0 mm	10.000 Vdc

Table 6.2 Kaman KD-2306-9U Parameters

Parameter	Value	Unit	Notes
Output	0 – 10	Vdc	
Resolution	0.01	%FS	Full Scale (FS) is 4 mm 0.01% of 4 mm is 0.4 µm
Static Resolution	0.4	µm	
Measuring Range	0 – 4 0 – 3	mm mm	Uncalibrated Calibrated
Offset	1	mm	Calibrated offset
Integral Cable Length	6 ½	ft	6.5 ft = 2 m
Operating Temperature Range (Electronics)	0 to 55	°C	
Operating Temperature Range (9U sensor)	cryogenic to 200	°C	
Frequency Response	50	kHz	-3dB point
Power Supply Requirements Voltage Voltage Regulation Current	 +15 to +30 ±0.5 150	 Vdc Vdc mAdc	 Maximum
Terminal Screw Torque	7	lb-in	Maximum 7 lb-in = 0.8 N-m

Note 1: Kaman KD-2306-9U Parameters shown here are from [25][26].

The KD-2306-9U consists of two subassemblies: a 9U sensor with an integral cable, and the KD-2306 signal conditioning electronics module in a DIN mounting enclosure (Figure 6.2). The system is preconfigured at the factory for a particular sensor (9U), cable length (6 ½ feet), target material (303 stainless steel), and calibrated measuring range (0 to 3 mm, 1-mm offset).

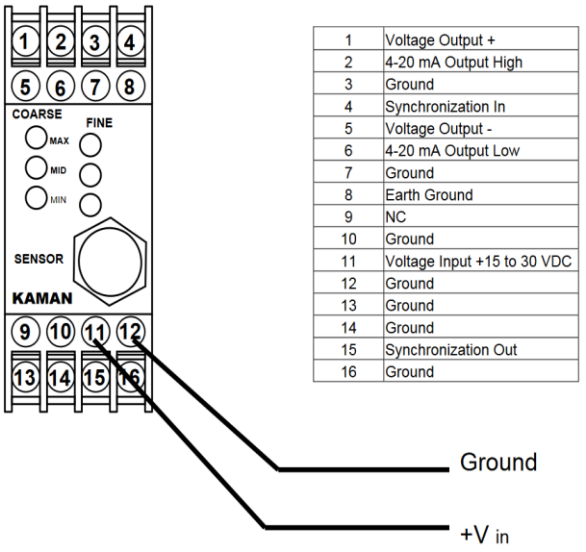

1	Voltage Output +
2	4-20 mA Output High
3	Ground
4	Synchronization In
5	Voltage Output -
6	4-20 mA Output Low
7	Ground
8	Earth Ground
9	NC
10	Ground
11	Voltage Input +15 to 30 VDC
12	Ground
13	Ground
14	Ground
15	Synchronization Out
16	Ground

Input Power Supply Connections

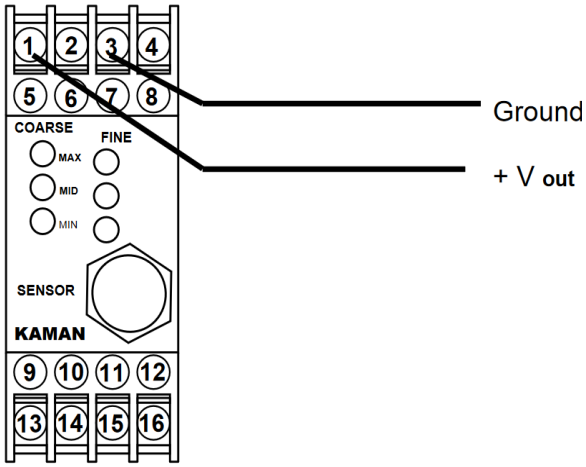

Single Ended Voltage Output

Figure 6.2 Kaman KD-2306 [25][26]

Input power was connected to terminals 11 and 12, as shown. A 15- to 30-Vdc ±0.5 Vdc and 150 mA capable supply was required. The single-ended voltage output was from terminal 1 to terminal 3, as shown.

CHAPTER 7. SINGLE-AXIS ACTIVE-MAGNETIC-BEARING DYNAMIC PLANT MODEL

This chapter describes the development of a dynamic plant model for the single-axis active-magnetic-bearing (AMB) academic test fixture. A plant model may be created by directly specifying a model or with system identification techniques using measured data. The single-axis AMB plant model was directly specified. While initial plant model parameter values may be calculated, refining some of these parameter values on the basis of the measured data may improve overall performance.

7.1. Equations of Motion

The H-bridge PWM current actuator applies a voltage across the electro-magnet coil. The equilibrium equation for the voltage across the electro-magnet coil is

$$e = L\frac{di}{dt} + k_b v + iR$$

where L is the electro-magnet coil inductance, k_b is a counter-electromotive force constant, v is the velocity of the flotor, i is the electro-magnet coil current, and R is the electro-magnet coil resistance. Expanding each term with a constant and a change, delta, results in

$$e + \Delta e = (L + \Delta L)\left(\frac{di}{dt} + \Delta\frac{di}{dt}\right) + (k_b + \Delta k_b)(v + \Delta v) + (i + \Delta i)(R + \Delta R)$$

Assuming L, k_b, and R are constants, and subtracting out the equilibrium equation, results in

$$\Delta e = L\Delta\frac{di}{dt} + k_b\Delta v + \Delta iR$$

which gives the voltage change or delta as a function of constants L, k_b, and R, and dynamic variables $\Delta\frac{di}{dt}$, Δv, and Δi.

The force of the electromagnet is proportional to the square of the electro-magnet coil current over the square of the gap or distance between the stationary "U" shaped electro-magnet and the flotor.

$$F = k_f\frac{i^2}{g^2}$$

Applying the same approach to this equilibrium equation results in

$$\Delta F = \frac{k_f 2i}{g^2}\Delta i - \frac{k_f 2i^2}{g^3}\Delta g$$

which gives the force change or delta as a function of constants k_f, i, and g and dynamic variables Δi and Δg. Note that a parameter x may have a constant portion x and a dynamic portion Δx.

At equilibrium, the force of gravity on the flotor is equal to the applied force of the electro-magnet.

$$F_{applied} - F_{gravity} = m\alpha$$

Applying the same approach to this equilibrium equation results in

$$\Delta F = (1 + \mu)m\Delta\alpha$$

which gives the change or delta in the flotor acceleration due to the change or delta in applied force. The flotor mass and coefficient of friction are assumed constant, and the dynamic variable is Δα.

7.2. Dynamic Plant Model Block Diagram

Using the equations of motion described in section 7.1, a block diagram of the single-axis AMB dynamic plant model was developed, as shown in Figure 7.1.

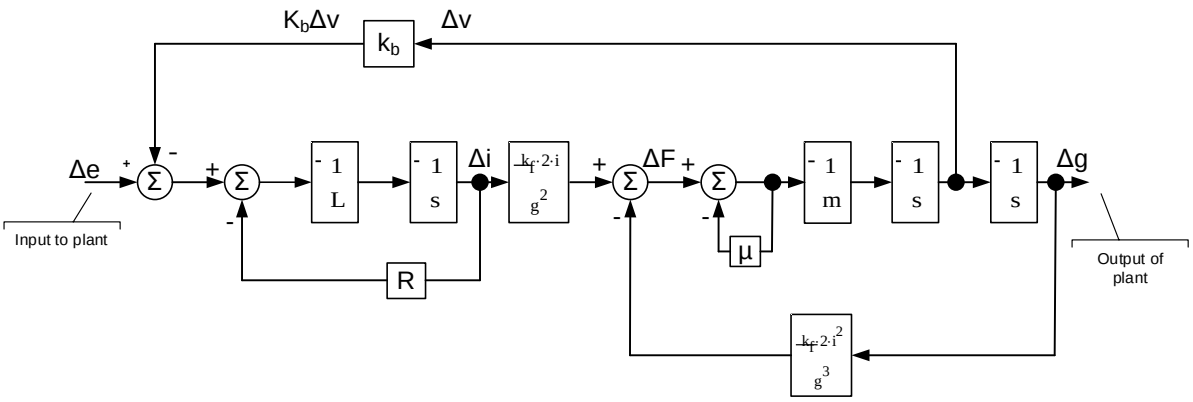

Figure 7.1 Single-Axis Active-Magnetic-Bearing Dynamic Plant Model Block Diagram

The input to the plant is a change in voltage, Δe, applied to the electro-magnet coil by the discrete MOSFET H-bridge. The output of the plant is the change in gap, Δg, between the face of the non-contact Eddy current displacement sensor and the 303 stainless-steel conductive target on the flotor assembly.

CHAPTER 8. SINGLE-AXIS ACTIVE-MAGNETIC-BEARING CONTROL SYSTEM DEVELOPMENT

This chapter describes a single-axis active-magnetic-bearing control system that was designed, built, and tested (Figure 8.1). The system model forms the basis for control system design. This model provides a basis from which to calculate appropriate commands and then enables understanding of the subsystems shown in previous chapters of this report to achieve appropriate signals and energy inputs for powering and controlling the single axis magnetic bearing plant.

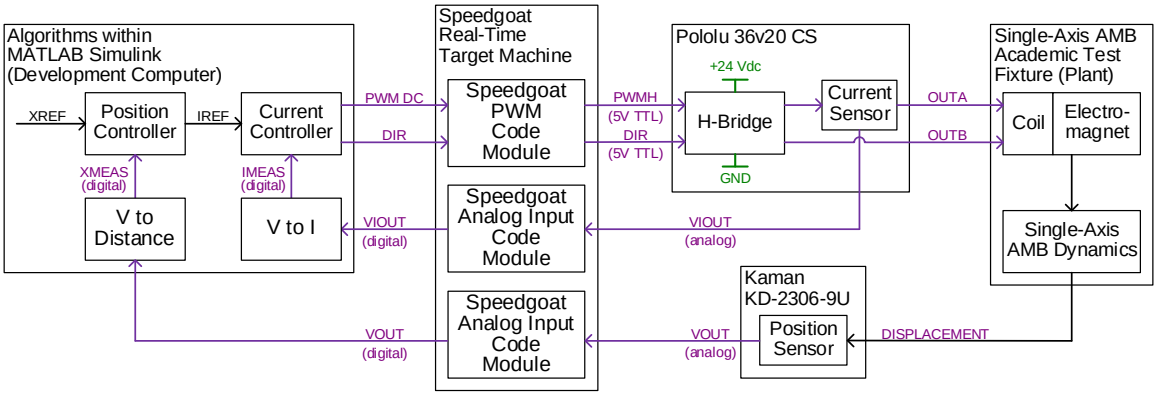

Figure 8.1 Single-Axis Active-Magnetic-Bearing Academic Test Fixture Block Diagram

This single-axis active-magnetic-bearing (AMB) test fixture implements a hardware-in-the-loop (HIL) with MATLAB Simulink Real-Time models. A Speedgoat performance real-time target machine connects a development computer running MATLAB Simulink with hardware consisting of one actuator and two sensors. It allows the coil current to be actuated by an H-bridge and measured by a current sensor. The displacement of the single-axis AMB is measured by a displacement sensor.

This single-axis AMB test fixture allows for prototyping current and position controllers in MATLAB Simulink.

8.1. Design

A proportional-integral (PI) controller for the single-axis AMB academic test fixture was designed and simulated in MATLAB Simulink with HIL. Tables 8.1 through 8.9 describe features of the system.

Table 8.1 Current Controller Signals

Name	Direction	Data Type	Description
IREF	In	Double	Reference current
IMEAS	In	Double	Measured current
PWM DC	Out	Double	Commanded PWM duty cycle between 0 (0% duty cycle) and 1 (100% duty cycle).
DIR	Out	Boolean	Commanded direction of current flow. DIR = '1' means current flows from OUTA to OUTB. DIR = '0' means current flows from OUT B to OUT A. Using a Boolean data type reduces memory requirements.

Table 8.2 Position Controller Signals

Name	Direction	Data Type	Description
XREF	In	Double	Reference displacement
XMEAS	In	Double	Measured displacement
IREF	Out	Double	Commanded coil current

Table 8.3 Voltage to Current, V to I, Signals

Name	Direction	Data Type	Description
VIOUT	In	Double	The Pololu High-Power Motor Driver 36v20 CS board includes a current sensor IC, the Allegro Microsystems ACS714LLCTR-30A-T. VIOUT (digital) is the ADC digital output of the current sensor analog output voltage, VIOUT.
XMEAS	Out	Double	IMEAS = (VIOUT – 2.5V)/(66 mV/A) = (VIOUT – 2.5V)*(15 A/V)

Table 8.4 Voltage to Distance, VOUT to XMEAS, Signals

Name	Direction	Data Type	Description
VOUT	In	Double	VOUT (digital) is the ADC digital output of the Kaman KD-2306-9U non-contact Eddy current displacement sensor output voltage.
XMEAS	Out	Double	XMEAS = (VOUT)*(0.3 mm / 1 V)

Table 8.5 Speedgoat PWM Code Module Signals

Name	Direction	Data Type	Description
PWM A DC	In	Double	Reference PWM duty cycle between 0 (0% duty cycle) and 1 (100% duty cycle).
PWM B DC	In	Double	Reference current polarity or direction (DIR). PWM B DC = '1' means reference current polarity or direction is from OUTA to OUTB. DIR = '0' means reference current polarity or direction is from OUT B to OUT A.
Period	In	Double	The PWM period value in seconds. This port is only active when **Show Period Input Port** is checked.
Halt PWM	In	Double	PWM generation is halted at the next model step after this port is set to 1. This port is only active when **Show PWM Generation Halt Input Port** is checked.
PWMH	Out	5V TTL	Pulse width modulation output; intended for the Pololu 36v20 CS PWMH input. During the active (high) portion of PWMH, the Pololu 36v20 CS outputs put the full V+ voltage across the coil in the direction determined by DIR; during the low portion of PWMH, the Pololu 36v20 CS shorts both coil terminals to ground.
DIR	Out	5V TTL	Direction output; intended for the Pololu 36v20 CS DIR input. When DIR = '1' the polarity or direction is from OUTA to OUTB. When DIR = '0' the polarity or direction is from OUT B to OUT A.

Table 8.6 Pololu High-Power Motor Driver 36v20 CS Signals

Name	Direction	Data Type	Description
PWMH	In	5V TTL	Pulse width modulation input. During the active (high) portion of PWMH, the Pololu 36v20 CS outputs put the full V+ voltage across OUTA and OUTB in the polarity determined by DIR; during the low portion of PWMH, the Pololu 36v20 CS shorts both OUTA and OUTB to ground.
DIR	In	5V TTL	Direction input. When DIR = '1' the current polarity or direction is from OUTA to OUTB. When DIR = '0' the current polarity or direction is from OUTB to OUTA.
OUTA	Out	High Power	High-power output pin; OUTA and OUTB are intended to be connected across a coil.
OUTB	Out	High Power	High-power output pin; OUTA and OUTB are intended to be connected across a coil.
VIOUT	Out	Analog	Current sensor analog output voltage signal. 66 mV/A output sensitivity. At zero current, VIOUT = VCC/2 where VCC = +5Vdc (nominal). VIOUT = (IP)*(66 mV/A) + (VCC/2) = (IP)/(15 A/V) + (2.5V) where IP is the current from OUTA to OUTB
V+	Supply	High Power	DC bus positive terminal.
GND	Supply	High Power	DC bus negative terminal; also signal ground.

Table 8.7 Kaman KD-2306-9U Non-Contact Eddy Current Displacement Sensor Signals

Name	Direction	Data Type	Description
+Vin	In	Power	Input power supply voltage, +15 Vdc.
Ground	In	Power	Input power supply ground.
VOUT	Out	Analog	Displacement sensor analog output voltage signal. The 0 to 10 V output voltage is linearly proportional to the distance between the face of the displacement sensor and the

Name	Direction	Data Type	Description
			stainless-steel conductive target on the flotor assembly. VOUT = (displacement [mm])*(3.33 V/mm) = (displacement [mm])/(0.3 mm/V)
Ground	Out	Analog	Displacement sensor analog output voltage signal ground.

Table 8.8 Speedgoat Analog Input Code Module Signals (1 of 2)

Name	Direction	Data Type	Description
VIOUT	In	Analog	The Pololu High-Power Motor Driver 36v20 CS includes a current sensor IC, the Allegro Microsystems ACS714LLCTR-30A-T. VIOUT is the current sensor analog output voltage signal. VIOUT has 66 mV/A output sensitivity. At zero current, VIOUT = VCC/2 where VCC = +5Vdc (nominal). VIOUT = (IP)*(66 mV/A) + (VCC/2) = (IP)/(15 A/V) + (2.5V) where IP is the current from OUTA to OUTB
VIOUT	Out	Double	The ADC digital output of the current sensor analog output voltage signal, VIOUT.

Table 8.9 Speedgoat Analog Input Code Module Signals (2 of 2)

Name	Direction	Data Type	Description
VOUT	In	Analog	Displacement sensor analog output voltage signal. The 0 to 10 V output voltage is linearly proportional to the distance between the face of the displacement sensor and the stainless-steel conductive target on the flotor assembly.

Name	Direction	Data Type	Description
			VOUT = (displacement [mm])*(3.33 V/mm) = (displacement [mm])/(0.3 mm/V)
VOUT	Out	Double	The ADC digital output of the displacement sensor analog output voltage signal, VOUT.

8.2. Implementation

The Simulink Real-Time hardware-in-the-loop testing with physical sensors and actuators, enabling verification of modeling assumptions and limitations, was implemented.

The position and current controllers consist of a proportional-integral (PI) feedback control loop. The Discrete PID Controller Simulink block is used to implement discrete-time PI control. The Discrete PID Controller Simulink block includes features such as anti-windup, external reset, and output saturation. The PI gains may be automatically tuned by using the 'Tune…' button (which requires a Simulink Control Design license).

8.3. Test Results and Observations

The measured current (IMEAS) (digital) signal shown in Figure 8.1 was observed to be noisy.

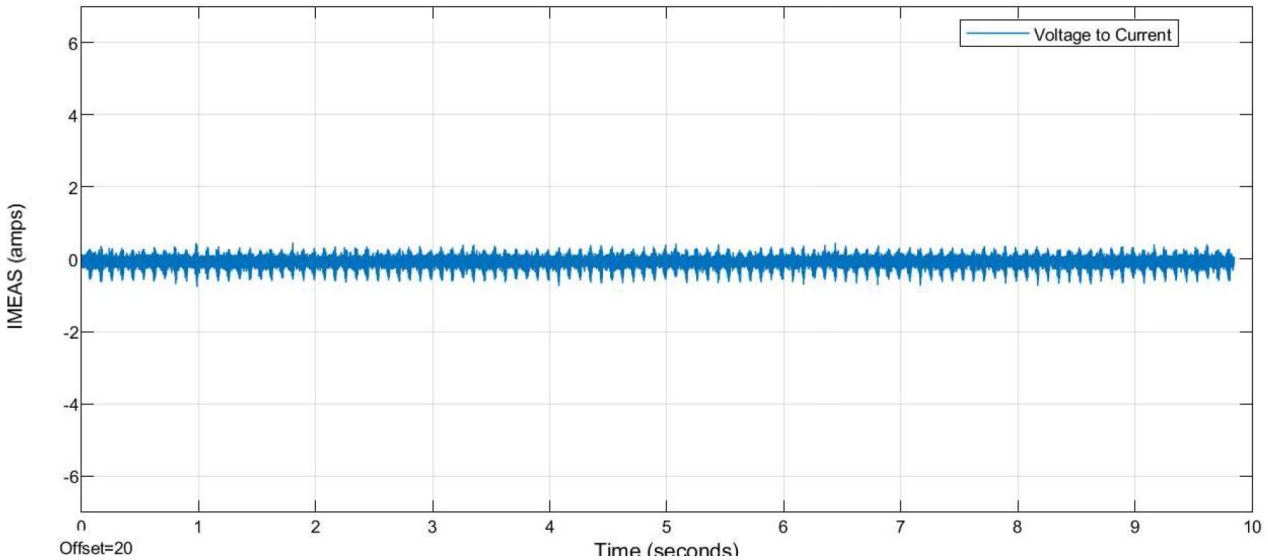

Figure 8.2 IMEAS (Digital) Signal *Before* Reducing the Cut-Off Frequency of the Analog Low-Pass-Filter

Three actions were taken to mitigate the observed sensor noise:

1) the current sensor integrated circuit's (IC) supply voltage implementation was changed from a +5Vdc wall-wart to a +5Vdc linear voltage regulator,
2) the dc bus voltage was filtered, and
3) the analog bandwidth of the current sensor was reduced, i.e., the cut-off frequency of the analog low-pass-filter was reduced.

The first two actions had no appreciable effect on the current sensor noise. The third action reduced the observed measurement noise, at the expense of the current sensor's step response (Figure 8.3). This reduction in step response caused by low-pass filtering the analog signal was less than the reduction in step response caused by low-pass filtering the digital signal (i.e., after the Speedgoat Analog Input Code Module).

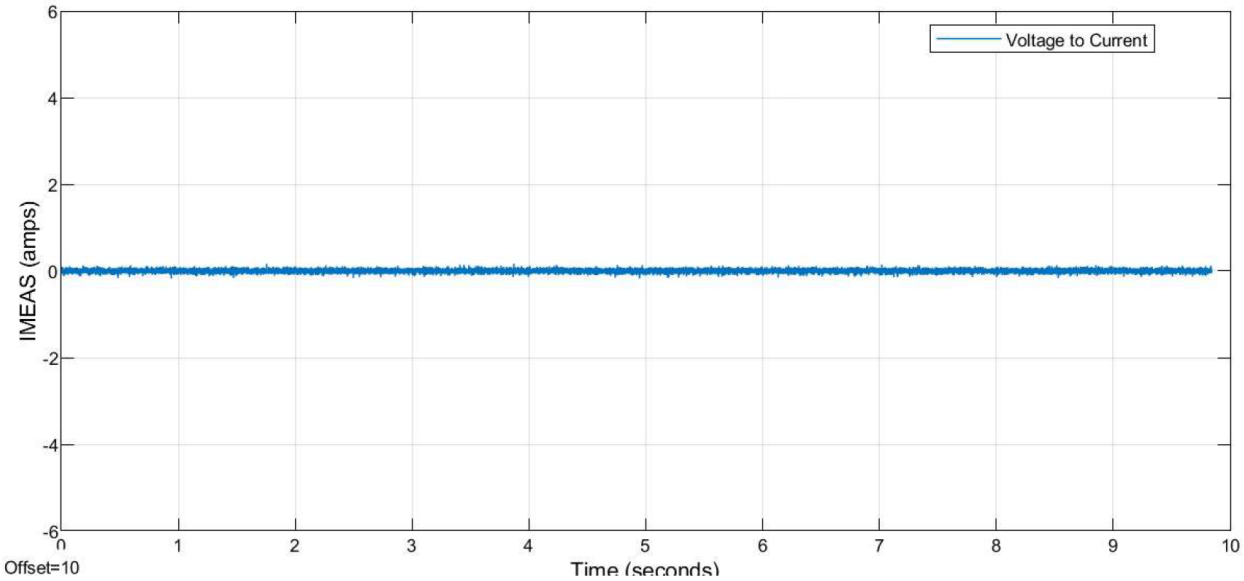

Figure 8.3 IMEAS (Digital) Signal *After* Reducing the Cut-Off Frequency of the Analog Low-Pass-Filter

The measured displacement (XMEAS) (digital) signal, i.e., the position sensor signal was not noisy. A PI controller was implemented but not tuned for the current controller. Current control was achieved. The ability to "snap" the flotor to the zero gap position was demonstrated. The ability to accurately maintain a non-zero gap was not achieved, yet. Controller development is ongoing.

CHAPTER 9. ROTARY ABSOLUTE ENCODER

The Renishaw Resolute™ rotary absolute encoder system is not used in the single-axis active-magnetic-bearing (AMB) academic test fixture. However, this rotary encoder system is used in the University of Idaho (UI) flywheel energy storage system (FESS), as shown in Figure 1.3.

This chapter presents the results of this project's development of the rotary encoder system interface. The rotary encoder interface did not work initially. The troubleshooting steps taken to get to the root cause are detailed. After the root cause had been identified and sufficiently addressed, the Renishaw Resolute™ rotary absolute encoder system block diagram, shown in Figure 9.1, was functional on the bench.

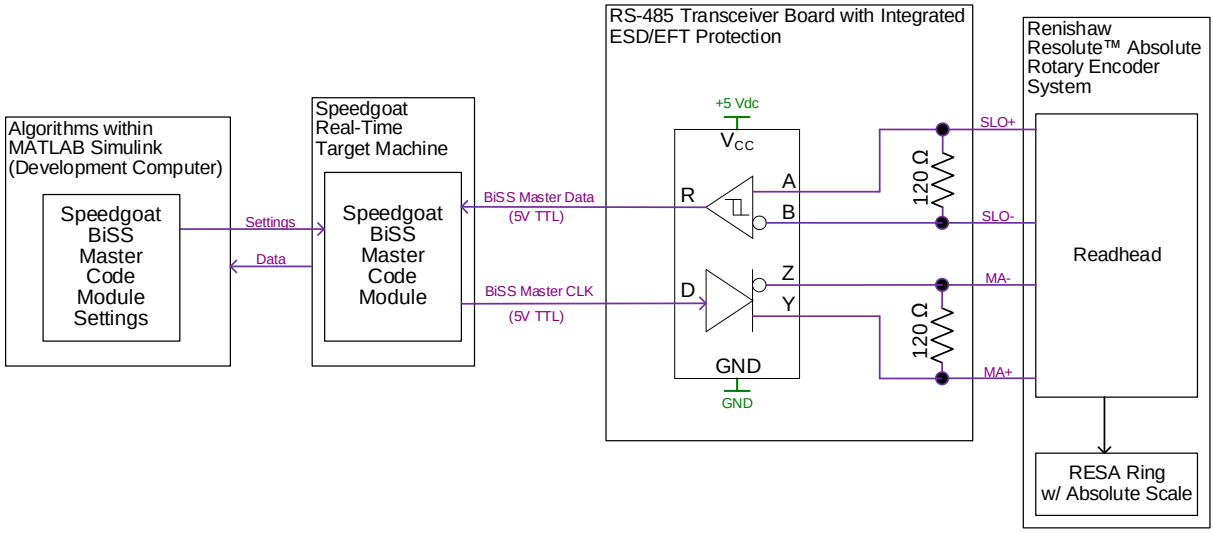

Figure 9.1 Rotary Absolute Encoder System Interface Block Diagram

This rotary absolute encoder interface implements HIL with MATLAB Simulink real-time models. A Speedgoat performance real-time target machine connects a development computer running MATLAB Simulink with hardware consisting of one Renishaw Resolute™ rotary absolute encoder system. It allows the angular position to be measured by a rotary absolute encoder.

This rotary absolute encoder system interface allows for prototyping of UI FESS subsystems in MATLAB Simulink.

9.1. Overview of Operation

The Renishaw Resolute™ rotary absolute encoder system is a rotational position measurement system consisting of a miniature ultra-high-speed digital camera inside a stationary readhead and a stainless-steel ring with absolute scale code marked directly on the periphery.

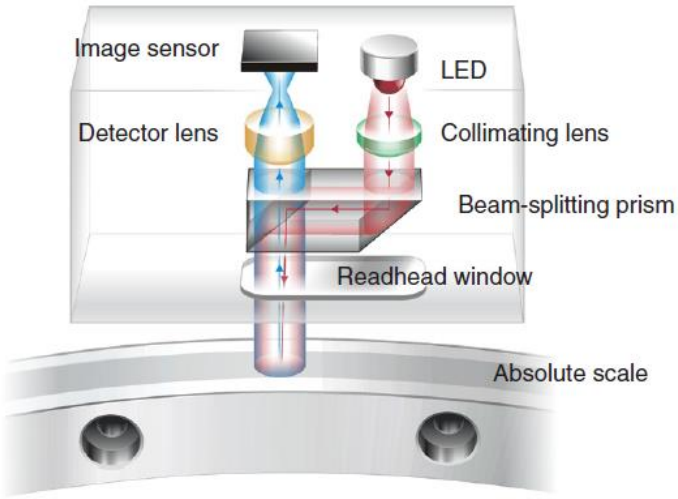

The Resolute encoder calculates rotational position on demand. The readhead receives a series of request signals from the host control system (Speedgoat Performance Real-Time Target Machine). Each time it receives a request, the readhead determines rotational position by two independent methods: 1) decoding a single image without any information from previous positions, and 2) linear extrapolation from the two most recent rotational position readings, assuming constant velocity. Once the two rotational position methods have been calculated, the encoder decides which position to output and whether to set the error flag. If the positions calculated by the two methods agree within ±15 µm (half a scale period) of one another, then the encoder outputs the position from the first method and sets an internal counter to zero.

If the positions disagree, then the encoder outputs the position from the second method and increments the internal counter. If the internal counter ever exceeds four, then the readhead sets the error flag. The readhead makes sure that there is never more than 75 µs between images by capturing extra images between requests if necessary. For a system requesting a position every ≤ 75 µs, the time between outputting the first incorrect position and raising the error flag is five times the request interval. For a slower system requesting a position at 500 µs intervals, this time will be 500 µs, as the readhead will have processed six further images between each pair of requests to make sure that the time between images never exceeds 75 µs. In both cases, the time between outputting an incorrect position and raising the error flag is sufficiently short that appropriate action can be taken in response to the error flag before the incorrect rotational position data can influence the control system.

9.2. RESA Absolute Angle Encoder System Parameters

Table 9.1 Renishaw Resolute™ Absolute Encoder System Parameters

Parameter	Value	Unit	Notes
Power Supply Requirements Voltage Voltage Ripple Maximum Current	 5 ±10% ±200 250	 Vdc mVpp mAdc	 at frequency up to 500 kHz maximum
Acceleration (Readhead), Operating	500	m/s^2	3 axes
Acceleration (Readhead), Maximum	2000	m/s^2	
Angular Velocity, Maximum Reading Speed of the RESA30SA206B ring	9200	rev/min	Renishaw recommends operating velocity does not exceed 50% of the rated maximum reading speed of the RESA30 ring
Angular Velocity, Operating	≤ 4600	rev/min	at 4600 rev/min, the rotor assembly will rotate 1.104 degrees
Angular Position, Accuracy	±4.94	arc second	18-bit resolution
Readhead Mass	19	g	UHV Readhead
Cable Mass	19	g/m	UHV Readhead Cable
Timeout Period	40	µs	minimum time between requests
Time Between Images	75	µs	maximum
Request Interval	40	µs	minimum
Request Rate	25	kHz	maximum
Readhead Physical Dimensions	36 x 16.5 x 17.2	mm	Length x Width x Height for UHV Readhead
Scale Pitch	30	µm	nominal
RESA30SA206B Ring Material	303/304		stainless steel
RESA30SA206B Coefficient of thermal expansion	15 ±0.5	µm/m/°C	at 20°C
RESA30SA206B Ring Outer Diameter	206	mm	
Readhead Protocol	BiSS C		
Resolution	18	bit	
Counts Per Revolution	262,144	counts	18-bit resolution
Readhead Electrical Cable Length	5	m	
Readhead Electrical Connection	flying lead		
Readhead Electrical Cable Construction			Silver-coated copper braided single screen. Fluorinated Ethylene propylene (FEP) core insulation, over tin-plated copper wire.
Readhead Electrical Cable Characteristic Impedance (Z_0)	100	Ω	for each differential pair (MA+,MA-) and (SLO+,SLO-)
Readhead Internal/Integrated Termination Resistor	120	Ω	for each differential pair (MA+,MA-) and (SLO+,SLO-)
Operating Temperature Range	0°C to +75°C		
Communication Format – BiSS	RS485/RS422		differential line-driven signal

Note 1: Renishaw Resolute™ Angle Readhead RA18BVA206B50V with RESA30SA206B Rotary (Angle) Ring Parameters shown here are from [28][29][30][31].

Note: Actual readhead part number is RA18BVA206B50V

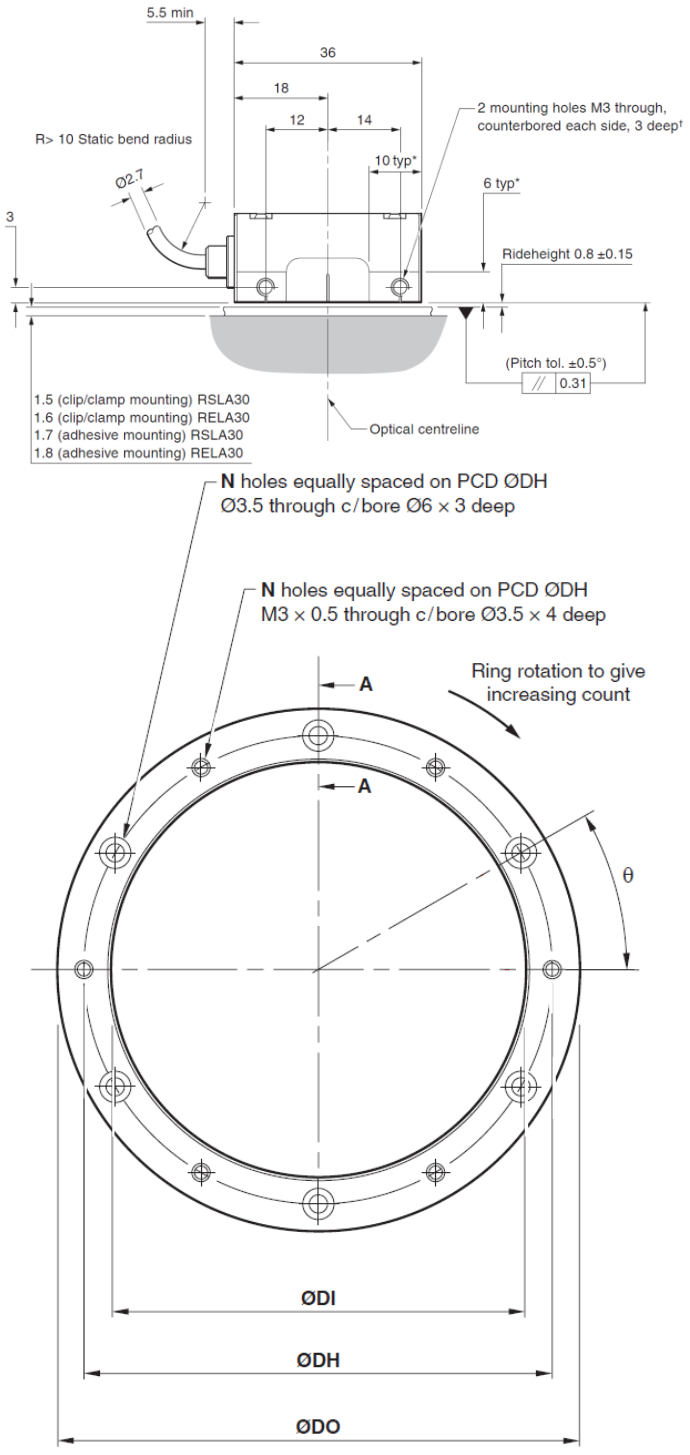

Figure 9.2 Renishaw Resolute™ UHV Absolute Optical Encoder [28] with RESA30 Rotary (Angle) Ring [30]

The Renishaw Resolute™ Ultra High Vacuum (UHV) absolute optical angle encoder readhead (Figure 9.3) is compatible with the RESA30 angle encoder. The readhead is an ultra-fast miniature digital camera that takes photos of the RESA30 ring's coded scale. The photos are analyzed by a high-speed digital signal processor (DSP) to determine absolute position. The built-in position-check algorithm constantly compares the calculated positions from two position measurement methods, 1) decoding a single image without any information from previous positions, and 2) linear extrapolation from the two most recent rotational position readings, assuming constant velocity. The Renishaw Resolute™ UHV readhead outputs position data upon request with the BiSS interface [31]. The Resolute™ UHV readhead is suitable for use in UHV conditions up to 10^{-9} Torr. To aid installation and diagnostics, there is an integral set-up LED on the readhead [33].

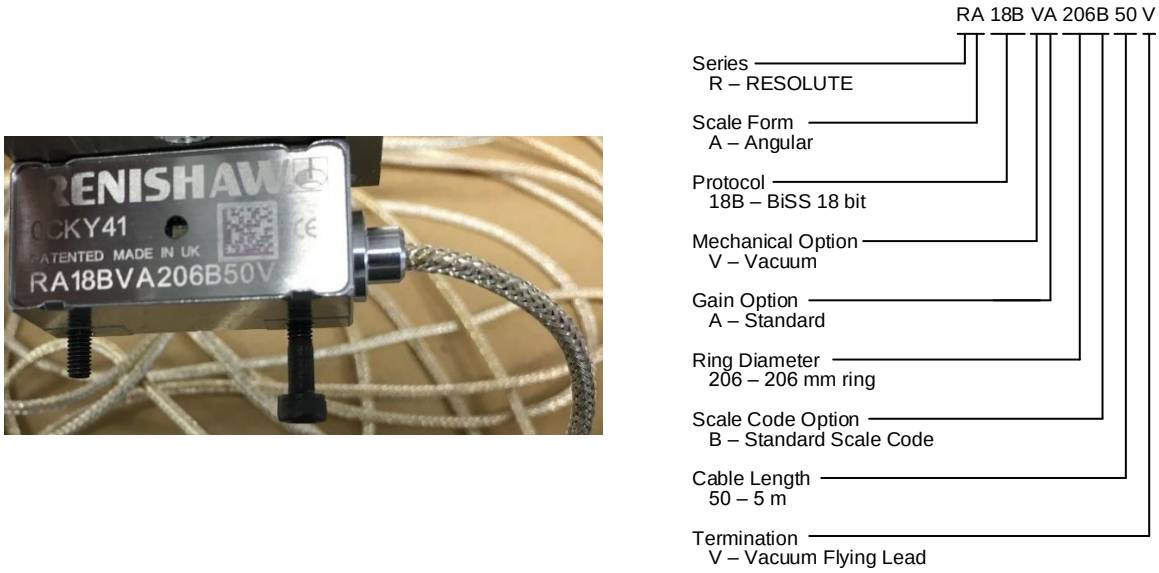

Figure 9.3 RA18BVA206B50V Angle Readhead Part Number

The RESA30 ring (Figure 9.4) is a one-piece stainless-steel ring with absolute scale code marked directly on the periphery. The non-contact format eliminates backlash, shaft wind-up (torsion), and other mechanical hysteresis errors.

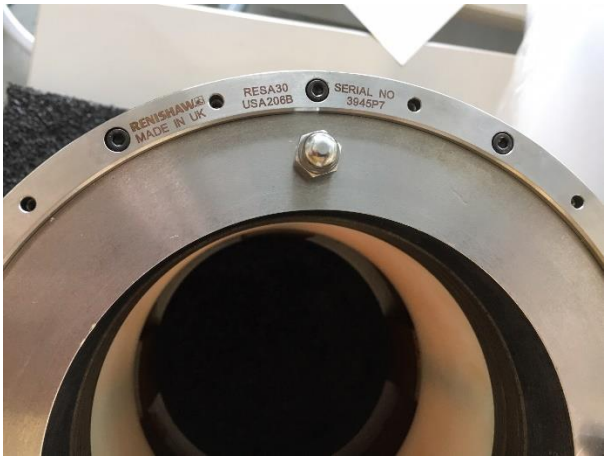

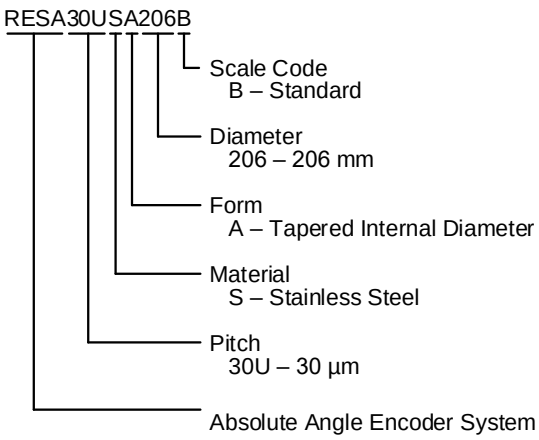

Figure 9.4 RESA30SA206B Rotary (Angle) Ring Part Number

9.3. Hardware Interface & Electrical Connections

The Renishaw Resolute™ absolute rotary encoder system readhead has an integrated 5-meter shielded cable with unterminated flying leads. The cable construction consists of a silver-coated copper braid single screen (shield) around a fluorinated ethylene propylene (FEP) core insulation surrounding seven tin-plated copper wires with functionality as shown in Table 9.2 and Figure 9.5.

Table 9.2 Renishaw Resolute™ UHV Cable Flying Leads [33]

Function	Signal	Wire Color
Power	+5V	Brown
	0V	White
		Green
Serial Communications	MA+	Violet
	MA-	Yellow
	SLO+	Gray
	SLO-	Pink
Shield	Shield	Silver-Coated Copper Braid

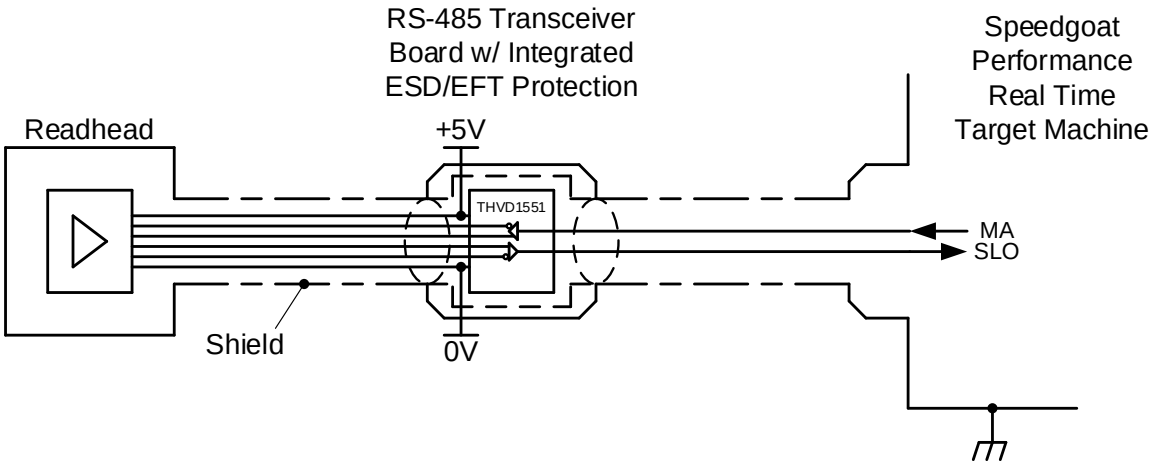

Figure 9.5 Renishaw Resolute™ Absolute Encoder System [33] Electrical Connections

The Texas Instruments THVD1551DGKR [34] device is a 5V RS-485 transceiver with ±18-kV IEC ESD protection. The THVD1551 is fully enabled with no external enabling pins.

9.4. BiSS Serial Communications

BiSS is an open-source serial communication protocol. BiSS stands for bidirectional serial synchronous. The Renishaw Resolute™ absolute encoder system supports the *BiSS C* mode (continuous mode) protocol in a unidirectional interface. BiSS is a high-speed serial protocol. The open source BiSS protocol implements a real-time interface between the Renishaw Resolute™ absolute encoder and the Speedgoat, Inc. Performance Real-Time Target Machine. It is a master-slave interface.

The Speedgoat, Inc. Performance Real-Time Target Machine is the master, and the Renishaw Resolute™ absolute encoder is the slave. The master controls the timing of position acquisition and the data transmission speed. The physical layer of this interface consists of two unidirectional differential pairs of lines:

- "MA" transmits position acquisition requests and timing information (clock) from master to encoder.
- "SLO" transfers position data from encoder to master, synchronized to MA.

Figure 9.6 shows the data transmitted.

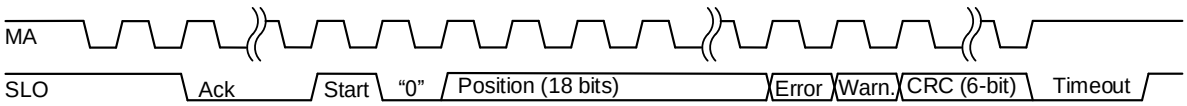

Figure 9.6 Renishaw Resolute™ Encoder BiSS C-mode (Unidirectional) Protocol Data Format

When the BiSS C-mode (unidirectional) interface bus is idle, the master holds MA high. The encoder indicates it is ready by holding SLO high. The master requests a position acquisition by starting to transmit clock pulses on MA. On the second rising edge from MA, the encoder sets SLO to “0,” generating the acknowledge (“Ack”). SLO remains low while the encoder takes an image with its high-speed camera and calculates the angular position with 18-bit resolution. After the angular position acquisition is complete, the encoder transmits data to the master synchronized to MA starting with one “Start” bit (SLO = “1”) and one “0” bit. The absolute position data are in binary format and transmitted most-significant bit (MSB) first synchronously with the clock MA. The error bit is active low and indicates that the position data should not be trusted. The error bit is also set to “0” if the temperature exceeds the maximum specified for the Renishaw Resolute™ encoder system. The warning bit is active low and indicates that the encoder scale and/or readhead lens should be cleaned, but it is not an indication of trustworthiness of the position data. The cyclic redundancy check (CRC) polynomial for position, error, and warning data is $x^6 + x^1 + x^0$. It is transmitted MSB first and inverted. The start bit and “0” bit are omitted from the CRC calculation. When all the data have been transferred, the master stops the clock and sets MA high. If the encoder is not yet ready for the next request cycle, then it sets SLO low (the Timeout period). When the encoder is ready for the next request cycle, it indicates this to the master by setting SLO high.

Table 9.3 Timing Parameters [31]

Parameter	Min	Typ	Max	Units	Notes
Ack time			20	µs	Note that Ack period always ends on an MA clock rising edge. Therefore, at low MA clock frequencies, the Ack time may exceed 20 µs.
MA Clock Frequency	0.28	2	2	MHz	MA clock frequency must be constant
MA Clock Duty Cycle		50		%	MA clock duty cycle should be 50%
Request Cycle Rate		TBD	25	kHz	
Sampling Moment	3.975	4.000	4.025	µs	Timed from the first rising edge on MA clock
RESOLUTE Internal Line Delay			42.5	ns	Internal propagation delay (MA-SLO) within Renishaw Resolute™ encoders
Line Delay Due to Cable Length		10		ns/m	Round-trip delay through cable (i.e., from master to encoder and back to master again)

The minimum empirically observed MA clock frequency is 280 kHz (0.28 MHz). With an MA clock frequency of 2 MHz, each bit transmitted on SLO takes 0.5 µs. The maximum acknowledge time is 20 µs, and there are a total of 28 bits to be transmitted during each request cycle. This leaves 40 µs – 20 µs – (28 bits)*(0.5 µs/bit) = 6 µs of slack in the timing while the maximum 25 kHz request cycle rate is achieved.

Signals travelling between master and encoder experience a time delay because of the cable length and signal propagation delays within the master and encoder. With an MA clock frequency of 2 MHz, the maximum cable length is 8 m [31]. The actual cable length is 5 m. Renishaw also recommends that the cable length be limited to 5 m to minimize the 5V supply voltage drop.

The encoder calculates a six-bit cyclic redundancy check (CRC) value from the data. The CRC polynomial for the 18-bit position, one-bit error, and one-bit warning data is $x^6 + x^1 + x^0$. The CRC method treats the 20 data bits as a single binary word and divides it by a key word, k, that is known to both the transmitter (encoder) and receiver (master) using polynomial division. The encoder uses the key k = 67. This number written in binary is 1000011, and expressed as a polynomial it is $x^6 + x^1 + x^0$. The polynomial has seven bits. The remainder of any digital word divided by a seven-bit word using polynomial division will contain no more than six bits, so the CRC words based on the CRC key 1000011 will always fit into the six CRC bits in the transmitted encoder data format. This is called a “six-bit CRC.” The six-bit CRC is calculated by dividing the 20 data bits by 1000011 using polynomial division. The remainder is the six-bit CRC check value. The receiver (master) calculates the six-bit CRC of the 20 data bits using the same CRC polynomial and compares the calculated result with the received six-bit CRC check

value. If the CRC check values do not match, then the 20 data bits contain a data error. If the CRC check values match, then the data are assumed to be error-free.

The receiver (master) is the Speedgoat, Inc. Performance Real-Time Target Machine. The development PC will run MATLAB Simulink. MATLAB code in a programmable Simulink block can be used to generate a six-bit CRC check value. The Communications Toolbox supports CRC Coding using Simulink blocks.

9.5. Renishaw Resolute™ Absolute Rotary Encoder DB9 Signals Oscilloscope Captures

This section contains oscilloscope captures at the Renishaw Resolute absolute rotary encoder DB9 connector pins while it is connected to the E201-9S USB Interface [35].

The Renishaw Resolute absolute rotary encoder DB9 connector is then moved from the E201-9S USB Interface [35] to a Texas Instruments THVD1551DGKR [34] to transform the differential clock (MA+ and MA-) and data (SLO+ and SLO-) signals from the encoder to the single ended clock (CLK) and data signals on the Speedgoat. A second set of oscilloscope captures are taken at the Renishaw Resolute absolute rotary encoder DB9 connector pins while it is connected to the Texas Instruments THVD1551DGKR [34] and the Speedgoat.

9.5.1. Renishaw Resolute Absolute Rotary Encoder DB9 Connector Pins While Connected to the E201-9S USB Interface (known good /working)

All oscilloscope captures are taken single-ended with respect to the DB9 connector pin 9 (0V).

MA+ frequency: 281.69 kHz

MA+ period: 3.55 µs

MA+ frame duration: ~224 µs (~64 MA+ rising edges)

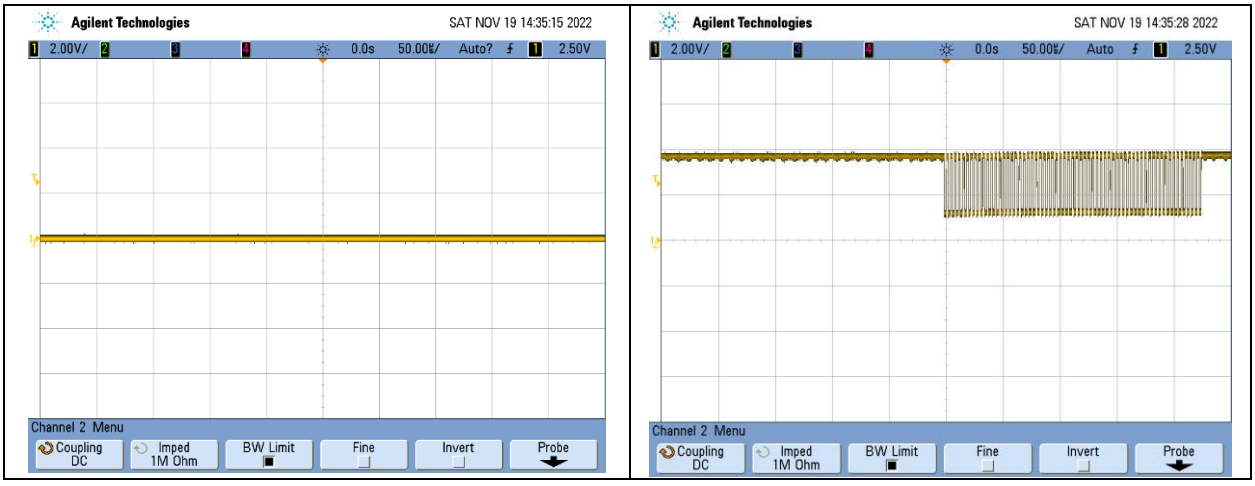

DB9 Connector Pin 1 (Inner Shield).
Shows pin 1 is 0 V (clean).

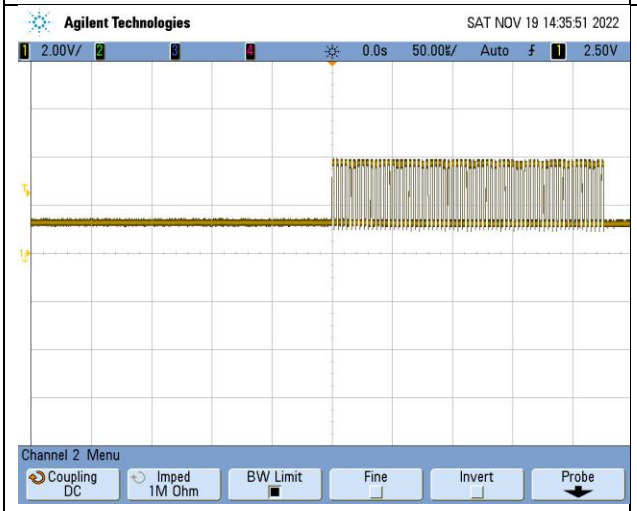

DB9 Connector Pin 2 (MA+).
Shows MA+ Vhigh ≈ 3.75 V, Vlow ≈ 1.25 V.
Idle state is high, 64 MA+ rising edges.

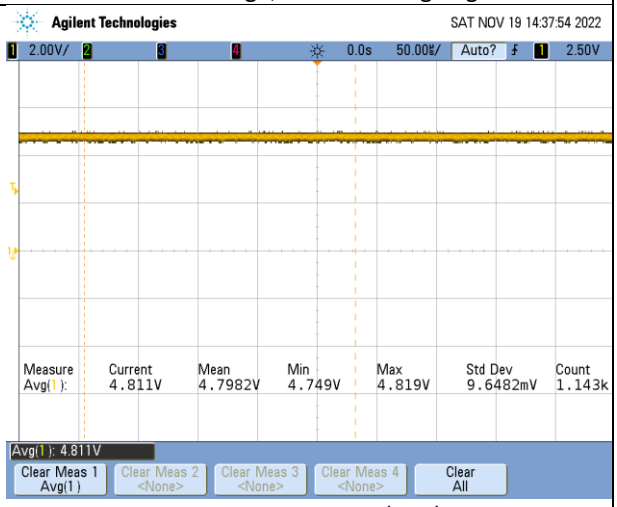

DB9 Connector Pin 3 (MA-).
Shows MA- is complement of MA+, as expected.

DB9 Connector Pin 4 (+5V).
Shows +5V supply is 4.8 Vdc and clean.

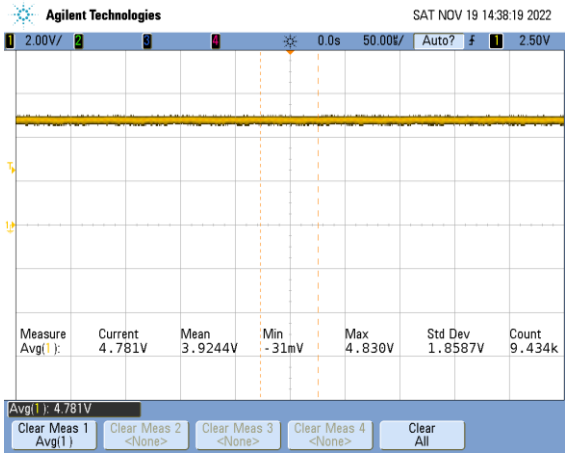

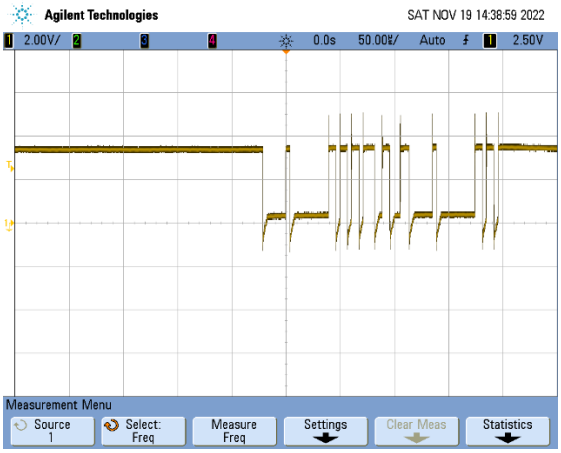

DB9 Connector Pin 5 (+5V).
Shows +5V supply is on both pins 4 and 5.
Shows +5V supply is 4.8 Vdc and clean.

DB9 Connector Pin 6 (SLO+)
Shows SLO+ Vhigh ≈ 3.5 V, Vlow ≈ 0.35 V.
Idle state is high, responds to MA+ rising edges.

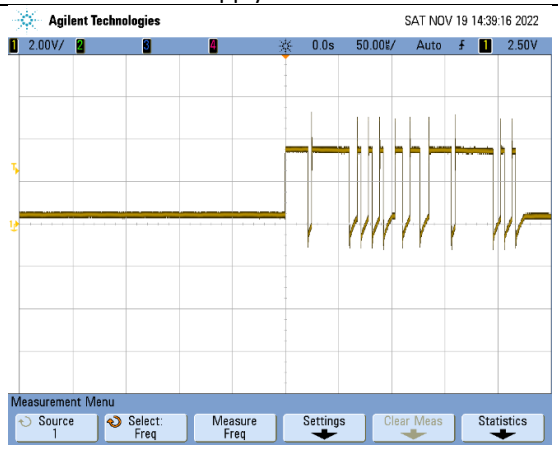

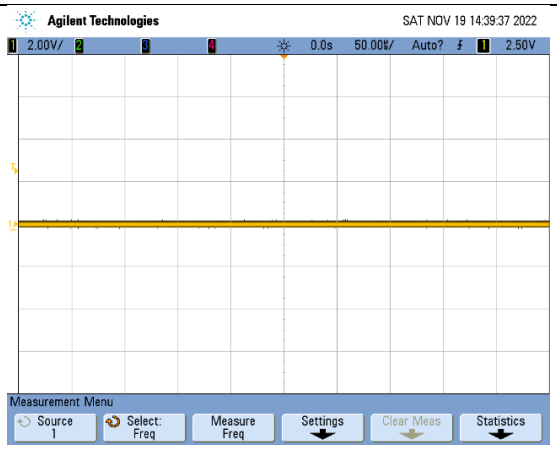

DB9 Connector Pin 7 (SLO-).
Shows SLO- is complement of SLO+, as expected.

DB9 Connector Pin 8 (0V).
Shows pin 8 is 0 V (clean).

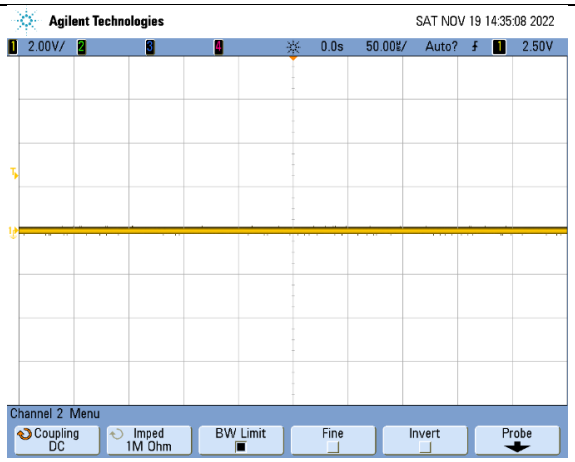

DB9 Connector Pin 9 (0V).
Shows pin 9 is 0 V (clean).

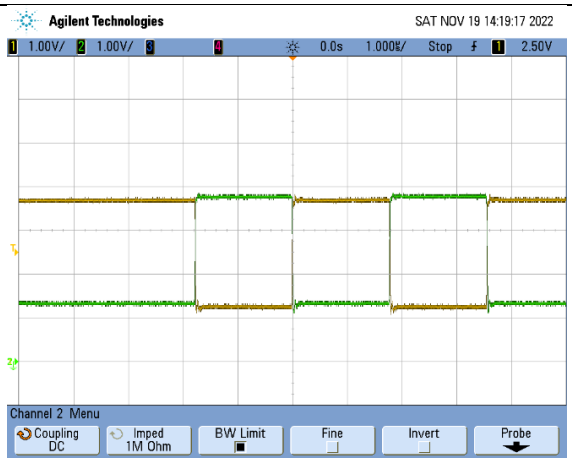

MA+ and MA- on same oscilloscope capture.
Vhigh ≈ 3.75 V, Vlow ≈ 1.25 V

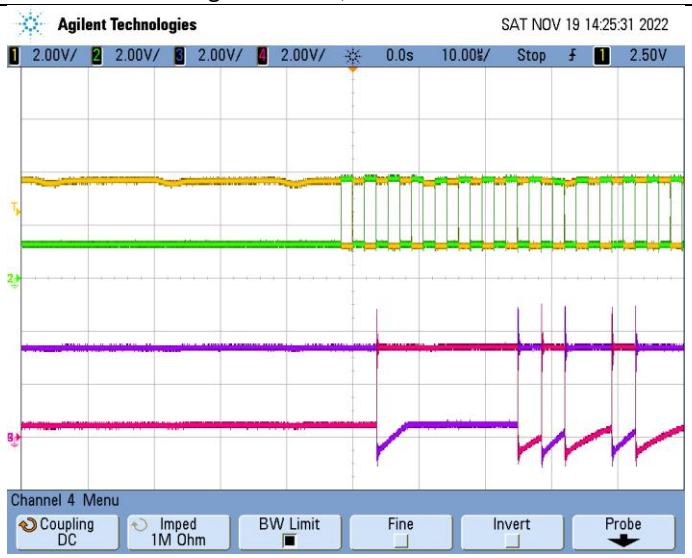

MA+, MA- (top) and SLO+, SLO- (bottom) on same oscilloscope capture.

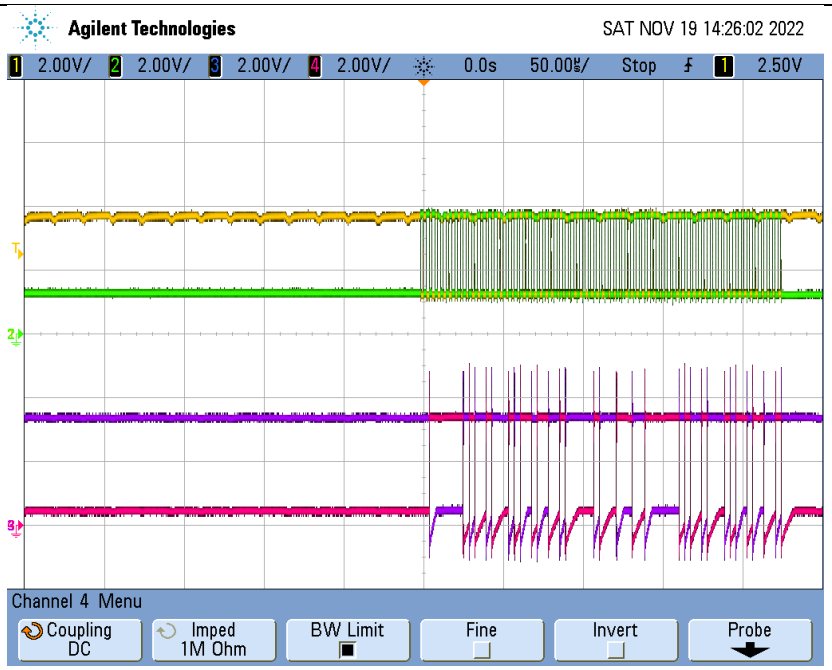

MA+, MA- (top) and SLO+, SLO- (bottom) on same oscilloscope capture.

9.5.2. *Renishaw Resolute Absolute Rotary Encoder DB9 Connector Pins While Connected to Texas Instruments THVD1551DGKR and the Speedgoat*

All oscilloscope captures are taken single-ended with respect to the DB9 connector pin 9 (0V).

MA+ frequency: 280.11 kHz

MA+ period: 3.57 µs

MA+ frame duration: ~125.3 µs (~35 MA+ rising edges)

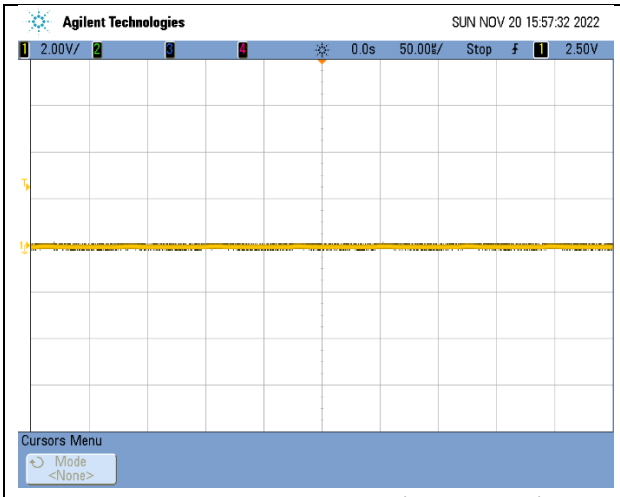

DB9 Connector Pin 1 (Inner Shield).
Shows pin 1 is 0 V (clean).

DB9 Connector Pin 2 (MA+).
Shows MA+ Vhigh ≈ 3.60 V, Vlow ≈ 1.03 V.
Idle state is high, ~35 MA+ rising edges.

DB9 Connector Pin 3 (MA-).
Shows MA- is complement of MA+, as expected.

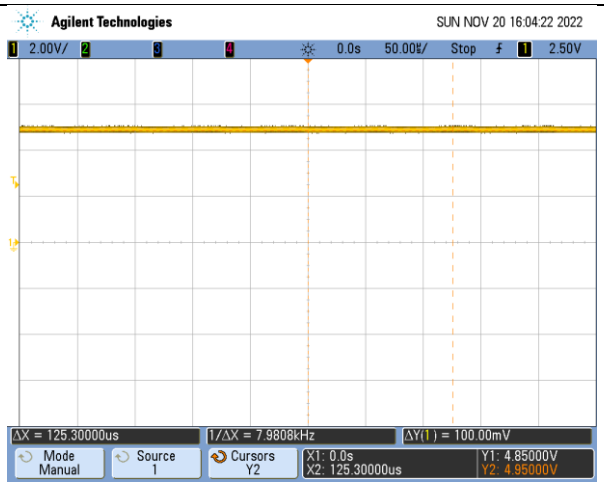

DB9 Connector Pin 4 (+5V).
Shows +5V supply is on both pins 4 and 5.
Shows +5V supply is 4.9 Vdc and clean.

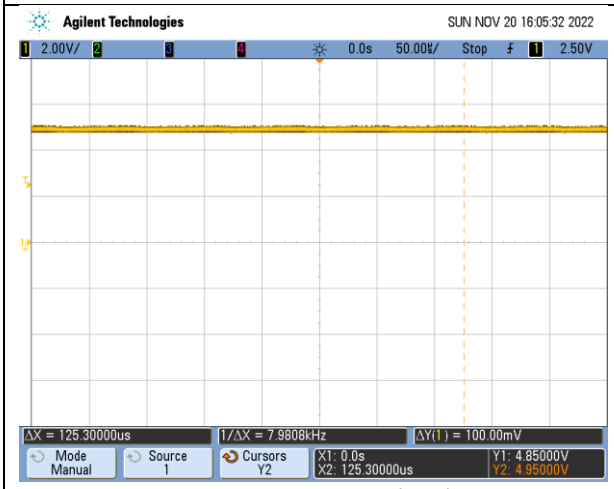

DB9 Connector Pin 5 (+5V).
Shows +5V supply is on both pins 4 and 5.
Shows +5V supply is 4.9 Vdc and clean.

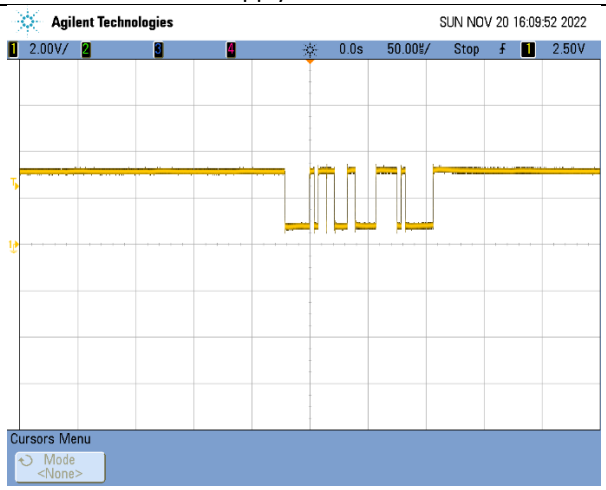

DB9 Connector Pin 6 (SLO+).
Shows SLO+ Vhigh ≈ 3.2 V, Vlow ≈ 0.8 V.
Idle state is high.

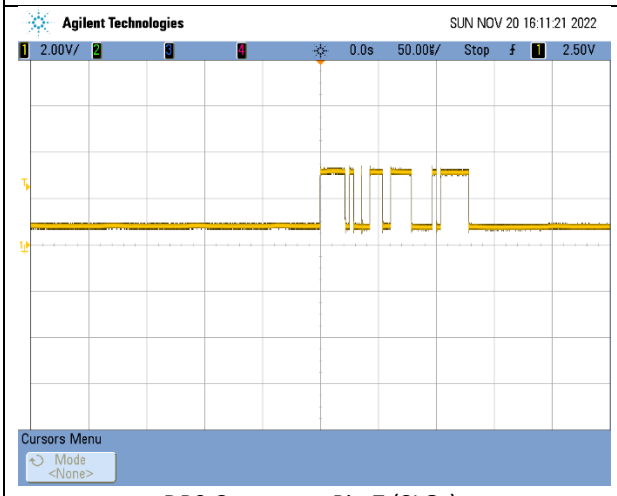

DB9 Connector Pin 7 (SLO-).
Shows SLO- is complement of SLO+, as expected.

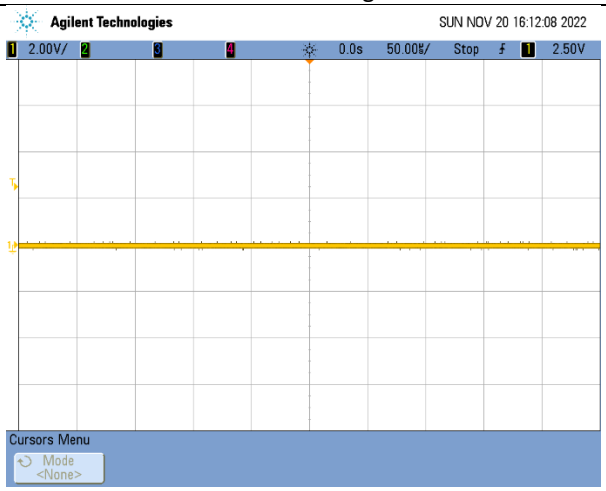

DB9 Connector Pin 8 (0V).
Shows pin 8 is 0 V (clean).

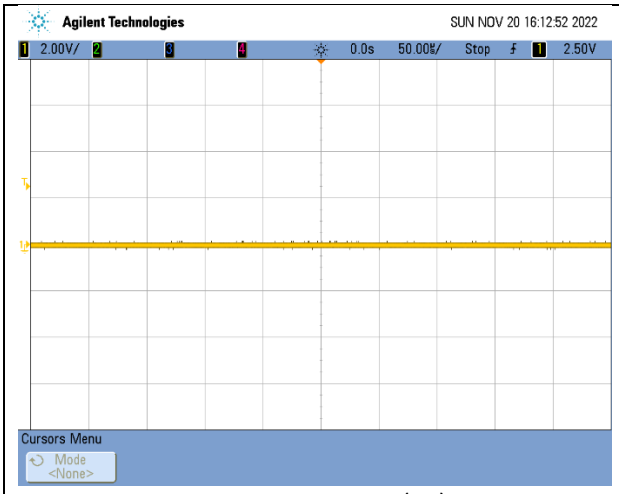

DB9 Connector Pin 9 (0V).
Shows pin 9 is 0 V (clean).

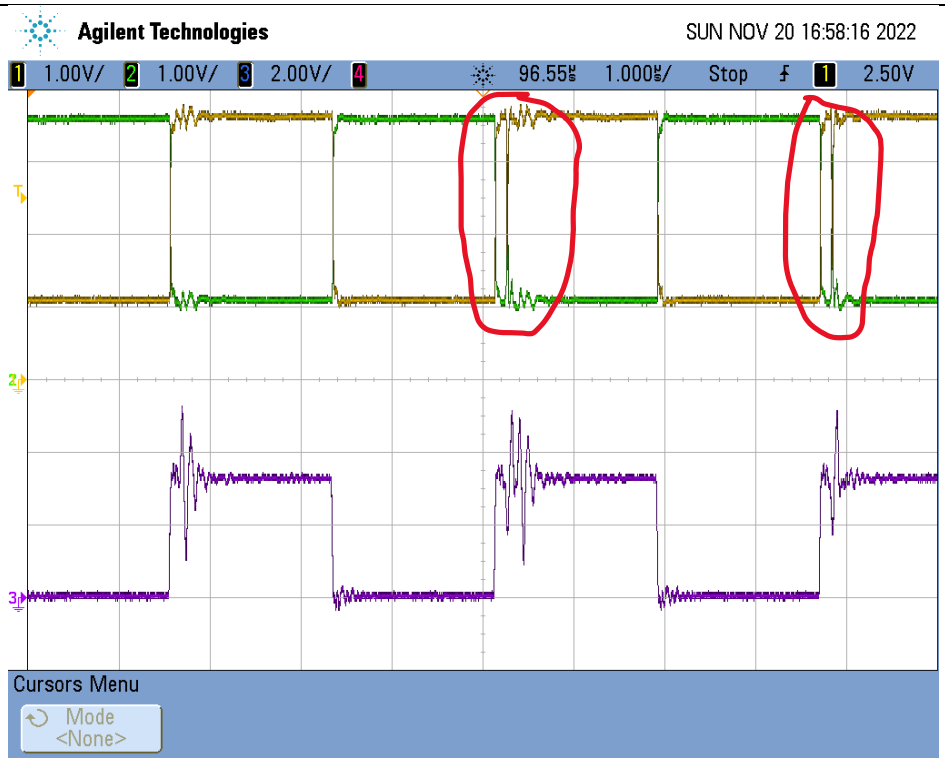

Zooming in on the MA+ and MA- (top) and Speedgoat (bottom) (1 µs per division).
MA+, MA- (top) and the single ended Clock (CLK) on the Speedgoat (bottom) on same oscilloscope capture.
Note glitches in MA+ / MA-.
Note glitch in the single ended Clock (CLK) on the Speedgoat when connected to the Texas Instruments THVD1551DGKR.

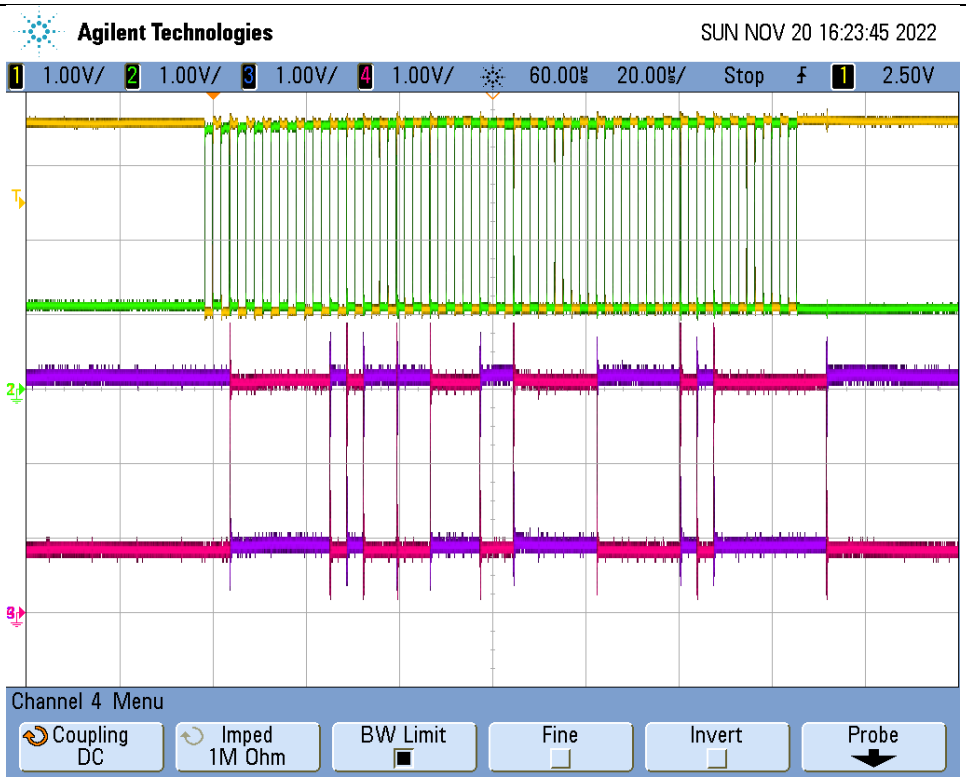

MA+, MA- (top) and SLO+, SLO- (bottom) on same oscilloscope capture.

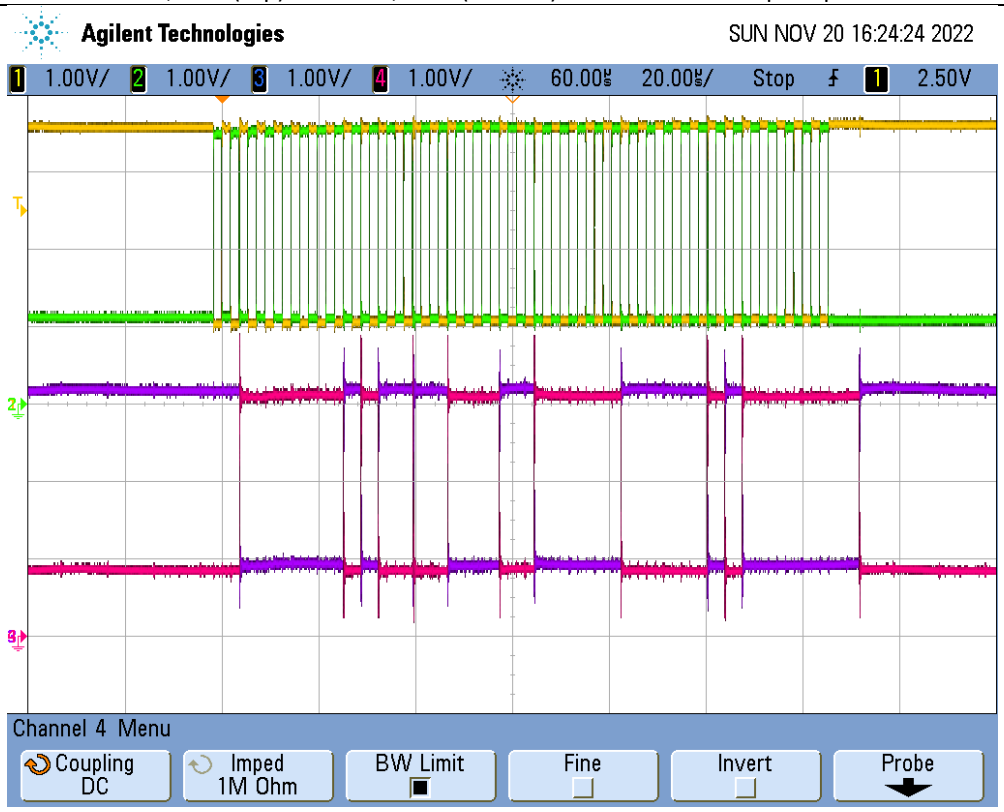

MA+, MA- (top) and SLO+, SLO- (bottom) on same oscilloscope capture.

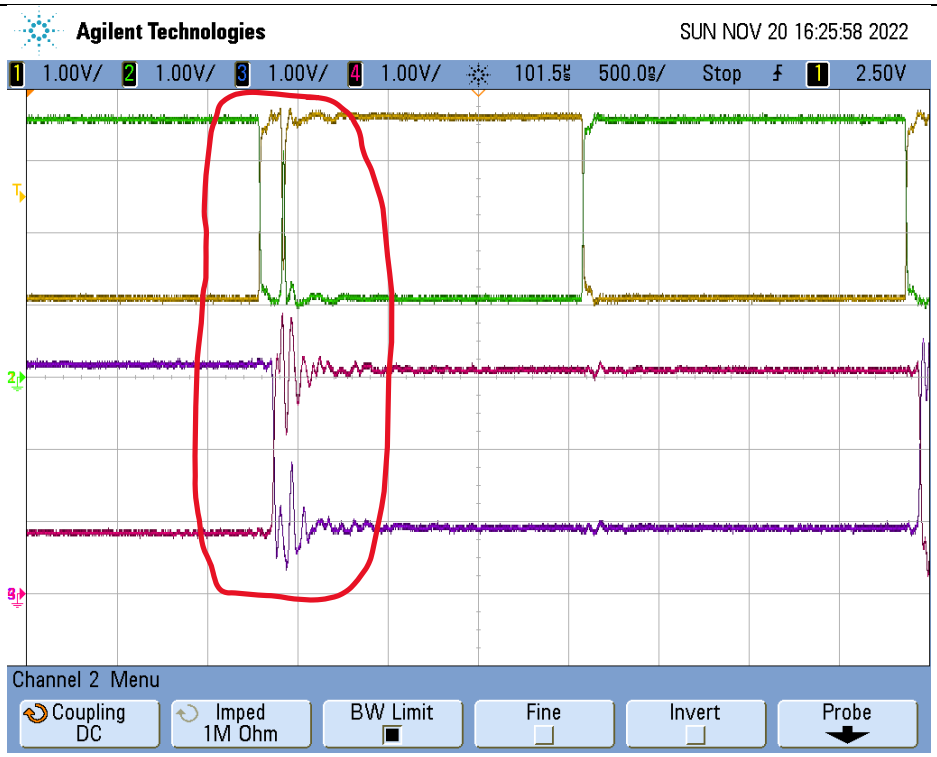

Zoomed MA+, MA- (top) and SLO+, SLO- (bottom) on same oscilloscope capture. Note glitch.

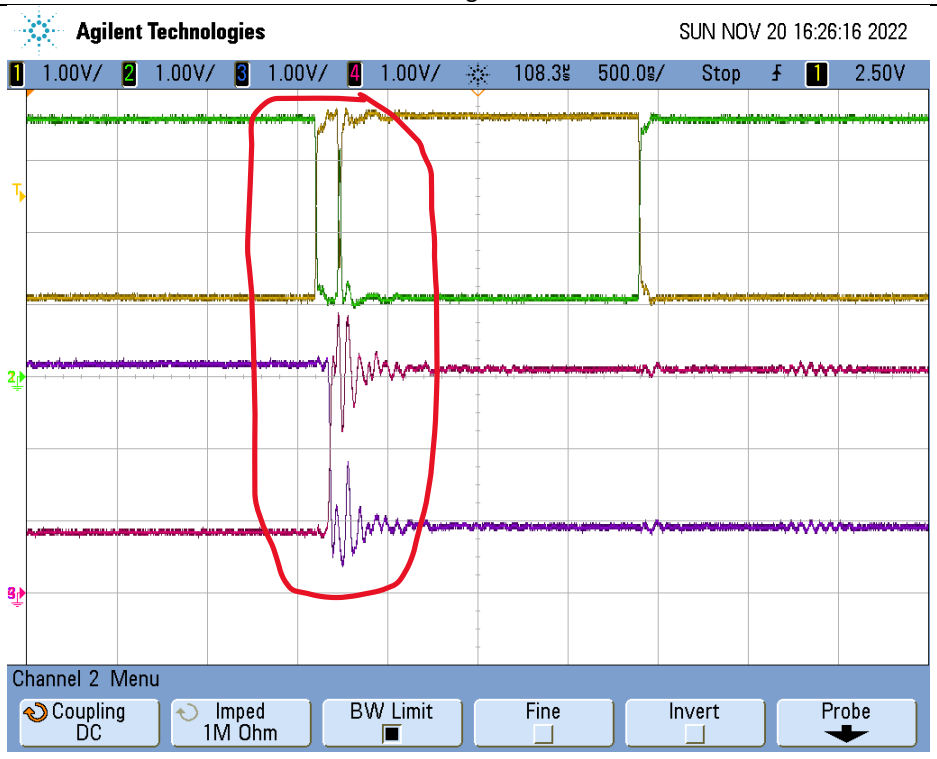

Zoomed MA+, MA- (top) and SLO+, SLO- (bottom) on same oscilloscope capture. Note glitch.

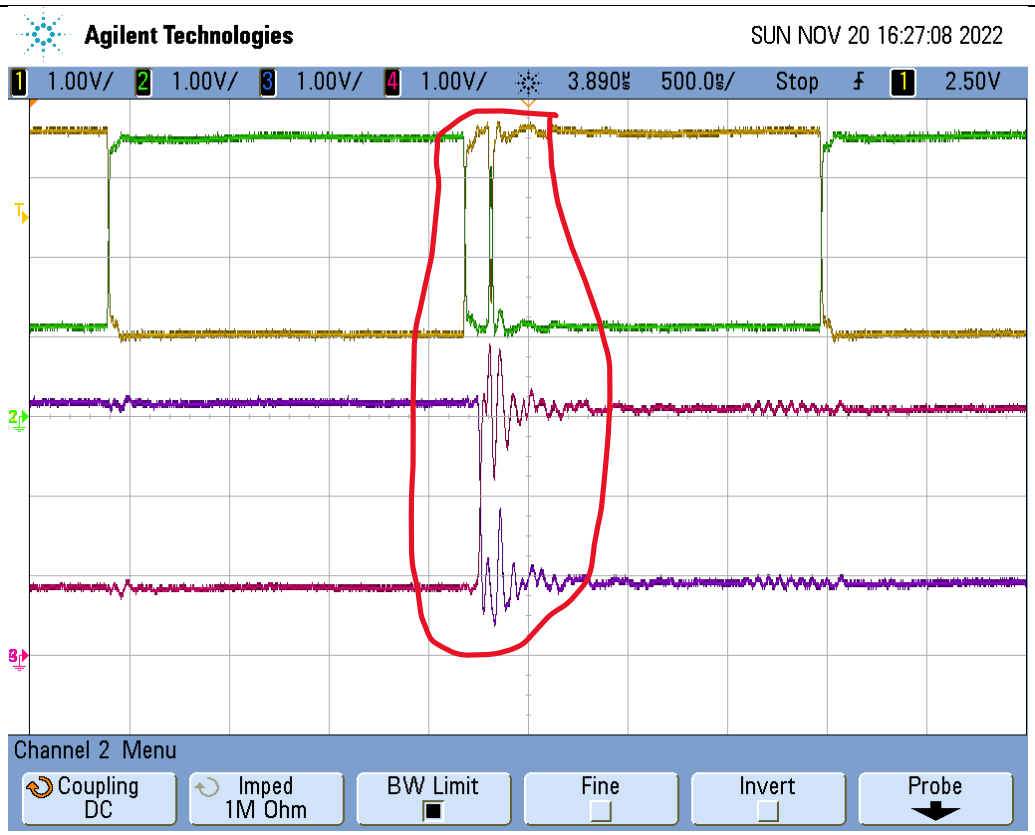

Zoomed MA+, MA- (top) and SLO+, SLO- (bottom) on same oscilloscope capture. Note glitch.

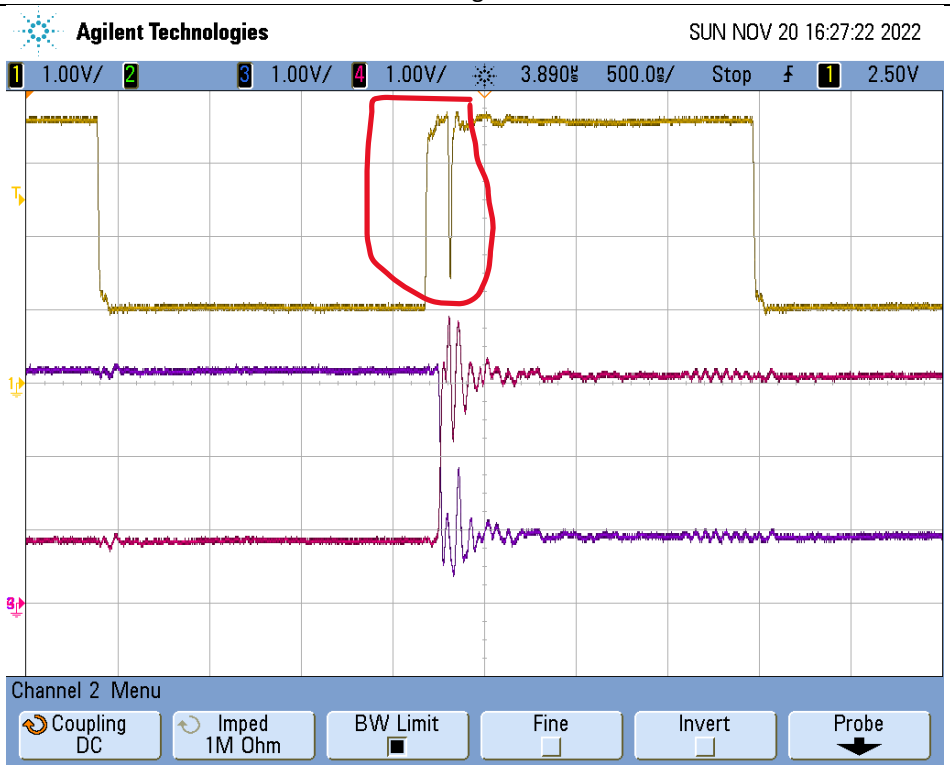

Zoomed MA+ only (top) and SLO+, SLO- (bottom) on same oscilloscope capture. Note glitch.

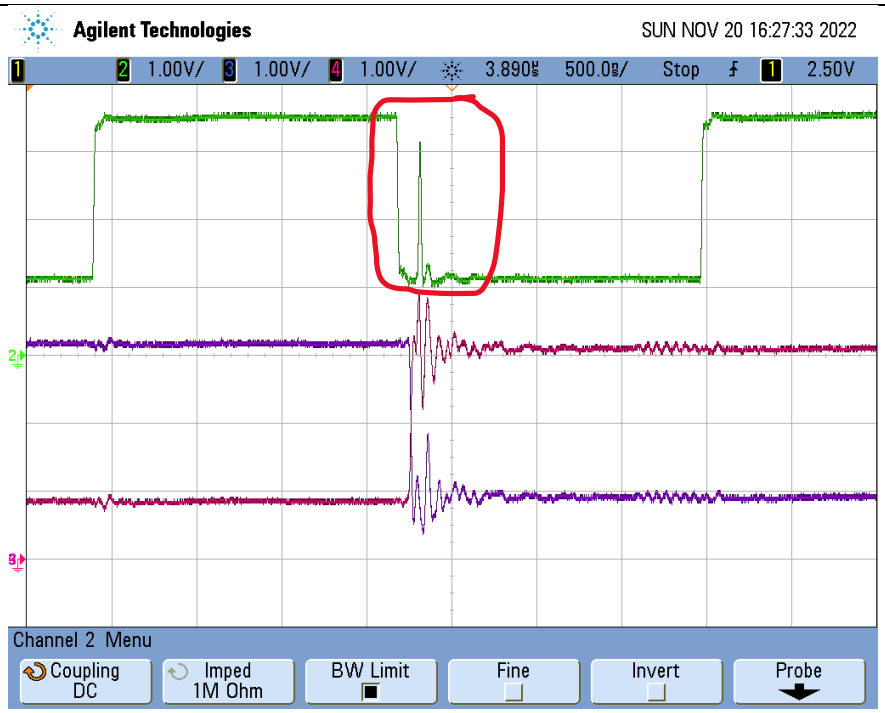

Zoomed MA- only (top) and SLO+, SLO- (bottom) on same oscilloscope capture. Note glitch.

9.5.3. Speedgoat Single-Ended MA Clock Signal Glitch

The "glitch" observed on the Speedgoat "BiSS Master CLK" is only present when it is connected to the Texas Instruments THVD1551DGKR [34].

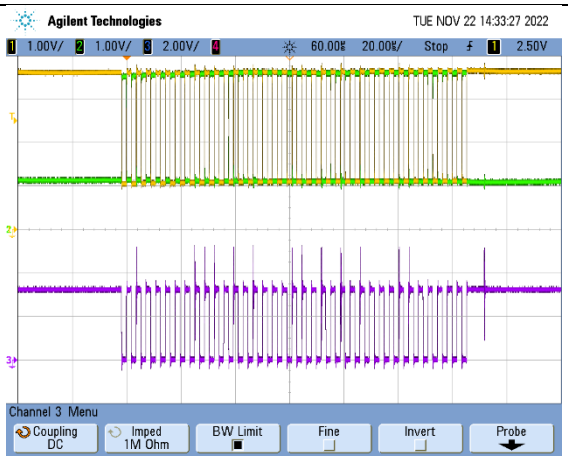

MA+, MA- (top) and Speedgoat "BiSS Master CLK" (bottom) on same oscilloscope capture. Note glitches.

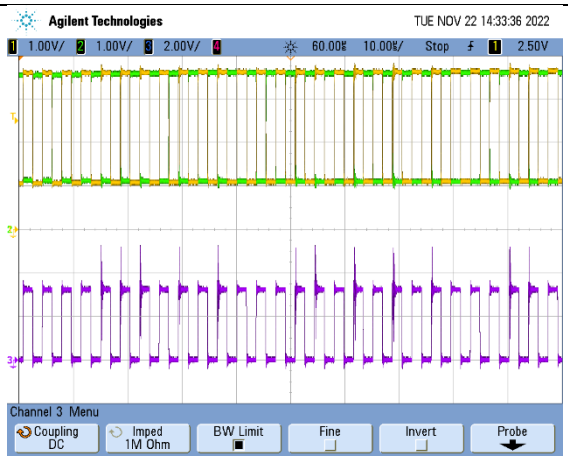

MA+, MA- (top) and Speedgoat "BiSS Master CLK" (bottom) on same oscilloscope capture. Note glitches.

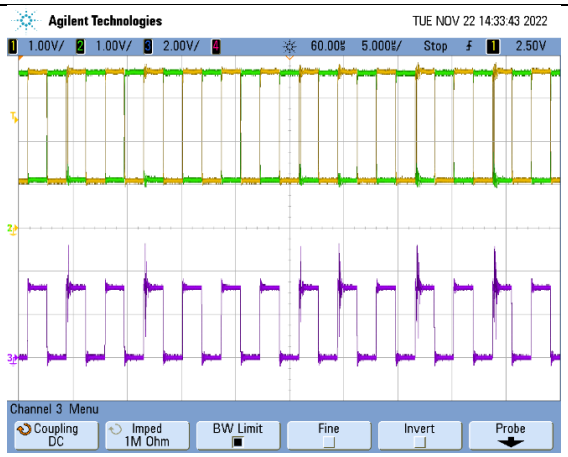

MA+, MA- (top) and Speedgoat "BiSS Master CLK" (bottom) on same oscilloscope capture. Note glitches.

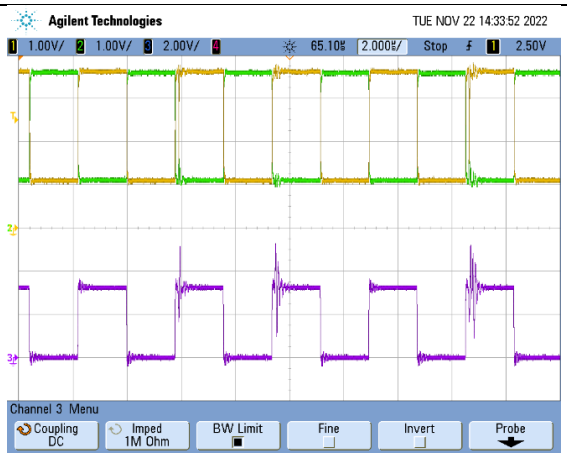

MA+, MA- (top) and Speedgoat "BiSS Master CLK" (bottom) on same oscilloscope capture. Note glitches.

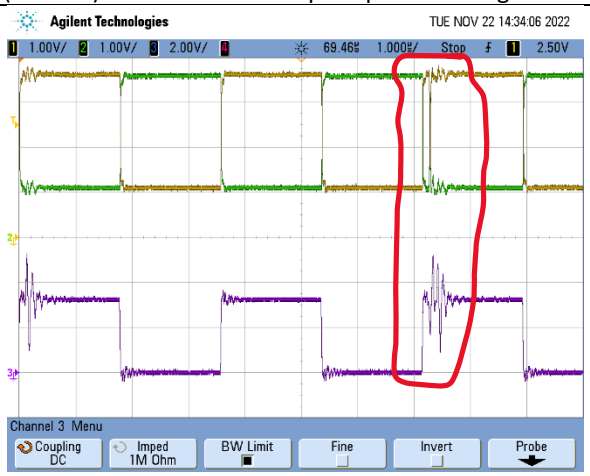

MA+, MA- (top) and Speedgoat "BiSS Master CLK" (bottom) on same oscilloscope capture. Note glitches.

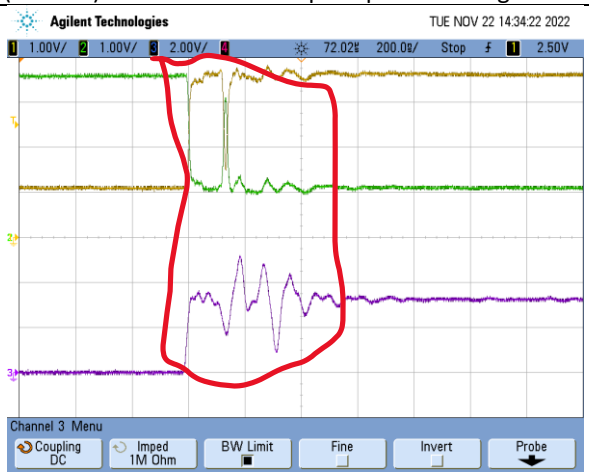

MA+, MA- (top) and Speedgoat "BiSS Master CLK" (bottom) on same oscilloscope capture. Note glitches.

Speedgoat "BiSS Master CLK" disconnected from the Texas Instruments THVD1551DGKR. Note *no* glitches. Note 3000*tic = 40 µs timeout, as expected. Looks good.

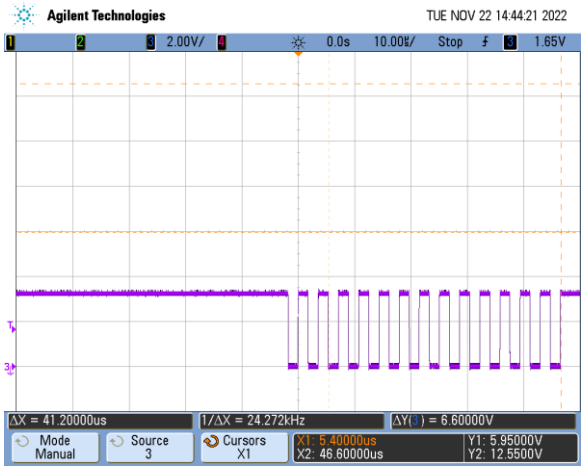

Speedgoat "BiSS Master CLK" disconnected from the Texas Instruments THVD1551DGKR. Note *no* glitches. Note 3000*tic = 40 µs timeout, as expected. Looks good.

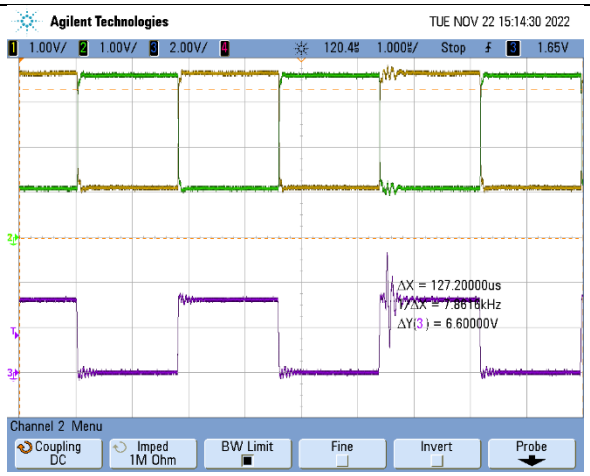

Added series termination resistor at Speedgoat “BiSS Master CLK”. Note poor signal integrity is still present, but good enough to prevent glitches at the Texas Instruments THVD1551DGKR MA+ and MA- outputs. Note *no* glitches in MA+ and MA-.

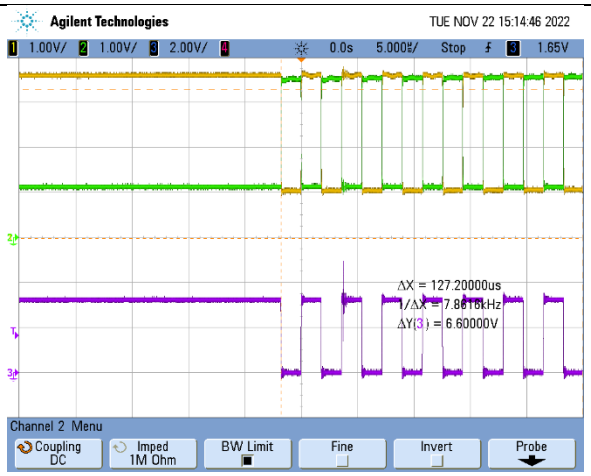

Added series termination resistor at Speedgoat “BiSS Master CLK”. Note poor signal integrity is still present, but good enough to prevent glitches at the Texas Instruments THVD1551DGKR MA+ and MA- outputs. Note *no* glitches in MA+ and MA-.

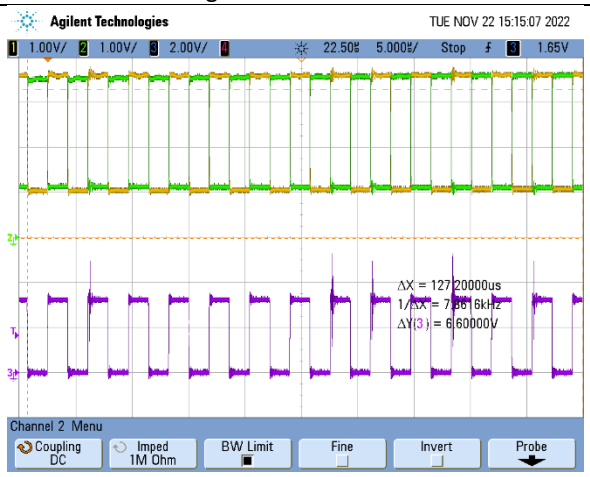

Added series termination resistor at Speedgoat “BiSS Master CLK”. Note poor signal integrity is still present, but good enough to prevent glitches at the Texas Instruments THVD1551DGKR MA+ and MA- outputs. Note *no* glitches in MA+ and MA-.

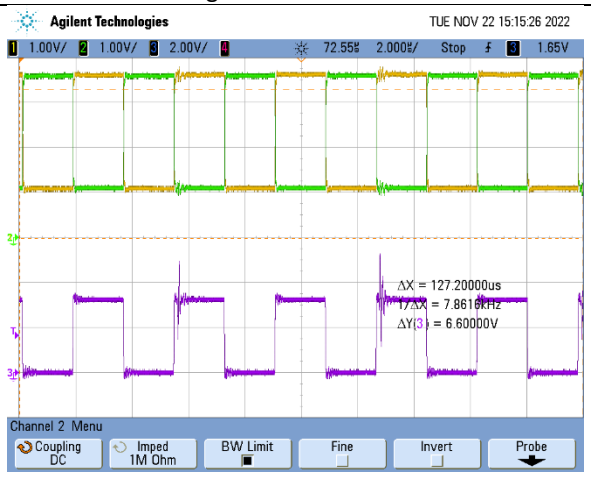

Added series termination resistor at Speedgoat “BiSS Master CLK”. Note poor signal integrity is still present, but good enough to prevent glitches at the Texas Instruments THVD1551DGKR MA+ and MA- outputs. Note *no* glitches in MA+ and MA-.

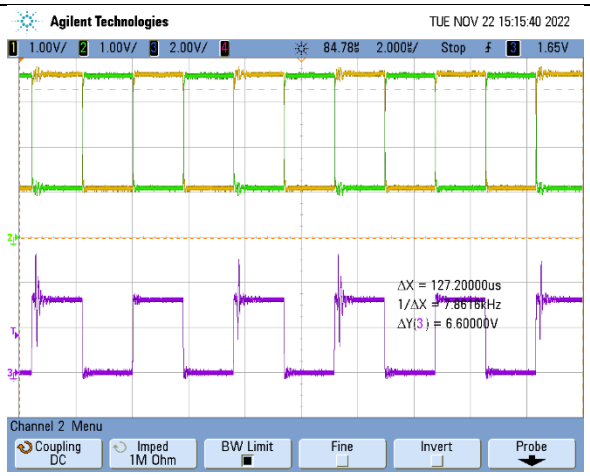

Added series termination resistor at Speedgoat "BiSS Master CLK". Note poor signal integrity is still present, but good enough to prevent glitches at the Texas Instruments THVD1551DGKR MA+ and MA- outputs. Note *no* glitches in MA+ and MA-.

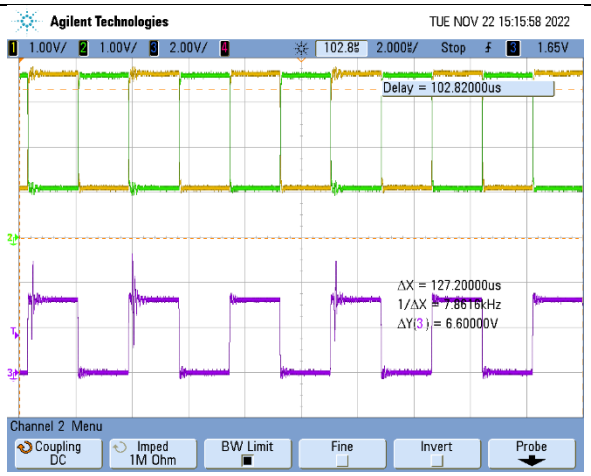

Added series termination resistor at Speedgoat "BiSS Master CLK". Note poor signal integrity is still present, but good enough to prevent glitches at the Texas Instruments THVD1551DGKR MA+ and MA- outputs. Note *no* glitches in MA+ and MA-.

After the series termination resistor was added at the Speedgoat "BiSS Master CLK," 18-bit position data were measured every 15 degrees using the Speedgoat and MATLAB Simulink. The measured 18-bit Rx position data looked perfect.

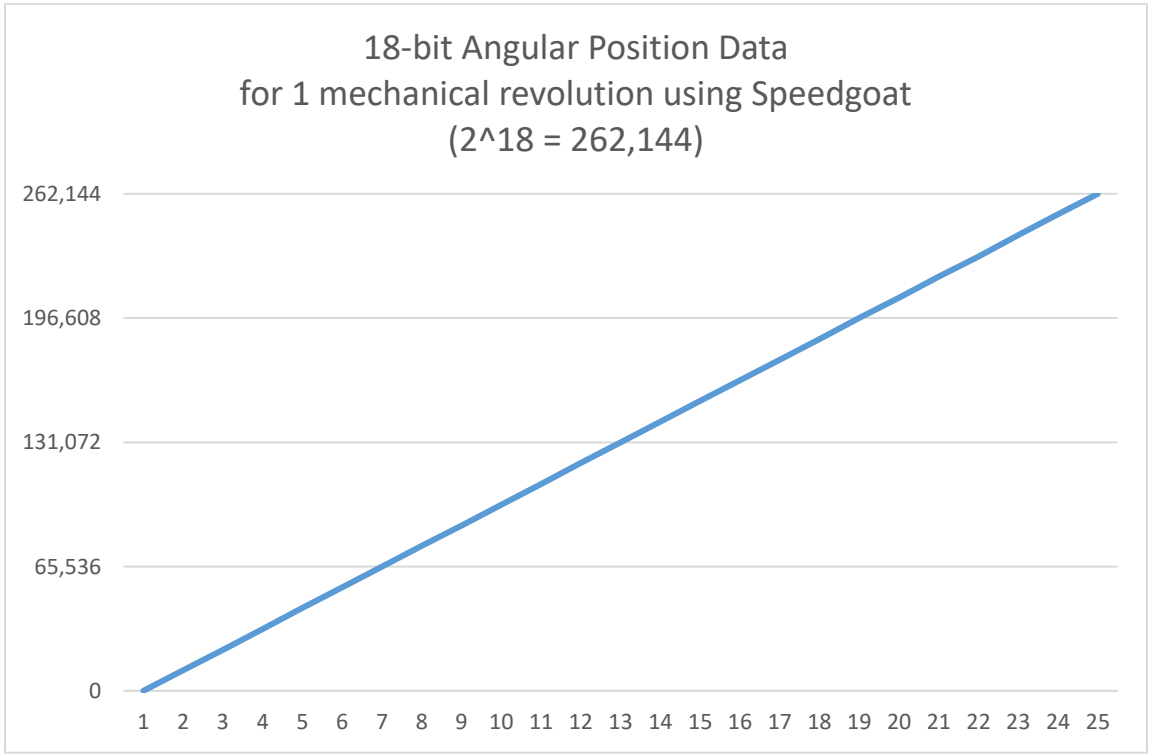

9.5.4. Rotary Encoder Interface Problem Root Cause

The root cause of the problem was poor signal integrity between the Speedgoat "BiSS Master CLK" output and the Texas Instruments THVD1551DGKR [34] digital input (Figure 9.7). Adding a series termination resistor and twisted-pair ("BiSS Master CLK" and GND) improved the poor signal integrity enough to eliminate the glitches on MA+ and MA-.

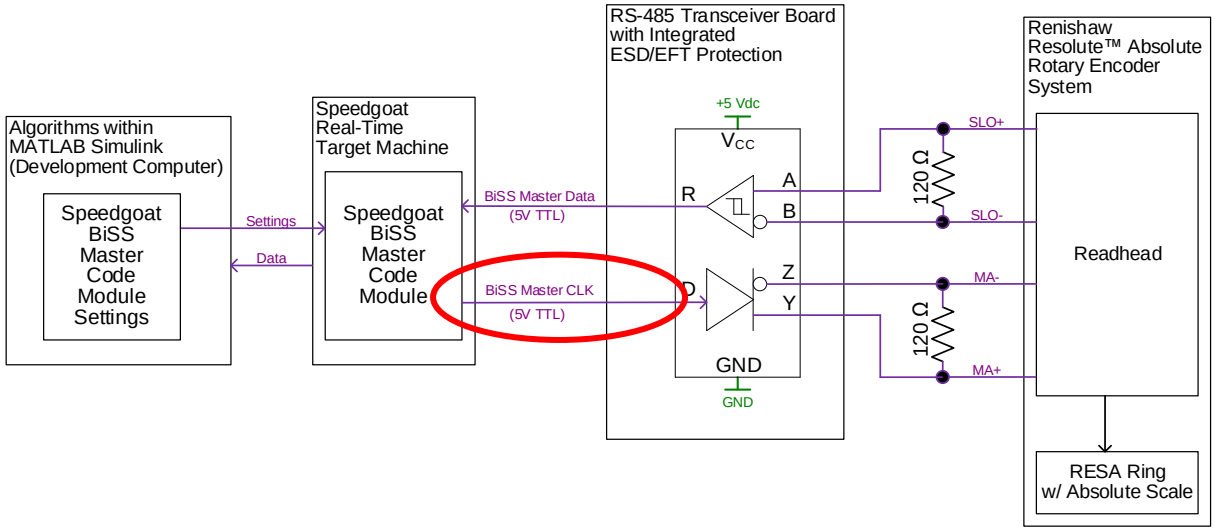

Figure 9.7 Rotary Encoder Interface Problem Root Cause

CHAPTER 10. MECHANICAL DEVELOPMENT

Having the machine's rotor supported magnetically by a Halbach magnet array (as shown in Figure 1.3) is a major component of this project's end goal. The first approach to achieving this was an all-up test in which the array of superconducting magnets was brought down to their operating temperature (approximately $-320°\text{F}$) and an attempt was made at "hovering" the rotor. However, this type of machine has 6 degrees of freedom, and properly controlling all of them at once (although one degree is passively controlled) requires more understanding of its inherent physical and electrical characteristics. Consequently, a staged approach (specifically pertaining to the rotor's support along its axis of rotation, the z-axis) was adopted, and this chapter outlines key aspects of the mechanical design that facilitate this staging approach.

10.1. Absolute Rotary Encoder Testing Equipment

As outlined in Chapter 9, the absolute rotary encoder is physically attached to, and rotates with, the rotor. The encoder provides real-time information about the angular position (from which speed can also be derived) of the machine's salient poles, which is critical information for controlling the energizing sequence of the stator coils. Ensuring that the real-time data acquisition system and the encoder's readhead properly "talk" to one another (see Chapter 9) was an important step for overall sensor integration. Separate testing hardware was manufactured to spin the rotary encoder at projected operating speeds and then to observe/test sensor and data acquisition compatibility.

Figure 10.1 shows the CAD model for a hub to which the rotary encoder is bolted. This hub is then bolted to a secondary hub (see [30]), which then couples this assembly (both hubs bolted together) to the motor shaft through a set screw. Figure 10.2 shows the drawing file for this part.

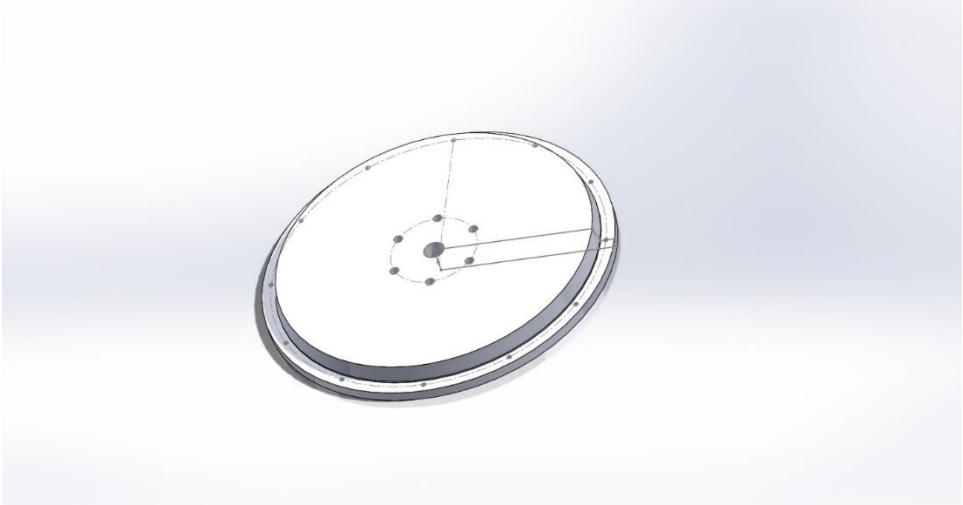

Figure 10.1 Rotary Encoder Test Fixture Primary Hub "Part"

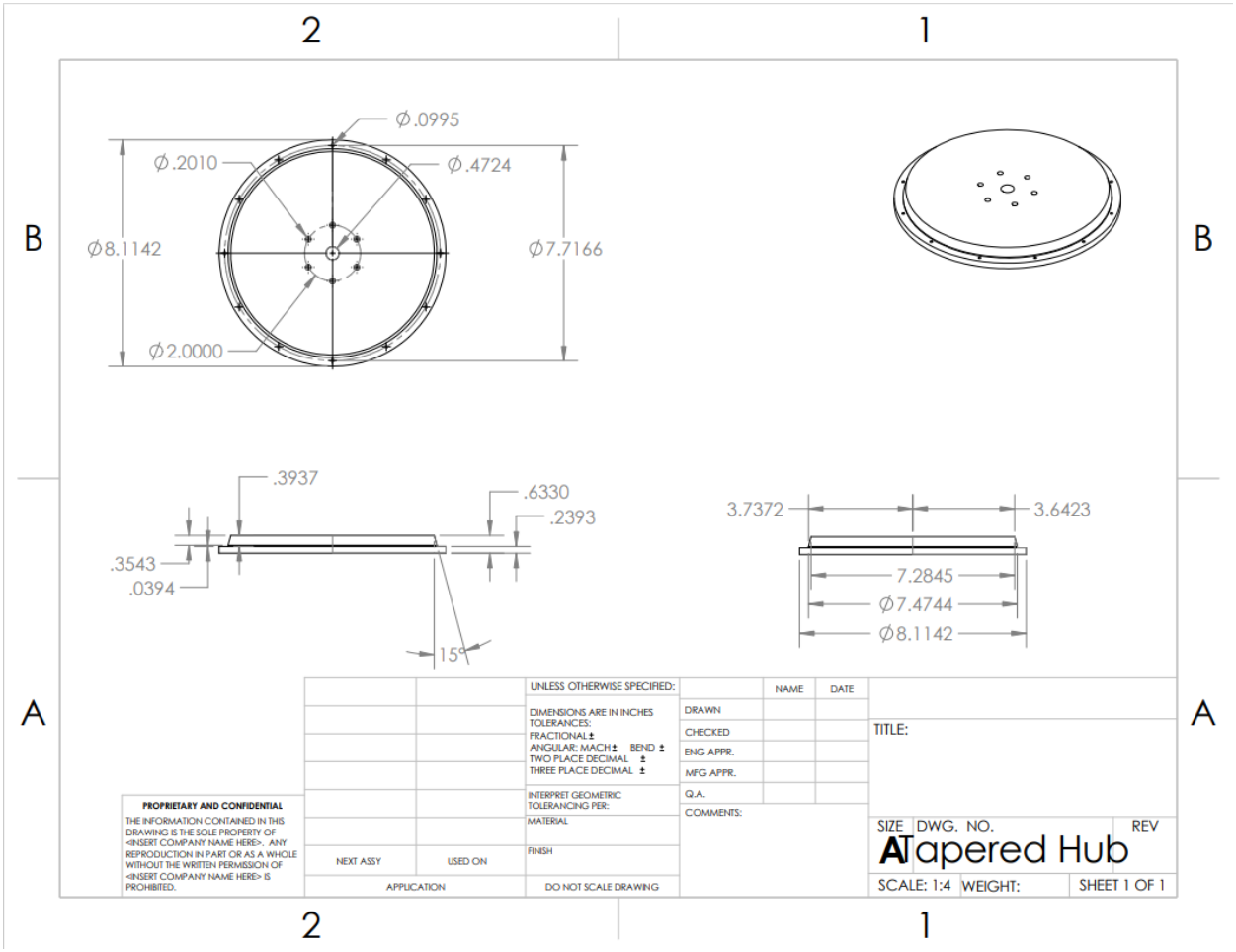

Figure 10.2 Rotary Encoder Test Fixture Primary Hub "Drawing File"

This part's dimensions and tolerancing were designed according to Renishaw's installation guidelines [33]. Additionally, the manufacturing process for these parts took considerable precautions to ensure that they were as concentric as possible. When the RESA ring was mounted to the hub, a dial indicator was also used to verify that the tapers of the hub and ring were evenly engaged. Otherwise, the ring could develop a more oval shape and interfere with the readhead's ride height of $0.8 \pm 0.15\ mm$.

Figure 10.3 shows the secondary hub with the set screw to couple both the primary and secondary hubs to the motor shaft. Both the primary and secondary hubs were machined and reamed as one unit to maintain concentricity.

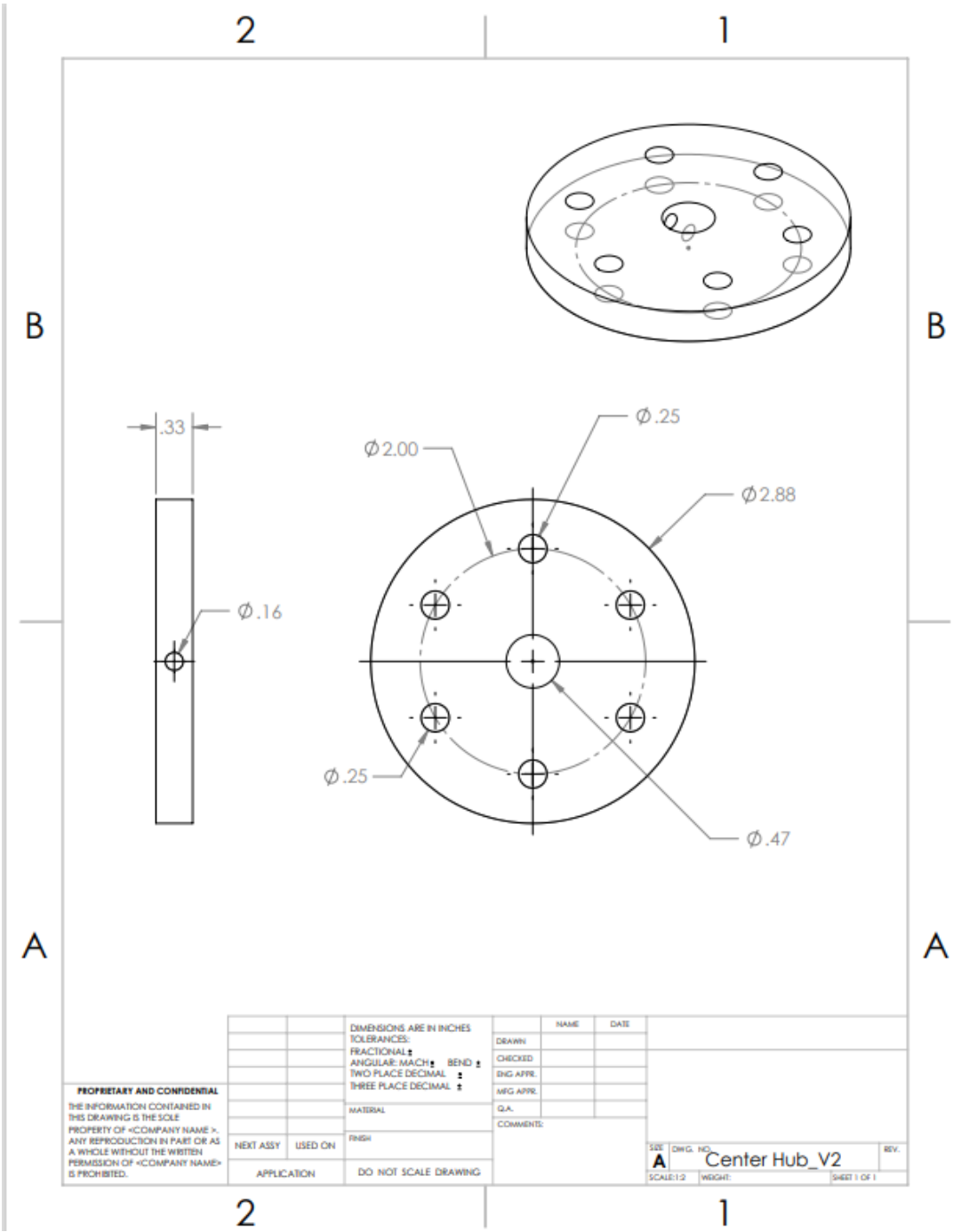

Figure 10.3 Rotary Encoder Test Fixture Secondary Hub "Drawing File"

Figure 10.4 shows the final assembly with the RESA ring attached to the primary hub. For reference, the ring testing assembly was mounted to a three-phase, 220V motor and driven by an external variable frequency drive (VFD). This test fixture is capable of speeds up to 3600

rpm (projected operating speeds of the fly wheel), even though the motor's rated speed is 1570 rpm. The motor load is fairly low, and the VFD is capable of almost 500 Hz of three-phase output.

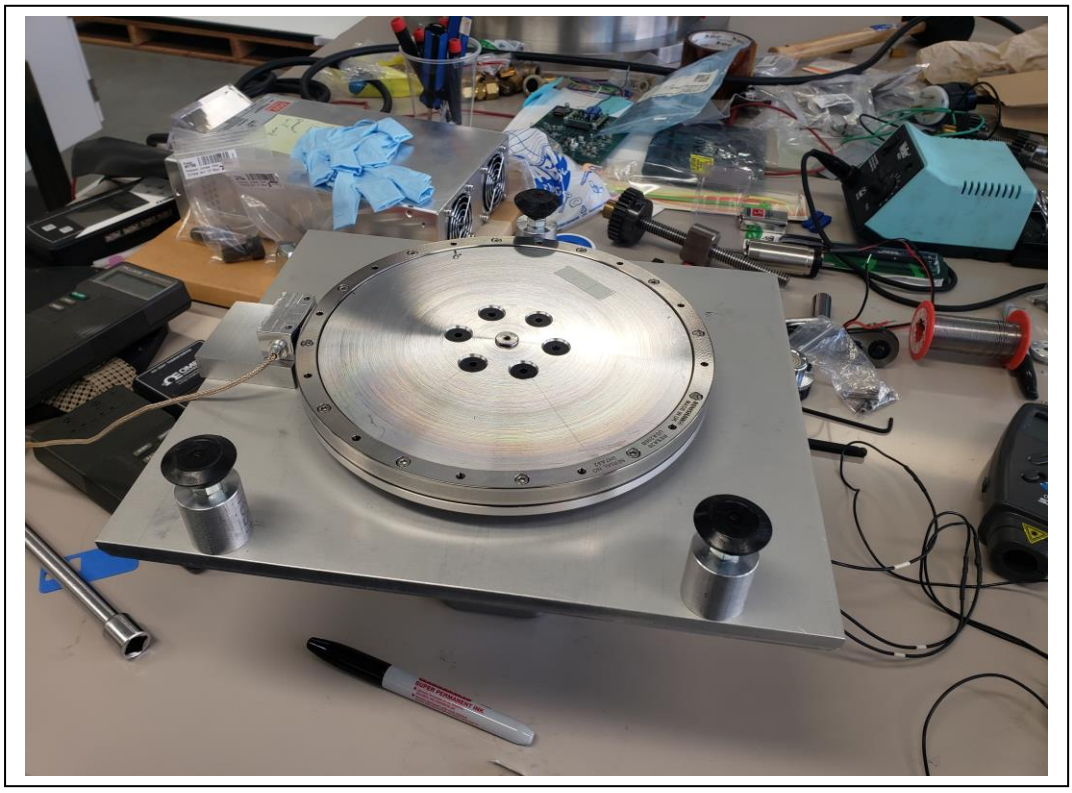

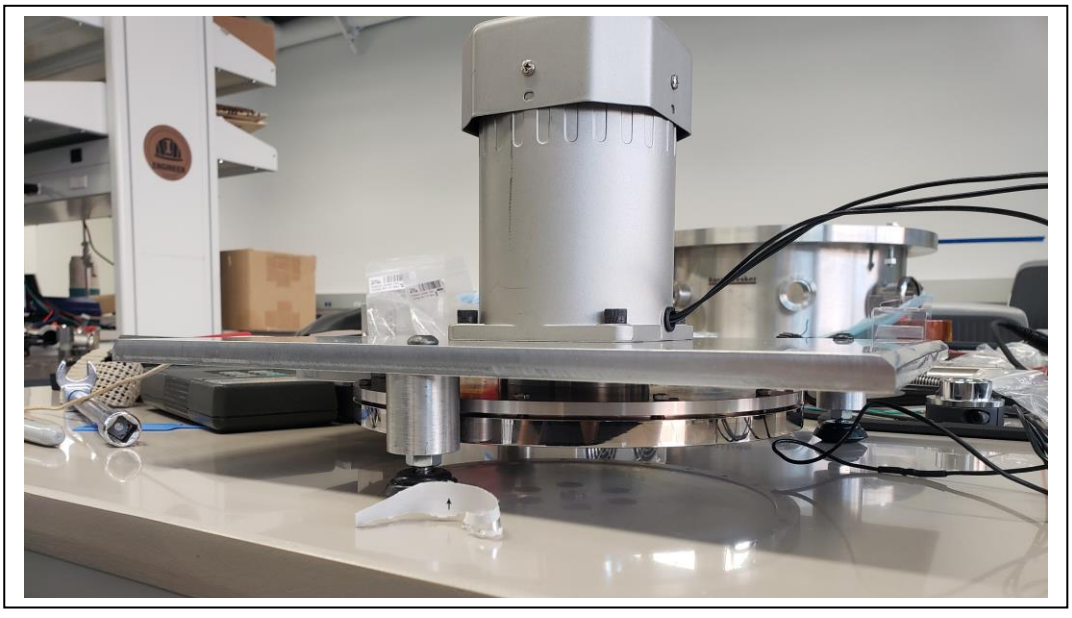

Figure 10.4 Final Assembly of Rotary Encoder Test Fixture

10.2. Air Bearing Fixture

As an intermediary step for eventually working up to using the Halbach magnet array of superconductors, an air bearing will provide the passive support along the rotor's axis of rotation (z-axis) for incremental development testing stages. Part of the motivation for using an air bearing is to partially reduce the degrees of freedom that need to be controlled. Consequently, this will allow for more focused tuning of the coil energizing sequence as well as the active magnet bearing (AMB). There is a channel through which the "cap" on the bottom of the rotor will ride that will also have physical guard rails, thereby assisting in the AMB's role to correct for the roll and pitch of the rotor assembly.

Figures 10.5 and 10.6 show the air bearing plenum through which building air will enter at approximately 80 psi. The plenum has a form factor similar to that of the superconductor array and will be, ideally, a drop-in substitute.

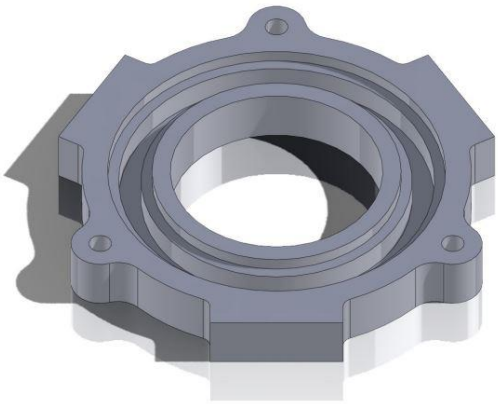

Figure 10.5 Air Bearing "Part"

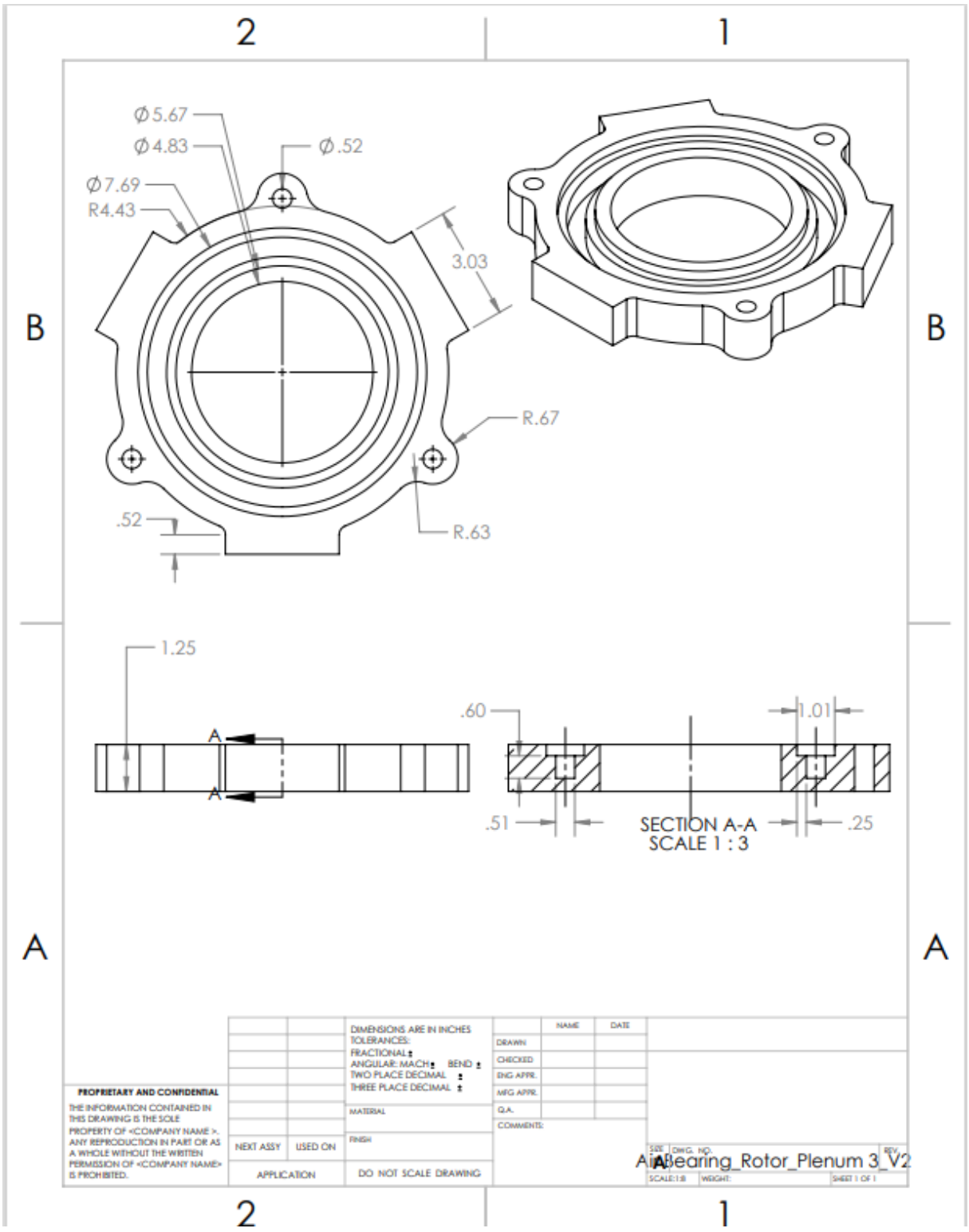

Figure 10.6 Air Bearing "Drawing File"

The plenum takes in air from six entry points (two inlets per lug) through the three square lugs (depicted in the figures above) and distributes the air throughout the main channel. Air is then forced up through the radially spiraled holes in the distribution plate, which are intended to increase the incoming air's stream velocity. The flywheel will "ride" on a film of air between the distribution plate and the flywheel tray.

Figures 10.7 and 10.8 show the part and its drawing file, respectively

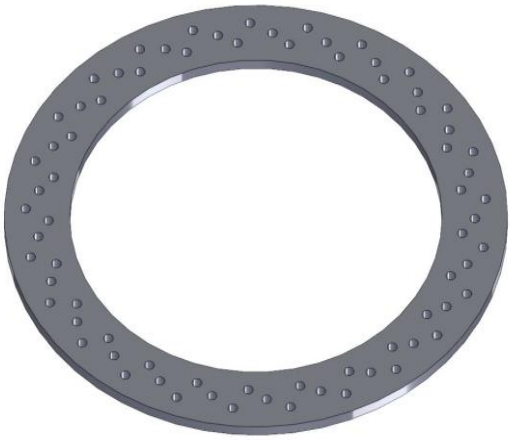

Figure 10.7 Air Distribution Plate "Part"

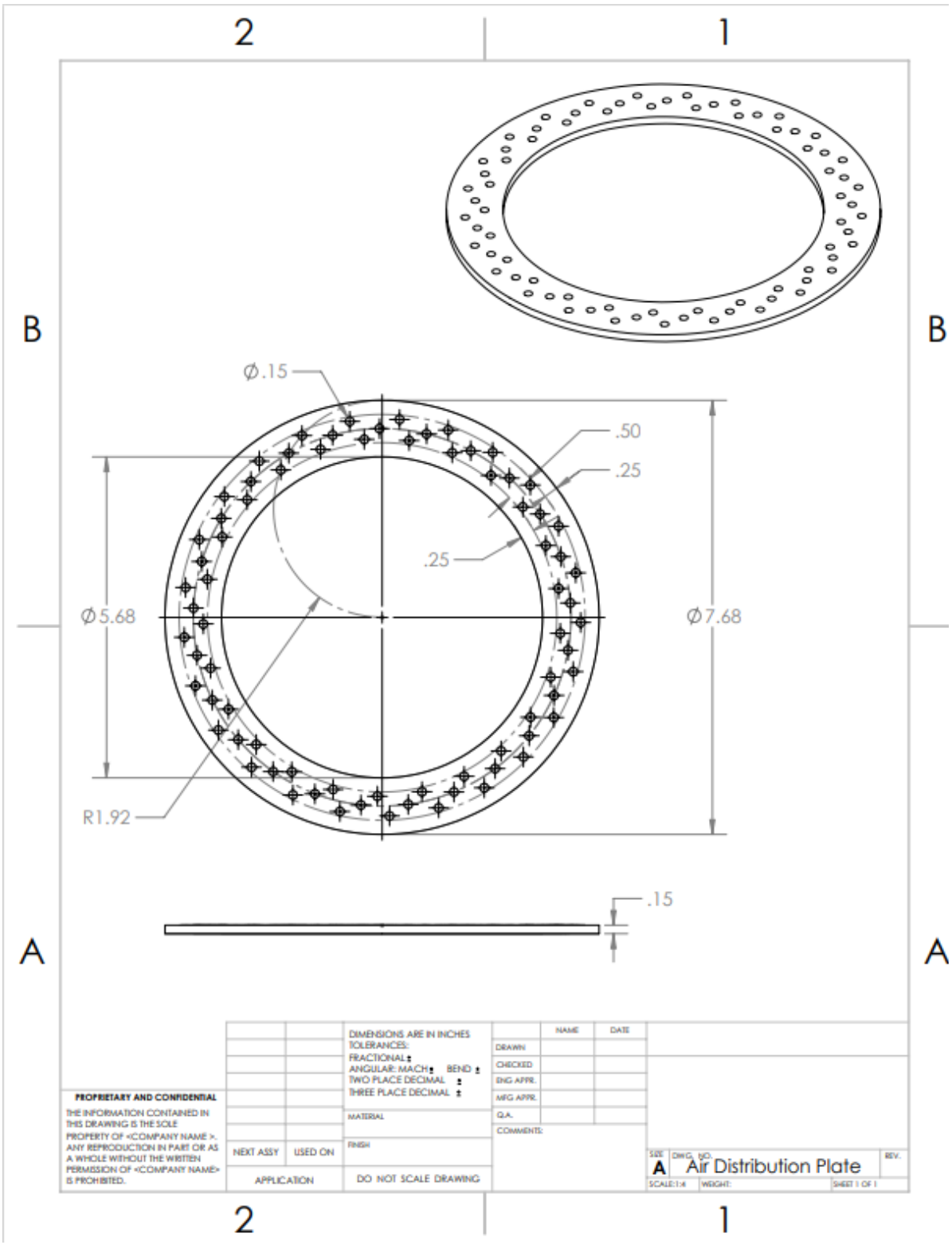

Figure 10.8 Air Distribution Plate "Drawing File"

The last component in this assembly is the “tray,” which attaches to the bottom of the rotor and has a protrusion that sits in the channel on top of the air distribution plate. Figures 10.9 and 10.10 show the part and its drawing file, respectively.

Figure 10.9 Rotor Tray “Part”

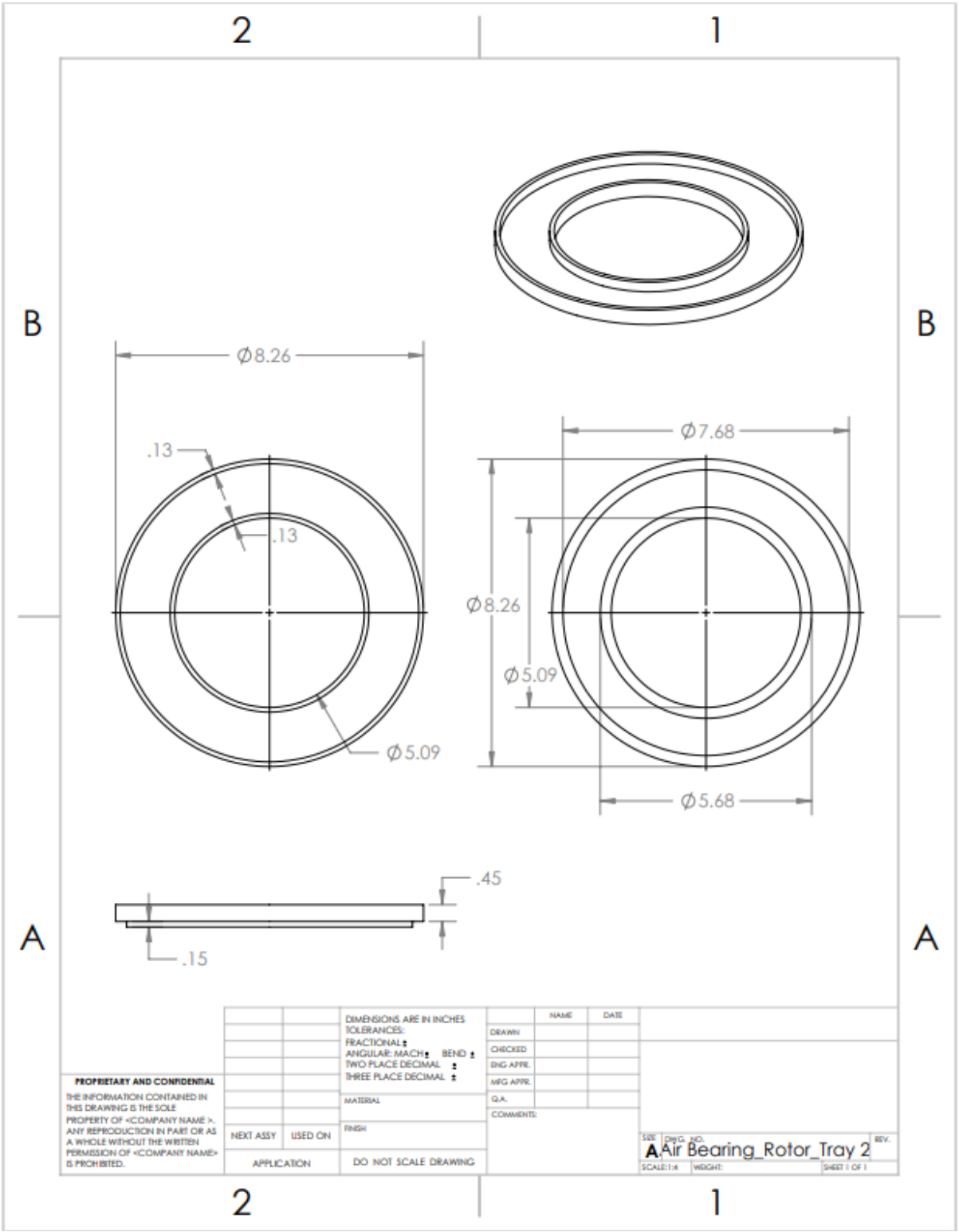

Figure 10.10 Rotor Tray "Drawing File"

Figure 10.11 shows the final assembly of the air bearing. Note that the rotor is not depicted here.

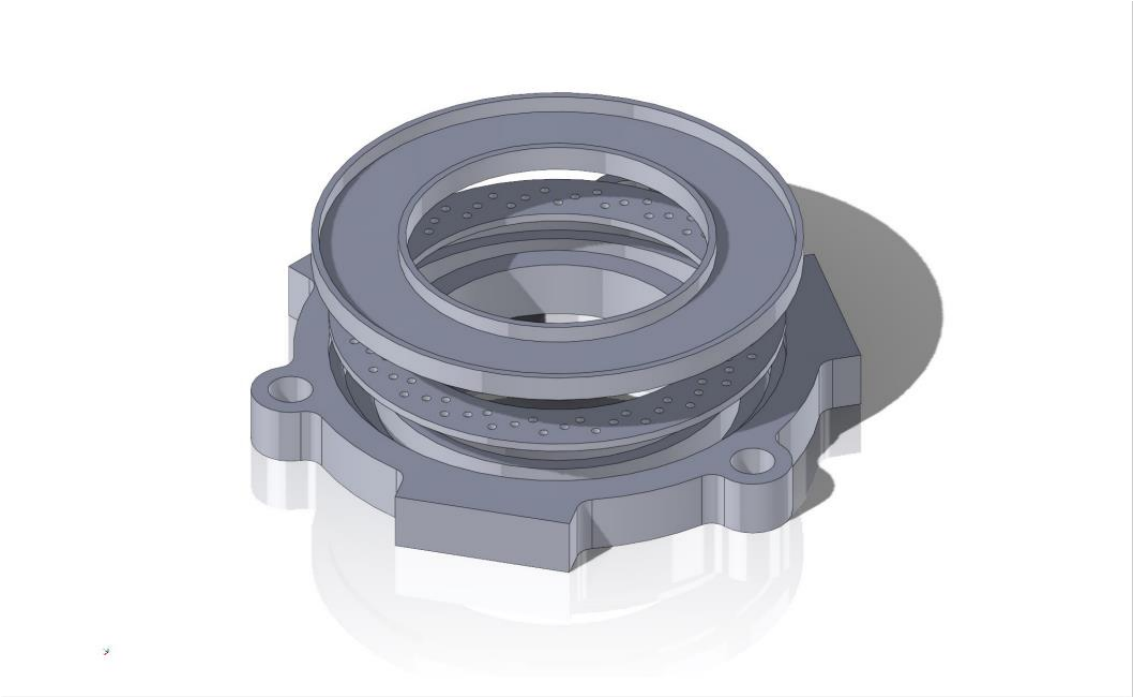

Figure 10.11 Air Bearing “Assembly”

10.3. Stator Rewinding

Previous testing to spin the rotor resulted in the possible burning of one (or more) stator energizing coils. Consequently, additional work was undertaken to have the motor professionally re-wound. As a result, the active magnetic bearing (AMB), which was press-fit onto the stator shaft, had to be disassembled. To access the underside of the AMB, the top of the coils were cut off to provide more space for the pulling collar. The pulling collar was manufactured and then cut in half to fit around the shaft. A bearing puller was then placed underneath, and the stator was placed on a hydraulic press. Figure 10.12 shows a few of the stator rewinding steps for a better view.

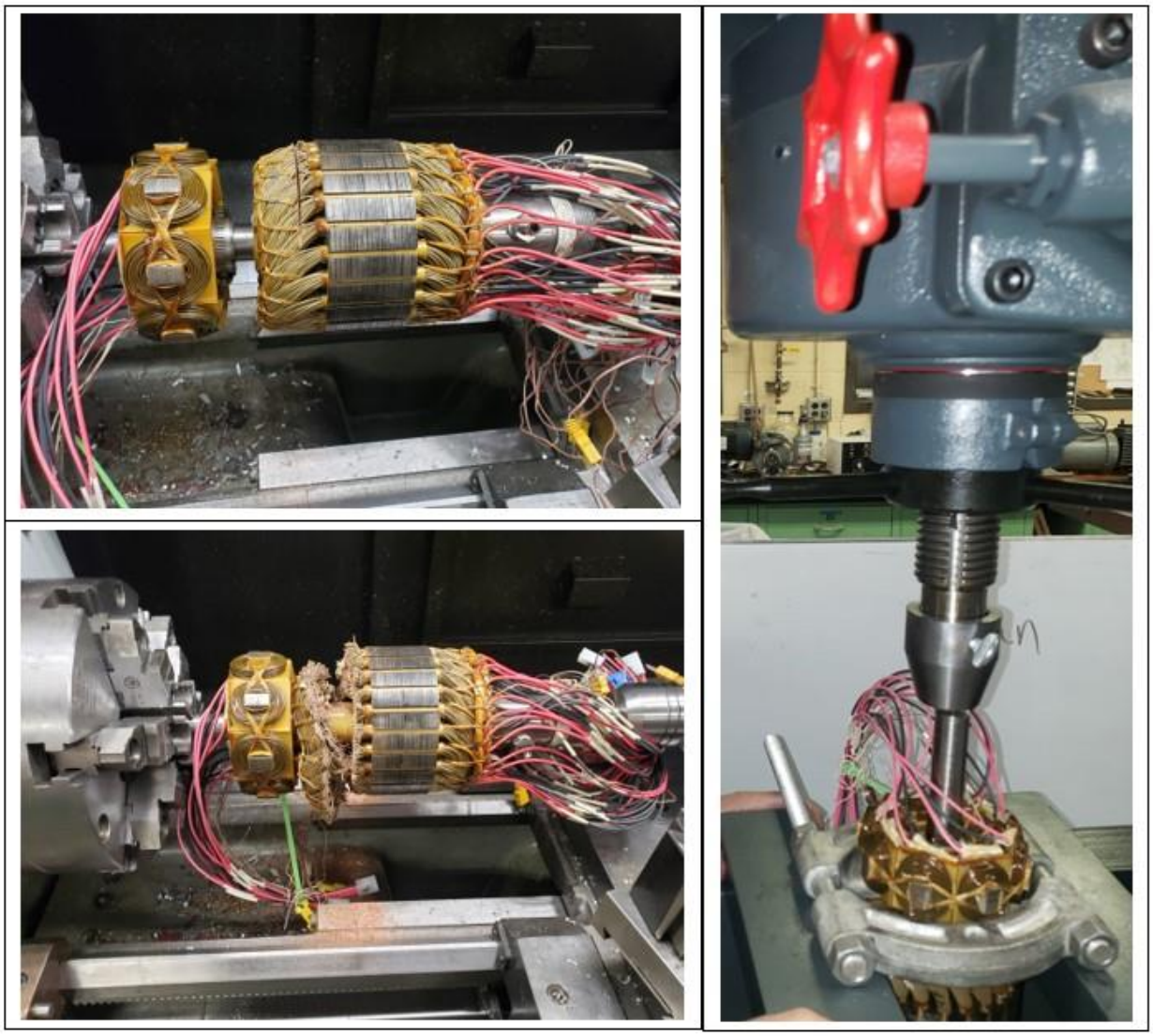

Figure 10.12 Coil Top Removal for Pulling Collar Clearance

CHAPTER 11. CONCLUSIONS

The research presented herein established the feasibility of using AMB control software and hardware for the University of Idaho's (UI) flywheel energy storage system (FESS). A single-axis AMB academic test fixture was used to test the sensor and actuator subsystems.

The H-bridge pulse width modulation (PWM) current actuator operation was developed, as described in Chapter 4.

The Hall-effect current sensor mathematical model was defined, as described in Chapter 5, from the manufacturer's data for the actual hardware. The sensor-measured output voltage data were obtained and observed to be noisy. Increasing the current sensor's filter capacitor, and thereby reducing the current sensor's bandwidth, significantly reduced the observed noise of the signal representing the sensed current.

The non-contact Eddy current displacement sensor mathematical model was defined from the manufacturer's specification and sensor calibration data, as described in Chapter 6. The physical hardware testing was notably consistent with the mathematical model and no significant sensor signal noise was observed.

For all three sensors and actuator subsystems, the physical interface is documented for integration into the flywheel energy storage system.

The equations of motion and a dynamic plant model of the single-axis AMB academic test fixture were developed, as described in Chapter 7. The plant model developed was the foundation for control system development. Simulink Real-Time hardware-in-the-loop testing with the physical sensors and actuators was conducted, as described in Chapter 8.

The current sensors' ratiometric output sensitivity to the current sensors' 5V supply voltage warrants careful selection of a 5V power source. This is an example of a small but important hardware implementation detail that was observed only during physical hardware testing.

The current sensors' digital signal was observed to be noisy, as shown in Figure 8.2. Reducing the analog bandwidth of the current sensor, i.e., reducing the cut-off frequency of the analog low-pass-filter of the current sensor analog output signal, reduced the observed measurement noise, as shown in Figure 8.3.

Chapter 9 presents the results of this project's development of the rotary encoder system interface. The rotary absolute encoder interface was designed, built, and tested in hardware. The

rotary encoder interface did not work initially. Troubleshooting steps were taken and the root cause was found (see section 9.5.4). After the root cause had been addressed, the Renishaw Resolute™ rotary absolute encoder system block diagram was functional in hardware.

Having the UI FESS rotor assembly supported magnetically by a Halbach magnet array (as shown in Figure 1.3) is a major component of this project's end goal. An air bearing fixture to support the rotor assembly in the z-axis (axis of rotation) was developed as an intermediate development step. The mechanical design of this air bearing fixture is detailed in Chapter 10.

REFERENCES

[1] W.-J. Guan, X.-Y. Zheng, K. F. Chung, and N.-S. Zhong, "Impact of air pollution on the burden of chronic respiratory diseases in China: Time for urgent action," *Lancet*, vol. 388, no. 10054, pp. 1939–1951, Oct. 2016.

[2] Md Ahsanual Hoque Rafi, and Jennifer Bauman, "A Comprehensive Review of DC Fast-Charging Stations With Energy Storage: Architectures, Power Converters, and Analysis," IEEE Transactions on Transportation Electrification, Vol. 7, No. 2, June 2021.

[3] Majid Moradzadeh, and Morad Mohamed Abdelmageed Abdelaziz, "A Stochastic Optimal Planning Model for Fully Green Stand-Alone PEV Charging Stations," IEEE Transactions on Transportation Electrification, Vol. 7, No. 4, December 2021.

[4] Zeinab Moghaddam, Iftekhar Ahmad, Daryoush Habibi, and Quoc Viet Phung, "Smart Charging Strategy for Electric Vehicle Charging Stations," IEEE Transactions on Transportation Electrification, Vol. 4, No. 1, March 2018.

[5] Emin Ucer, Işıl Koyuncu, Mithat C. Kisacikoglu, Mesut Yavuz, Andrew Meintz, and Clément Rames, "Modeling and Analysis of a Fast Charging Station and Evaluation of Service Quality for Electric Vehicles," IEEE Transactions on Transportation Electrification, Vol. 5, No. 1, March 2019.

[6] Juliette Ugirumurera, and Zygmunt J. Haas, "Optimal Capacity Sizing for Completely Green Charging Systems for Electric Vehicles," IEEE Transactions on Transportation Electrification, Vol. 3, No. 3, September 2017.

[7] Soodeh Negarestani, Mahmud Fotuhi-Firuzabad, Mohammad Rastegar, and Abbas Rajabi-Ghahnavieh, "Optimal Sizing of Storage System in a Fast Charging Station for Plug-in Hybrid Electric Vehicles," IEEE Transactions on Transportation Electrification, Vol. 2, No. 4, December 2016.

[8] Ziaoying Gan, Haoxiang Zhang, Gai Hang, Zhida Qin, and Haiming Jin, "Fast-Charging Station Deployment Considering Elastic Demand," IEEE Transactions on Transportation Electrification, Vol. 6, No. 1, March 2020.

[9] Xiaoyu Duan, Zechun Hu, Yonghua Song, Kai Strunz, Yan Cui, and Likai Liu, "Planning Strategy for an Electric Vehicle Fast Charging Service Provider in a Competitive Environment," this article has been accepted for publication in a future issue of IEEE Transactions on Transportation Electrification, Citation Information: DOI 10.1109/TTE.2022.3152387.

[10] Muhammad Hosnee Mobarak, Rafael N. Kleiman, and Jennifer Bauman, "Solar-Charged Electric Vehicles: A Comprehensive Analysis of Grid, Driver, and Environmental Benefits," IEEE Transactions on Transportation Electrification, Vol. 7, No. 2, June 2021.

[11] Hao Tu, Hao Feng, Srdjan Srdic, and Srdjan Lukic, “Extreme Fast Charging of Electric Vehicles: A Technology Overview,” IEEE Transactions on Transportation Electrification, Vol. 5, No. 4, December 2019.

[12] B. Kisling. “Active Magnetic Bearing Control for an Experimental Flywheel Energy Storage System”. Master’s Thesis. University of Idaho, 2014.

[13] K. Ramus. “Power Electronic Components and Hardware for an Experimental Flywheel Energy Storage System”. Master’s Thesis. University of Idaho, 2014.

[14] Wikipedia, 2022. *Pacific Northwest*. https://en.wikipedia.org/wiki/Pacific_Northwest. Accessed May 14, 2022.

[15] SAE International, Standard J1772_201710, “SAE Electric Vehicle and Plug in Hybrid Electric Vehicle Conductive Charge Coupler,” https://doi.org/10.4271/J1772_201710 . Accessed May 14, 2022.

[16] Peiwen He, and Alireza Khaligh, “Comprehensive Analyses and Comparison of 1 kW Isolated DC-DC Converters for Bidirectional EV Charging Systems,” IEEE Transactions on Transportation Electrification, Vol. 3, No. 1, March 2017.

[17] Tonghqo Pei, Dawei Li, Jiayun Liu, Jian Li, and Wugin Kong, “Review of Bearingless Synchronous Motors: Principle and Topology,” this article has been accepted for publication in a future issue of IEEE Transactions on Transportation Electrification, Citation Information: DOI 10.1109/TTE.2022.3164420.

[18] Xiaojun Li, Alan Palazzolo, and Zhiyang Wang, “A Combination 5-DOF Active Magnetic Bearing for Energy Storage Flywheels,” IEEE Transactions on Transportation Electrification, Vol. 7, No. 4, December 2021.

[19] A. Buchroithner, H. Wegleiter, and B. Schweighofer, “Flywheel energy storage systems compared to competing technologies for grid load mitigation in EV fast-charging applications,” in Proceedings IEEE 27th International Symposium Industrial Electronics (ISIE), June 2018, pp. 508-514, doi: 10.1109/ISIE.2018.8433740.

[20] Pololu High-Power Motor Driver 36v20 CS. https://www.pololu.com/product/1457. Accessed May 14, 2022.

[21] Infineon IPD048N06L3 G OptiMOS 3 Power-Transistor Datasheet. https://www.infineon.com/dgdl/Infineon-IPD048N06L3-DS-v02_00-en.pdf?fileId=db3a30431ddc9372011e2b4f496e4db0. Accessed May 14, 2022.

[22] Allegro Microsystems A3941KLPTR-T Datasheet, Automotive Full Bridge MOSFET Driver. https://www.allegromicro.com/-/media/files/datasheets/acs714-datasheet.ashx. Accessed May 14, 2022.

[23] Jing Huang, Krishnan Padmanabhan, and Oliver M. Collins, "The Sampling Theorem With Constant Amplitude Variable Width Pulses," IEEE Transactions on Circuits and Systems, Vol. 58, No. 6, June 2011.

[24] Allegro Microsystems ACS714 Datasheet, Automotive Grade, Fully Integrated, Hall-Effect-Based Linear Current Sensor IC with 2.1 kVRMS voltage Isolation and Low-Resistance Current Conductor. https://www.allegromicro.com/-/media/files/datasheets/acs714-datasheet.pdf. Accessed May 14, 2022.

[25] Kaman KD-2306 Multi-Purpose Non-Contact Position/Displacement Sensing Instrument Data Sheet. https://www.kamansensors.com/wp-content/uploads/2016/10/Kaman_KD-2306_data_sheet_web.pdf. Accessed May 14, 2022.

[26] Kaman KD-2306 Non-Contact Displacement Measuring System User's Manual. https://www.kamansensors.com/wp-content/uploads/2017/03/Kaman_KD-2306_User_Manual.pdf. Accessed May 14, 2022.

[27] Kaman 9U Sensor. https://www.kamansensors.com/wp-content/uploads/2016/10/Kaman-9U-sensor.jpg. Accessed May 14, 2022.

[28] Renishaw Resolute™ UHV Absolute Optical Encoder Data Sheet L-9517-9530-02-B. https://www.renishaw.com/media/pdf/en/d9196500488b447a9a4dac9f39b2ba1a.pdf.

[29] Renishaw Resolute™ Absolute Optical Encoder with BiSS® Serial Communications Data Sheet L-9517-9448-05-B. https://resources.renishaw.com/en/details/--65803.

[30] Renishaw Resolute™ Absolute Encoder System with RESA30 Rotary (Angle) Ring Data Sheet L-9517-9399-03-B. https://www.renishaw.com/media/pdf/en/76ad426600e7463dbee0c4c48d7ca59f.pdf.

[31] Renishaw BiSS® C-mode (unidirectional) for Resolute™ Encoders Data Sheet Data Sheet L-9709-9005-03-F. https://www.renishaw.com/media/pdf/en/de4d6a54313b48c3a4dadef7207ac4c1.pdf.

[32] Renishaw White Paper: Safety First – the Position Determination and Checking Algorithms of the Resolute™ True-Absolute Optical Encoder. https://www.renishaw.com/media/pdf/en/85e8fcb53e06465a9b323634320a6830.pdf.

[33] Renishaw Installation Guide Resolute™ RESA30 and REXA30 Absolute Angle Encoders Data Sheet M-9553-9735-03-C. https://www.renishaw.com/media/pdf/en/6ed3d75885ef49b1aded7f99252ac069.pdf.

[34] Texas Instruments THVD1551DGKR Datasheet. https://www.ti.com/lit/ds/symlink/thvd1551.pdf.

[35] E201-9S USB Interface for Absolute BiSS-C Encoders. https://www.rls.si/eng/e201-usb-encoder-interface-123.

APPENDIX A: ALLEGRO ACS714 CURRENT SENSOR THEORY OF OPERATION

Sensing machine coil current is required for motor-generator control. This appendix discusses the Allegro ACS714 device which provides an economical and precise way of sensing ac and dc currents based on the Hall-effect. This discussion provides an overview of the ACS714 sensor and its characteristics.

ACS714 Evaluation Board

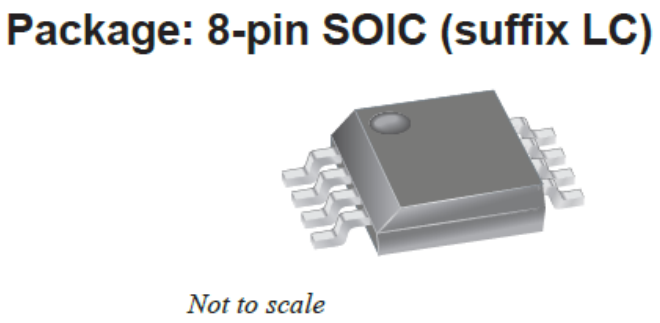

A.1. Hall-Effect

The Allegro ACS714 current sensor is based on the principle of the Hall-effect, which was discovered by Dr. Edwin Hall in 1879. According to this principle, when a current carrying conductor is placed into a magnetic field, a voltage is generated across its edges perpendicular to the directions of both the current and the magnetic field.

The fundamental physical principle behind the Hall-effect is the Lorentz force. When an electron moves along a direction, v, perpendicular to the appliced magnetic field, B, it experiences a force, F, the Lorentz force, which is normal to both the applied magnetic field and the electrical current flow.

$$Lorentz\ Force \quad \vec{F} = q\,\vec{v} \times \vec{B}$$

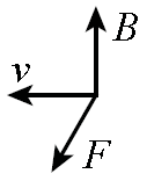

In response to the Lorentz force, F, the electroncs move in a curved path along the conductor and a net charge, and therefore a voltage, develops across the plate (orthogonal to the direction of current flow). This Hall voltage, V_H, obeys the formula below, which shows that V_H is proportional to the applied field strength, and that the polarity of V_H is determined by the direction, either north or south, of the applied magnetic field. **By this property, the Hall-effect is employed as a magnetic field sensor.**

$$V_H = \frac{I\,B_\perp}{\rho_n\,q\,t}$$

where:

V_H is the Hall voltage across the Hall element

I_H is the current passing through the Hall element

q is the magnitude of the charge of the charge carriers ($q = 1.602 \times 10^{-19}$ coulombs)

ρ_n is the charge carrier density (n signifies that the charge carriers are electrons)

t is the thickness of the Hall element plate

A thin plate of semiconductor material (called a Hall element) carries the current (I_H) and is placed into the magnetic field ($B_\perp$) which is perpendicular to the direction of current flow. Because of the presence of the Lorentz force, the distribution of current (I_H) is no longer uniform across the Hall element and therefore a potential difference is created across its edges perpendicular to the directions of both the current (I_H) and the magnetic field ($B_\perp$). This voltage, V_H, is known as the Hall voltage and its typical value is in the order of few microvolts. The Hall voltage is directly proportional to the magnitudes of I_H and $B_\perp$. So, if one of them (I_H) is known, then the observed Hall voltage can be used to estimate the other ($B_\perp$).

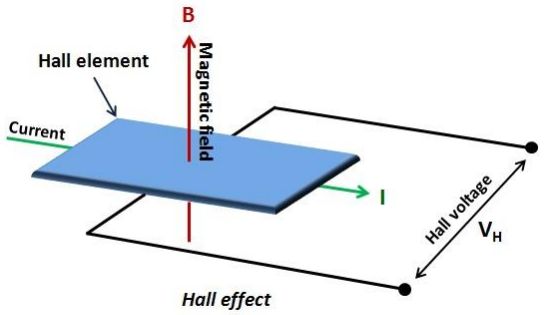

Figure A.1 Principle of the Hall-effect

The Allegro Microsystems ACS714LLCTR-30A-T [24] device is packaged in an 8-pin surface mount small outline integrated circuit (SOIC). Note that the primary current, I_P, flows through the primary copper conduction path (from pins 1 and 2, to pins 3 and 4) and does not flow through the Hall element. The primary current, I_P, induces a magnetic field, $B_\perp$, which is sensed by the Hall element. The Hall element is employed as a magnetic field sensor. The magnitude of the magnetic field, $B_\perp$, is linearly proportional to the magnitude of the primary current, I_P, providing a linear relationship between the output Hall voltage, V_H, and input primary current, I_P.

A.2. Hall Element Structure

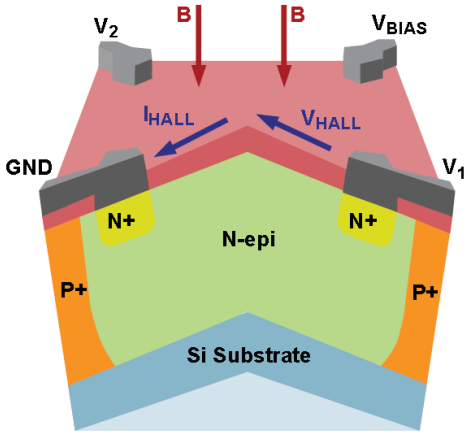

Allegro Hall-effect-based current sensor ICs are manufactured on silicon wafers. The Hall elements are part of the monolithic integrated circuits. Each Hall element is an area of doped silicon that creates an n-type plate that will conduct current, I_H. When a current, I_H, is forced from one corner of the plate to the opposite corner, a Hall voltage, V_H, develops across the other two corners of the plate when in the presence of a perpendicular magnetic field, $B_\perp$. The Hall voltage is zero when no magnetic field is applied.